UNIVERSITÀ DEGLI STUDI DELL'AQUILA
DIPARTIMENTO DI INGEGNERIA E SCIENZE DELL'INFORMAZIONE E MATEMATICA

Dottorato di Ricerca in Matematica e Modelli

XXXV ciclo

Titolo della tesi

Exploiting symmetries to improve variational quantum algorithms

SSD CHIM/02

Coordinatore del corso
Prof. Gabrielli Davide

Dottorando
Ratini Leonardo

Tutor
Prof. Guidoni Leonardo

A.A. 2021/2022

Contents

Summary 5

I Introduction **6**

1 Quantum computation and quantum information **7**
1.1 Qubits 7
1.2 Quantum computation 9
1.3 Quantum information 11

2 Simulating quantum systems **15**
2.1 The electronic structure problem 15
2.2 Classical simulations 19
2.3 Quantum simulations 22
2.3.1 Encoding methods 23
2.3.2 Variational quantum eigensolver 24
2.3.3 Final considerations 26

II Results **28**

3 Wavefunction Adapted Hamiltonian Through Orbital Rotations (WAHTOR) **29**
3.1 Introduction 30
3.2 The WAHTOR algorithm 31
3.3 Computational details 33
3.4 Results 37
3.4.1 State Vector Simulations 37
3.4.2 Noiseless measurement-based simulations 43
3.4.3 Noisy measurement-based simulations 45
3.5 Conclusions 47

4 Optimization strategies in WAHTOR algorithm 48
4.1 Introduction 48
4.2 Computational details 50
4.3 Results 54
4.3.1 Non-adiabatic WAHTOR algorithm 54
4.3.2 Quantum chemistry and Hubbard model results 57
4.4 Conclusions 60

5 Natural orbitals and compactness of quantum mutual information 62
5.1 Introduction 62
5.2 Computational details 64
5.3 Results 67
5.4 Conclusions 71

6 SU(N) fermions 73
6.1 Introduction 73
6.2 The method 73
6.3 Computational details 77
6.3.1 Simulated systems 77
6.3.2 Ansatz construction 78
6.4 Results 78

7 Quantum Information Driven Ansatz (QIDA) 82
7.1 Introduction 83
7.2 QIDA 84
7.2.1 Quantum mutual information metrics 84
7.2.2 Natural orbitals 84
7.2.3 The scheme 85
7.3 Computational details 89
7.3.1 Tested Systems 89
7.3.2 Ansätze construction 89
7.4 Results 91
7.5 Conclusions 97

8 Spin-symmetric ansätze 99
8.1 Introduction 99
8.2 Spin-inversion symmetry 99
8.3 Results 103

9 Conclusions and outlook 107

10 Appendix **109**
10.1 Derivatives 109
10.2 Quantum mutual information matrices 111

Bibliography **118**

Summary

Quantum computation could give an exponential speed-up to quantum simulations. Actually, in the so-called noisy-intermediate scale quantum (NISQ) era, the available devices are composed of a few qubits, are affected by noise and are prone to decoherence. Finding a way to simulate quantum systems that can be run on these devices is not a trivial task and, to this scope, many quantum algorithms have been developed. In particular, the variational quantum eigensolver (VQE) is one of the most promising algorithms to simulate quantum systems on NISQ devices. Nevertheless, this algorithm is affected by some limitations that do not allow us to use it for practical scope. The goal of this thesis is to exploit the symmetries of the systems under consideration to find new strategies to implement the VQE algorithm. This work is divided into two parts: the first one is composed of introductory material while the second one shows the original results achieved in this work. In particular, in chapter 1 we give an overview of the most important concepts of quantum computation and quantum information while 2 illustrate some algorithms used in classical and quantum simulations. In chapter 3 we define a method that optimizes the Hamiltonian to adapt it to the wavefunction through orbital rotations. Chapter 4 improve this method by reducing the required quantum computational resources while 5 show that, for small molecules, the algorithm converges to the natural orbitals single-particle basis set. In chapter 6 the algorithm is generalized to include quasiparticles states and it is applied to SU(N) fermionic systems. Chapter 7 define a strategy to create optimal hardware-efficient ansätze starting from the correlations caught by an approximated groundstate. In chapter 8 we show how to exploit the spin symmetry of the Hamiltonian to build ansätze preserving it. Finally, in chapter 9 we summarize the obtained results and show how they open the way to future developments.

Part I

Introduction

Chapter 1

Quantum computation and quantum information

This chapter will give an overview of the basic concepts of quantum computation and quantum information that are fundamentals to understand the results shown in the next chapters [1, 2, 3].

1.1 Qubits

The building blocks of classical computation are the bits, which are variables that can assume the value 0 or 1. It is possible to define the quantum bits or qubits, that is the unit of information in the realm of quantum mechanics. Consider a two-dimensional Hilbert space $\mathscr{H}$ and define a basis as

$$|0\rangle = \begin{pmatrix} 1 \\ 0 \end{pmatrix} \qquad |1\rangle = \begin{pmatrix} 0 \\ 1 \end{pmatrix} \tag{1.1}$$

where the Dirac notation has been used. By defining the equivalence relation $\sim$ "differ by a multiplicative constant different from zero", the quotient space $\mathscr{H}/\sim$ can be defined. From now on this space will be the Hilbert space that we will consider and we will use the terms ray, vector and ket indistinctly to refer to the equivalence classes of it. These equivalence classes represent the physical states used to describe a quantum system. A generic ket can be written as

$$|\psi\rangle = \alpha\,|0\rangle + \beta\,|1\rangle \tag{1.2}$$

where $\alpha, \beta \in \mathbb{C}$ and $|\alpha|^2 + |\beta|^2 = 1$. A useful geometric representation of this ket can be given by considering the following parametrization

$$|\psi\rangle = \cos\frac{\theta}{2}\,|0\rangle + e^{i\varphi}\sin\frac{\theta}{2}\,|1\rangle \tag{1.3}$$

where $\theta \in [0, \pi]$ and $\varphi \in [0, 2\pi)$. These parameters define a point on the surface of the unit three-dimensional sphere, called Bloch Sphere, with cartesian coordinate

$$\boldsymbol{r} = (\cos\varphi \sin\theta, \sin\varphi \sin\theta, \cos\varphi) \tag{1.4}$$

This can be visualized in figure 1.1 where the basis vectors are on the vertical axis. The mapping between the space of the parameters $(\theta, \varphi) \in \mathbb{R}^2$ and the sphere $\mathbb{S}^2$ is not one-to-one because, on the poles of the sphere, φ is undetermined. This does not have physical consequences because, as explained above, we are considering a quotient space. The other kets $|\psi\rangle$ are uniquely determined by the value of the parameters θ and φ. The two-level system

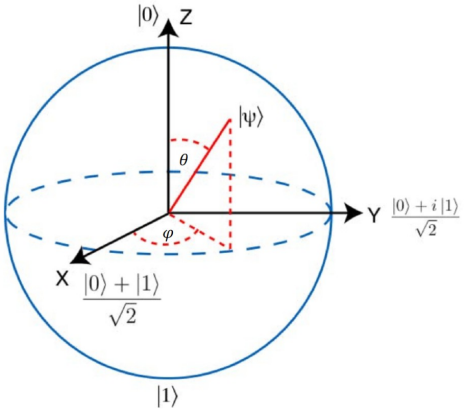

Figure 1.1: Bloch Sphere

described so far is called qubit and the vectors $|0\rangle$ and $|1\rangle$ identify the so-called computational basis. Unlike the classic bit which can assume just two values, the qubit can be in a continuum of states. In principle, this means that it is possible to associate an infinite amount of information into a qubit. To determine the values of these parameters, it is necessary to prepare an ensemble of identical systems and, through quantum tomography, perform measurements to reconstruct the state, as explained in more detail below. The ensemble is composed of a finite number of copies and as a consequence, the coefficients in formulas 1.2 and 1.3 can be determined within a certain error. Then only a finite amount of information can be encoded into a qubit. It is possible to consider a system composed of n qubits, mathematically this is represented as the product of n copies of the Hilbert space defined above

$$\mathscr{H}^n = \bigotimes_{i=1}^{n} \mathscr{H}_i \tag{1.5}$$

Physically this describes a quantum system composed of n distinguishable quantum systems. A basis of this space is composed of the 2^n kets

$$|i_1, ..., i_n\rangle = \bigotimes_{j=1}^{n} |i_j\rangle \tag{1.6}$$

where $i_j \in \{0, 1\}$ and $|\psi\rangle \in \mathscr{H}$ is a linear combination of these vectors

$$|\psi\rangle = \sum_{i_1,...,i_n=0}^{1} C_{i_1...i_n} |i_1, ..., i_n\rangle \tag{1.7}$$

with $C_{i_1...i_n} \in \mathbb{C}$ and $\sum_{i_1,...,i_n=0}^{1} |C_{i_1...i_n}|^2 = 1$. A state $|\psi\rangle$ is called separable if it can be written as

$$|\psi\rangle = \bigotimes_{j=1}^{n} |\psi_j\rangle \tag{1.8}$$

where $|\psi_j\rangle \in \mathscr{H}_j$. If this is not possible we say that the state is entangled, and thus cannot be described as a product of states of individual subsystems. As an example, consider the bipartite system $\mathscr{H}_1 \otimes \mathscr{H}_2$ composed of two qubits, the vectors of the basis are $|00\rangle, |01\rangle, |10\rangle, |11\rangle$. The state

$$|s\rangle = \frac{1}{\sqrt{2}} |0\rangle \otimes (|0\rangle + |1\rangle) \tag{1.9}$$

is a separable state while

$$|e\rangle = \frac{1}{\sqrt{2}}(|00\rangle + |11\rangle) \tag{1.10}$$

is an entangled state. This means that the qubits of the system are correlated and a measurement of one of them modifies the state of the other one.

1.2 Quantum computation

Classical circuits are made by gates and wires that manipulate and carry around the information respectively. Wires, representing the bits, are drawn with lines going from the left to the right and gates are applied on them to modify the state of one or more bits. Similarly, we define a quantum circuit made by a quantum wire for each qubit and unitary operators called, quantum gates, that modify the state of the qubits. One-qubit gates are represented as black boxes acting on a wire of the circuit

and their matrix representation is expressed in the basis of the vectors 1.6. Examples of one-qubit gates are the Pauli gates

$$X = \begin{pmatrix} 0 & 1 \\ 1 & 0 \end{pmatrix} \qquad Y = \begin{pmatrix} 0 & -i \\ i & 0 \end{pmatrix} \qquad Z = \begin{pmatrix} 1 & 0 \\ 0 & -1 \end{pmatrix} \tag{1.11}$$

that, with the identity operator, form a basis for the Hermitian matrices of dimension two and are used to implement the Hamiltonian of a quantum system on a quantum circuit. The matrices form of the useful Hadamard (H), the phase (S) and the $\pi/8$ (T) quantum gates are

$$H = \begin{pmatrix} 1 & 1 \\ 1 & -1 \end{pmatrix} \qquad S = \begin{pmatrix} 1 & 0 \\ 0 & i \end{pmatrix} \qquad T = \begin{pmatrix} 1 & 0 \\ 0 & e^{\frac{i\pi}{4}} \end{pmatrix} \tag{1.12}$$

Some quantum gates can depend on parameters, like

$$R_X(\theta) = e^{-i\frac{\theta X}{2}} = \begin{pmatrix} \cos\frac{\theta}{2} & -i\sin\frac{\theta}{2} \\ -i\sin\frac{\theta}{2} & \cos\frac{\theta}{2} \end{pmatrix} \tag{1.13}$$

$$R_Y(\theta) = e^{-i\frac{\theta Y}{2}} = \begin{pmatrix} \cos\frac{\theta}{2} & -\sin\frac{\theta}{2} \\ \sin\frac{\theta}{2} & \cos\frac{\theta}{2} \end{pmatrix} \tag{1.14}$$

$$R_Z(\theta) = e^{-i\frac{\theta Z}{2}} = \begin{pmatrix} e^{-i\frac{\theta}{2}} & 0 \\ 0 & e^{i\frac{\theta}{2}} \end{pmatrix} \tag{1.15}$$

that will be used to create parametrized ansätze of physical systems on quantum circuits. A widely used two-qubits gate is the controlled-not or CNOT gate with the following matrix representation

$$CNOT = \begin{pmatrix} 1 & 0 & 0 & 0 \\ 0 & 1 & 0 & 0 \\ 0 & 0 & 0 & 1 \\ 0 & 0 & 1 & 0 \end{pmatrix} \tag{1.16}$$

One of the qubits is called control and the other one is the target. The state of the control qubit is not modified while the state of the target change if the control is $|1\rangle$. This gate is represented as

where the black dot identifies the control and the circled cross the target qubit. Hadamard, phase, CNOT and the $\pi/8$ gates form the so-called standard set of the universal gates, this means that every unitary quantum gate

can be approximated with arbitrary error just using this set. Consider the three-bit Toffoli gate

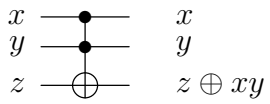

where $\oplus$ is the modulo two addition. This is a universal gate for classical computation because every gate, reversible or not, can be obtained with this. As a consequence, every classical circuit can be built just using these gates. Toffoli gate is unitary so it can be reproduced on a quantum computer, it follows that every classical circuit can be simulated on a quantum one.

1.3 Quantum information

The states considered up to now are called pure states and, for a qubit, they live on the surface of the Bloch Sphere. If a system must be considered a statistical mixture of n quantum states $|\psi_i\rangle \in \mathscr{H}$ with probability p_i, we introduce the ensemble of pure state $\{p_i, |\psi_i\rangle\}$ and define the density operator, or density matrix, as

$$\rho = \sum_{i=1}^{n} p_i \, |\psi_i\rangle \, \langle\psi_i| \tag{1.17}$$

If $n = 1$, the density operator for a pure state is obtained, otherwise we say that the system is in a mixed state. Thus, this formalism generalizes the one introduced above. If a closed system evolves under the unitary operator U, the density matrix becomes

$$\rho(U) = \sum_{i=1}^{n} p_i U \, |\psi_i\rangle \, \langle\psi_i| \, U^\dagger = U\rho U^\dagger \tag{1.18}$$

It is possible to show that an operator ρ is the density operator associated to some ensemble $\{p_i, |\psi_i\rangle\}$ if and only if:

$$tr(\rho) = 1 \qquad \wedge \qquad \langle\phi| \, \rho \, |\phi\rangle \geq 0 \quad \forall \, |\phi\rangle \in \mathscr{H} \tag{1.19}$$

By noting that $tr(\rho^2) \leq 1$, we have

- $tr(\rho^2) = 1$ for a pure state
- $tr(\rho^2) < 1$ for a mixed state

Consider the Hilbert space $L_{\mathscr{H}}$ of linear operators on $\mathscr{H}$ with the Hilbert-Schmidt inner product

$$\langle O_1, O_2 \rangle \equiv tr(O_1^\dagger O_2) \tag{1.20}$$

where $O_1, O_2 \in L_{\mathscr{H}}$. Each linear operator can be written as a linear combination of an orthonormal basis of $L_{\mathscr{H}}$. For the density operator, this basis is composed of Hermitian matrices. In particular, for a qubit, we can define the vector

$$\boldsymbol{\sigma} = \frac{1}{\sqrt{2}}(X, Y, Z, I) \tag{1.21}$$

where I is the identity matrix of dimension two and X, Y, Z are the Pauli matrices defined in 1.11. It can be easily seen that

$$\langle \sigma_i, \sigma_j \rangle = \delta_{ij} \qquad \forall i, j \in \{1, 2, 3, 4\} \tag{1.22}$$

Thus these four matrices form an orthonormal basis for the Hilbert space of the qubit and, for a n qubits system, the basis set is built by considering the tensor product of them. The density operator corresponding to a state living in $\mathscr{H}^n$ can be expanded as

$$\rho = \sum_{i_1,\dots,i_n=1}^{4} \frac{tr(\sigma_{i_1} \otimes \dots \sigma_{i_n} \rho)\sigma_{i_1} \otimes \dots \sigma_{i_n}}{2^n} \tag{1.23}$$

To univocally determine the density operator we need to obtain in some way the value of the coefficients $tr(\sigma_{i_1} \otimes \dots \sigma_{i_n} \rho)$ from the experiments. This procedure is called quantum state tomography and, to be performed, requires the concept of measurement. We start by defining a set of measurement operators $\{M_m\}$ such that

$$\sum_m M_m^\dagger M_m = I \tag{1.24}$$

where I is the identity operator and the index m refers to the measurement outcomes that can be obtained from the measure. The probability that the experiment gives the result m is

$$p(m) = tr(M_m^\dagger M_m \rho) \tag{1.25}$$

and the density operator after the measurement is

$$\rho_m = \frac{M_m \rho M_m^\dagger}{tr(M_m^\dagger M_m \rho)} \tag{1.26}$$

As an example, consider the density operator of a qubit that, from 1.23 and 1.19, can be written as

$$\rho = \frac{1}{2}(I + \sum_{i=1}^{3} r_i \sigma_i) \qquad \|\boldsymbol{r}\| \leq 1 \tag{1.27}$$

where $\boldsymbol{r} = \big(tr(X\rho), tr(Y\rho), tr(Z\rho)\big)$ is called Bloch vector and can be represented on the Block sphere: if $\|\boldsymbol{r}\| = 1$ we have a pure state on the surface of the sphere, otherwise the state is mixed and live in the interior part of it. Now we define the measurement operators in the computational basis

$$M_0 = |0\rangle\langle 0| \qquad M_1 = |1\rangle\langle 1| \tag{1.28}$$

It follows that

$$r_3 = tr(Z\rho) = tr(M_0^\dagger M_0 \rho) - tr(M_1^\dagger M_1 \rho) = p(0) - p(1) \tag{1.29}$$

Thus r_3 can be determined, within a statistical precision, by performing measurements in the computational basis on a set of qubits prepared in the same conditions. Moreover, by noting that $X = HZH$ and $Y = HSZS^\dagger H$, we deduce the following relations

$$r_1 = tr(X\rho) = tr(Z\rho_X) = p(0) - p(1) \qquad \rho_X = H\rho H \tag{1.30}$$

$$r_2 = tr(Y\rho) = tr(Z\rho_Y) = p(0) - p(1) \qquad \rho_Y = HS\rho S^\dagger H \tag{1.31}$$

To prepare ρ_X and ρ_Y on a quantum circuit, we apply respectively the quantum gates H and HS at the end of the one corresponding to the density operator ρ. Physically, this is equivalent to performing rotations along the X and Y axis on the Bloch Sphere before the measurement. So the $\boldsymbol{r}$ can be reconstructed by measuring in the computational basis the two new density operators. On a quantum circuit, the measurement operation is graphically represented with the following symbol

In conclusion, we want to resume the differences between bits and qubits. As shown in the previous sections, a qubit can be in a superposition of the states $|0\rangle, |1\rangle$ and not only assume the two mutually excluding values $0, 1$ of a classical bit. Nevertheless, giving access to the information encoded in a qubit is not trivial like for a bit because the measurement of a quantum system is involved. As an example, consider the following quantum circuit

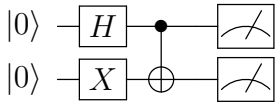

The two qubits system is initialized in the state $|\psi\rangle = |00\rangle$. After the application of the quantum gates the state becomes $|\psi\rangle = \frac{1}{\sqrt{2}}(|01\rangle + |10\rangle)$ and, to determine it, a set of measurement must be performed reinitializing the circuit after each measure.

Chapter 2

Simulating quantum systems

One of the most promising applications of quantum computation is the simulation of quantum systems. We focus our attention on quantum systems composed of atomic nuclei and electrons. In this chapter, we give an overview of some of the ab-initio classical techniques [4] used to determine the electronic structure of these systems and how a quantum computer could be useful for this purpose [5].

2.1 The electronic structure problem

Considering a system composed by M atomic nuclei and N electrons in the non-relativistic regime interacting through the Coulomb potential. In the following, capital letters refer to nuclei while lowercase ones to the electrons. To the electron $i \in 1, ..., N$ we can associate the spatial coordinate $\boldsymbol{r_i} \in \mathbb{R}^3$, in the same manner we can define the spatial coordinates $\boldsymbol{R_S} \in \mathbb{R}^3$ for the nucleus $S \in 1, ..., M$. We collect these variables with the vectors $\boldsymbol{r}$ and $\boldsymbol{R}$ respectively. Since there are no time-dependent potentials, we can write down the time-independent Schrödinger equation in the coordinate space [6]

$$\mathcal{H}\Psi(\boldsymbol{r}, \boldsymbol{R}) = \mathcal{E}\Psi(\boldsymbol{r}, \boldsymbol{R}) \tag{2.1}$$

where $\Psi(\boldsymbol{r}, \boldsymbol{R}) = \langle \boldsymbol{r}, \boldsymbol{R} | \Psi \rangle$ is an eigenfunction of the system corresponding to the ket $|\Psi\rangle$, $\mathcal{E}$ is the corresponding eigenenergy and $\mathcal{H}$ is the Hamiltonian expressed in atomic units [4]

$$\mathcal{H} = -\sum_{i=1}^{N} \frac{\nabla_i^2}{2} - \sum_{S=1}^{M} \frac{\nabla_S^2}{2M_S} - \sum_{i=1}^{N}\sum_{S=1}^{M} \frac{Z_S}{r_{iS}} + \sum_{S=1}^{M}\sum_{T>S}^{M} \frac{Z_S Z_T}{R_{ST}} + \sum_{i=1}^{N}\sum_{j>i}^{N} \frac{1}{r_{ij}} \tag{2.2}$$

M_S is the mass of nucleus S, Z_S is the atomic number of nucleus S and

$$R_{ST} = |\boldsymbol{R_S} - \boldsymbol{R_T}| \qquad R_{iS} = |\boldsymbol{r_i} - \boldsymbol{R_S}| \qquad r_{ij} = |\boldsymbol{r_i} - \boldsymbol{r_j}| \tag{2.3}$$

The electronic Hamiltonian, including all the terms depending on the electronic degree of freedom, can be defined as

$$H = -\sum_{i=1}^{N} \frac{\nabla_i^2}{2} - \sum_{i=1}^{N}\sum_{S=1}^{M} \frac{Z_S}{r_{iS}} + \sum_{i=1}^{N}\sum_{j>i}^{N} \frac{1}{r_{ij}} \tag{2.4}$$

We write the wavefunction as

$$\Psi(\boldsymbol{r}, \boldsymbol{R}) = \sum_{\alpha} C_\alpha(\boldsymbol{R})\psi_\alpha(\boldsymbol{r}, \boldsymbol{R}) \qquad \alpha = 1, 2, ... \tag{2.5}$$

where $\psi_\alpha(\boldsymbol{r}, \boldsymbol{R})$ are the electronic wavefunctions satisfying the Schrödinger equation supposing that the electrons move in the field generated by fixed nuclei

$$\left(H + \sum_{S=1}^{M}\sum_{T>S}^{M} \frac{Z_S Z_T}{R_{ST}} \right) \psi_\alpha(\boldsymbol{r}, \boldsymbol{R}) = E_\alpha(\boldsymbol{R})\psi_\alpha(\boldsymbol{r}, \boldsymbol{R}) \tag{2.6}$$

The eigenenergies $E_\alpha(\boldsymbol{R})$ and the eigenfunctions depend parametrically on the nuclear coordinates. The coefficient $C_\alpha(\boldsymbol{R})$ represent the wavefunction of the nuclear motion. Since the ratio between the electron mass and nuclear masses is $O(10^{-3}, 10^{-5})$, we can take into account the Born-Oppenheimer approximation [7]: we suppose that the nuclear motion is much slower than the electronic one, so $|\nabla_R \psi_\alpha(\boldsymbol{r}, \boldsymbol{R})| \ll |\nabla_R C_\alpha(\boldsymbol{R})|$ and the following equation is obtained

$$\left(-\sum_{S=1}^{M} \frac{\nabla_S^2}{2M_S} + E_\alpha(\boldsymbol{R}) \right) C_\alpha(\boldsymbol{R}) = \mathcal{E} C_\alpha(\boldsymbol{R}) \tag{2.7}$$

To find the solutions of 2.1 under this approximation, one solves the electronic problem and then uses the obtained information to determine the nuclear motion. From now on we fix the nuclear positions and focus on the electronic wavefunction, so we drop the $\boldsymbol{R}$ variables from the equations. Moreover, for each electron, we consider the variables

$$\boldsymbol{x_i} = (\boldsymbol{r_i}, \omega_i) \qquad i = 1, ..., N \tag{2.8}$$

,collected into the vector $\boldsymbol{x}$, to include the spin variables ω_i in our discussion. Thus given a set of fixed nuclei, the problem we want to solve is

$$\left(H + \sum_{S=1}^{M}\sum_{T>S}^{M} \frac{Z_S Z_T}{R_{ST}} \right) \psi(\boldsymbol{x}) = \mathscr{E}\psi(\boldsymbol{x}) \tag{2.9}$$

The nuclear-nuclear interaction is a constant term and will be dropped in the following discussion. Moreover, the state $|\psi\rangle$ will be used instead of

its representation in the space of the positions $\psi(\boldsymbol{x}) = \langle \boldsymbol{x}|\psi\rangle$. Now, given an Hilbert space $\mathscr{H}$, consider a complete set of orthonormal single-particle states $\{\phi_j\}$ for $j = 1, 2, ...$ It is convenient that the corresponding functions $\langle \boldsymbol{y}|\phi_j\rangle$ are chosen in order to verify the boundary condition of the Schrödinger equation: for a system in a periodic nuclear potential, we could use the Bloch wavefunctions [8] while, for a molecule, molecular spin-orbitals are a good choice. Taking into account the indistinguishability of quantum particles and the fermionic statistics of electrons, the n-particles state $|\psi\rangle$ can be expanded on this basis set

$$|\psi\rangle = \sum_{i_1>i_2>...>i_N=1}^{\infty} c_{i_1,i_2...,i_N} |i_1, i_2, ..., i_N\rangle \tag{2.10}$$

where

$$|i_1, i_2, ..., i_N\rangle = \frac{1}{\sqrt{N!}} \sum_{\sigma\in P} sgn(\sigma) \bigotimes_{j=1}^{N} |i_j\rangle \tag{2.11}$$

is called Slater determinant. P is the set of permutations of the indices $i_1, i_2, ..., i_N$ and $sgn(\sigma)$ is the signature of the permutation σ. The Slater determinants in equation 2.10 form an orthonormal basis of the antisymmetric product of N identical Hilbert spaces $\mathscr{F}^N$. To include states with different numbers of particles we define the Fock space for fermions as

$$\mathscr{F} = \bigoplus_{k=0}^{\infty} \mathscr{F}^k \tag{2.12}$$

where $\mathscr{F}^0 \equiv \mathbb{C}$ is the one-dimensional Hilbert space corresponding to the state without particles $|0\rangle$ called vacuum state. We note that to define a basis for this space, we only need the occupation of states and the order we give them. Thus, to avoid the redundancy of the notation in 2.10, we introduce the so-called occupation number representation or second quantization [9, 10, 11]. We start by defining the orthonormal basis vectors of the Fock space

$$|n_1, n_2, ..., n_\infty\rangle \tag{2.13}$$

where n_i is the number of particles in the state $i = 1, .., \infty$, so 0 or 1. A generic state in this basis can be expressed as

$$|\psi\rangle = \sum_{n_1,n_2,...,n_\infty=0}^{1} c_{n_1,n_2,...,n_\infty} |n_1, n_2, ..., n_\infty\rangle \tag{2.14}$$

Now, for each single particle state, we introduce the linear operators $a_i^\dagger$ and $(a_i^\dagger)^\dagger$ called, respectively, creation and annihilation operators. They satisfy the anticommutation relations

$$\{a_i, a_j\} = \{a_i^\dagger, a_j^\dagger\} = 0 \qquad \{a_i, a_j^\dagger\} = \delta_{ij} \qquad i, j = 1, 2, ... \tag{2.15}$$

From these algebraic relations, it is easy to show that the number operators $\hat{n}_i = a_i^\dagger a_i$ are Hermitian with eigenvalues 0 and 1. Since $[\hat{n}_i, \hat{n}_j] = 0$, it is possible to find a set of simultaneous eigenstates, with eigenvalues 0 or 1, for each operator and the states in 2.13 do this. Thus

$$\hat{n}_i \left|n_1, n_2, ..., n_\infty\right\rangle = n_i \left|n_1, n_2, ..., n_\infty\right\rangle \tag{2.16}$$

and define the vacuum state $|\varnothing\rangle$ as the one such that

$$\hat{n}_i \left|\varnothing\right\rangle = 0 \qquad \forall i = 1, 2, ... \tag{2.17}$$

All the other basis states can be obtained by the creation operators

$$\left|n_1, n_2, ..., n_\infty\right\rangle \equiv (a_1^\dagger)^{n_1}(a_2^\dagger)^{n_2}...(a_\infty^\dagger)^{n_\infty} \left|\varnothing\right\rangle = \prod_{j=1}^{\infty}(a_j^\dagger)^{n_j} \left|\varnothing\right\rangle \tag{2.18}$$

that is valid because verify the equation 2.16. Now, the effect of the application of creation and annihilation operators on the basis states can be computed directly from the 2.15

$$a_i \prod_{j=1}^{\infty}(a_j^\dagger)^{n_j} \left|\varnothing\right\rangle = (-1)^{S_i} n_i \prod_{j=1}^{\infty}(a_j^\dagger)^{n_j \oplus \delta_{ij}} \left|\varnothing\right\rangle \tag{2.19}$$

$$a_i^\dagger \prod_{j=1}^{\infty}(a_j^\dagger)^{n_j} \left|\varnothing\right\rangle = (-1)^{S_i} (n_i \oplus 1) \prod_{j=1}^{\infty}(a_j^\dagger)^{n_j \oplus \delta_{ij}} \left|\varnothing\right\rangle \tag{2.20}$$

where $\oplus$ denote the modulo two addition and $S_i = n_1 + n_2 + ...n_{i-1}$. So, a_i destroy a particle in mode i if it exists or annihilate the vacuum if it is not, $a_i^\dagger$ create a particle in the same mode if it does not exist or annihilate the vacuum if it exists. Thus, starting from the vacuum state, every state can be constructed by applying the creation operators of the mode on which we want a particle. It is possible to show [10] that the basis states 2.18 can be obtained without introducing the Fock space and the occupation number representation basis states. We just impose the relations 2.15 on an algebra of objects a_i,$a_i^\dagger$. As a consequence of the irreducibility of the representation in some vector space $\mathscr{F}$, we obtain the basis state 2.18. Now,

to conclude our discussion, we need to represent the Hamiltonian H in the second quantization. It is possible to show [9] that

$$H = \sum_{ij} h_{ij} a_i^\dagger a_j + \frac{1}{2} \sum_{klst} h_{klst} a_k^\dagger a_l^\dagger a_s a_t \tag{2.21}$$

where

$$h_{ij} = \int \phi_i^*(\boldsymbol{r}) \Big(-\frac{\nabla^2}{2} - \sum_{S=1}^{M} \frac{Z_S}{|\boldsymbol{r} - \boldsymbol{R_S}|} \Big) \phi_j(\boldsymbol{r}) d\boldsymbol{r} \tag{2.22}$$

$$h_{klst} = \int \frac{\phi_k^*(\boldsymbol{r_2}) \phi_l^*(\boldsymbol{r_1}) \phi_t(\boldsymbol{r_2}) \phi_s(\boldsymbol{r_1})}{|\boldsymbol{r_2} - \boldsymbol{r_1}|} d\boldsymbol{r_1} d\boldsymbol{r_2} \tag{2.23}$$

h_{ij} is called one-body integral and represents the kinetic and the external potential terms that, in this case, correspond to the Coulomb interaction between electrons and nuclei. h_{klst} is called two-body integral and corresponds to the Coulomb electron-electron interaction.

2.2 Classical simulations

Our goal is to find the eigenvalues and the eigenstates of the Hamiltonian operator 2.21. In particular, we focus on the groundstate, the eigenstate corresponding to the lowest eigenvalue. This section briefly illustrates some of the classical algorithms usually used in molecular systems to approximate the groundstate. First of all one need to select a finite set of M single-particle orthonormal states, the spin-orbitals $\{|\psi\rangle_i\}$ for a molecule, to which associate the set of operators $\{a_i, a_i^\dagger\}$ for $i = 1, ..., M$. Obviously, the truncation introduces an approximation because it is equivalent to set $n_i = 0$ in the linear combination 2.14 for $i > M$, we lost the completeness of the basis set. Now, the first method we investigate is the Hartree-Fock one. The idea is to find an effective Hamiltonian, quadratic in the creation and annihilation operators, such that the groundstate is supposed to approximate the one corresponding to 2.21. The advantage is that such an effective Hamiltonian can be easily diagonalized [12]. We consider a Hamiltonian that includes just terms that conserve the number of particles, even if terms that do not conserve the number of particles can also be included, as done in the BCS theory of superconductivity [13, 14]. Suppose that the effective Hamiltonian that we are looking for, written in diagonal form, is

$$H_{HF} = \sum_i \big(h_{ii} + V_{ii}^{HF} \big) a_i^\dagger a_i \tag{2.24}$$

where h_{ij} is the one-body term of 2.21 and V_{ij}^{HF} is the unknown Hartree-Fock potential that must be determined. The groundstate for a system of N particles is the Slater determinant

$$|\psi_{HF}\rangle = \prod_{\alpha=1}^{N} a_\alpha^\dagger |\varnothing\rangle \tag{2.25}$$

Now, consider the unitary transformation $U = e^k$, with $k^\dagger = -k$, then one can define the operators $b_\alpha^\dagger = \sum_i U_{i\alpha} a_i^\dagger$ that satisfy the anticommutation relations 2.15. These operators define a new basis set and we know that [15] $b_\alpha^\dagger = e^{\hat{k}} a_\alpha^\dagger e^{-\hat{k}}$, where $\hat{k} = \sum_{ij} k_{ij} a_i^\dagger a_j$. The Slater determinants

$$|\psi_{HF}(k)\rangle = \prod_{\alpha=1}^{N} b_\alpha^\dagger |\varnothing\rangle = e^{\sum_{ij} k_{ij} a_i^\dagger a_j} |\psi_{HF}\rangle \tag{2.26}$$

are the groundstate of other effective Hamiltonians diagonal in $b^\dagger$ operators. The groundstate of 2.24 is the best approximation of the one of the Hamiltonian thus the expectation value of the energy $E(k) = \langle\psi_{HF}(k)| H |\psi_{HF}(k)\rangle$ has a minimum in $k = 0$. From the necessary conditions for a minimum $\frac{dE(k)}{dk} = 0$, one obtains

$$h_{ij} + \sum_{l=1}^{N} (h_{illj} - h_{iljl}) = 0 \qquad i \neq j \tag{2.27}$$

Comparing with 2.24, one finds that, defining $V_{ij}^{HF} = \sum_{l=1}^{N} (h_{illj} - h_{iljl})$, the unitary transformation that diagonalizes the effective Hamiltonian is the one that verifies the optimum condition. This potential and the one-body term both depend on the chosen basis set thus, to find the solution, the self-consistency condition must be satisfied. In practice, we start from a basis set and calculate h_{ij} and V_{ij}^{HF}, then diagonalize the effective Hamiltonian to obtain a new basis set and the cycle starts again until convergence is reached. The Hartree-Fock energy is

$$E_{HF} = \langle\psi_{HF}| H |\psi_{HF}\rangle = \sum_{i}^{N} (h_{ii} + \frac{1}{2} V_{ii}^{HF}) \tag{2.28}$$

and the correlation energy is defined as $E_{corr} = \mathscr{E} - E_{HF}$ when $M \to \infty$, where $\mathscr{E}$ is the groundstate energy. Since the size of the basis set is fixed at the beginning of our calculations, we refer $E_{corr}, \mathscr{E}, E_{HF}$ to a basis composed by M states. Hatree-Fock method is a mean-field theory, this can be

inferred by factorizing the Hamiltonian [16]. By using the Wick theorem, the Hamiltonian 2.21 can be written as

$$H = \sum_{ij}(h_{ij} + V_{ij}^{HF})a_i^\dagger a_j + \sum_{klst} h_{klst} : a_k^\dagger a_l^\dagger a_s a_t : -\frac{1}{2}\sum_{i=1}^{N} V_{ii}^{HF} \tag{2.29}$$

where the last term is just a constant while the first one includes the one-body part of the two-body interaction through V^{HF}. The second term contains the operators normal ordered with respect to the Hartree-Fock state and represents the true two-body interaction because, when acting on $|\psi_{HF}\rangle$, promotes two electrons from occupied to empty states. Thus this term does not contribute to $E(0)$ and $\frac{dE(k)}{dk}|_{k=0}$, if we neglect this fluctuation in the Hamiltonian the 2.24 is recovered. With this procedure, we obtained a set of M single-particle states that can be used as starting point for the post-Hartree-Fock methods, used in quantum chemistry, which we illustrate in the following. First of all, we note that, for a system composed of N particles, a set of $\binom{M}{N}$ different Slater determinants can be constructed. The configuration interaction (CI) method writes down the wavefunction of the system as

$$|\psi_{FCI}\rangle = \sum_{i_N>\ldots>i_2>i_1=1}^{M} c_{i_1,i_2,\ldots,i_N} \prod_{j=1}^{N} a_{i_j}^\dagger |\varnothing\rangle \tag{2.30}$$

and find the values of the coefficients of this expansion corresponding to the groundstate. This method is named full CI because all the determinants are included. The full CI groundstate is exact within the subspace spanned by the one-electron basis and is used as a reference for the other methods. Even for small systems and M, the number of determinants is huge and the simulation is classically intractable. Thus, one truncates the expansion by considering a small number of excitations above the Hartree-Fock state: CISD include single and double excitations, CISDT add triple excitations and so on. Suppose that we know the groundstate of the system $|\psi_{GS}\rangle$. We can define the set of natural orbitals $\{b_i^\dagger\}$ from the relation

$$b_i = \sum_j U_{ji} a_j \qquad \text{such that} \qquad D = U^\dagger \gamma U \tag{2.31}$$

where D is a diagonal matrix and U is the unitary matrix that diagonalizes the first-order reduced density matrix $\gamma_{ij} = \langle\psi_{GS}| a_j^\dagger a_i |\psi_{GS}\rangle$. This new set is important because to obtain a given accuracy with the CI method, one requires fewer configurations formed from natural orbitals than configurations formed from any other orthonormal basis set [17]. Since the natural orbitals can be obtained only if one knows the groundstate, many strategies have been

developed to approximate them. For example, one could perform a CI calculation with a small number of Slater determinants. Then one constructs the γ matrix from the obtained state, diagonalizes it and finds a set of approximated natural orbitals that construct the new determinants [18]. The cycle is repeated until energy or natural orbitals converge. So the Hartree-Fock spin-orbitals are not the best choice, thus they can be optimised together with the coefficient of a multiconfiguration expansion. This method, called multiconfiguration self-consistence field (MCSCF), considers the state

$$|\psi_{MCSCF}\rangle = e^{\sum_{ij} k_{ij} a_i^\dagger a_j} \sum_\alpha C_\alpha |\alpha\rangle \tag{2.32}$$

and optimize both set of parameters k and C_α, where $|\alpha\rangle$ are the configurations under consideration. If the number of determinants is just one the method reduces to the Hartree-Fock one. Finally, we introduce the coupled cluster method (CC), initially developed for nuclear physics [19, 20] and then applied to study molecules [21]. CC take into account an ansatz with the following form

$$|\psi_{CC}\rangle = e^T |\psi_{HF}\rangle \qquad T = \sum_k T_k \tag{2.33}$$

with

$$T_n = \sum_{i_1,...i_n \in unocc} \sum_{j_1,...,j_n \in occ} t_{i_1...1_n}^{j_1...j_n} a_{i_1}^\dagger ... a_{i_n}^\dagger a_{j_1} ... a_{j_n} \tag{2.34}$$

where *occ* and *unocc* indicate respectively the occupied orbitals and the unoccupied one respect $|\psi_{HF}\rangle$. Usually, just the T_1 and T_2 operators are considered in the exponential (CCSD). If all the excitations are included the $|\psi_{FCI}\rangle$ is recovered. The CC method generates an ansatz that includes all the determinants and then converges faster than the CI one. Nevertheless, the method is not variational [15] and is suitable for multireference states. To overcome these problems the unitary coupled cluster has been developed (UCC). This method is exponentially costly to implement with a classical computer while it is efficient to do on a quantum computer and, for this reason, will be described in the next section.

2.3 Quantum simulations

Noisy Intermediate-Scale Quantum (NISQ) devices are quantum computers composed of $\mathcal{O}(10^2)$ qubits that are not fault-tolerant [22]. In this section, we show how to encode an electronic structure problem in second quantization on a quantum computer and illustrate one of the most promising algorithms for NISQ devices: the variational quantum eigensolver (VQE) algorithm.

2.3.1 Encoding methods

To simulate a quantum system on a quantum computer, the Fock space 2.12 must be encoded on the Hilbert space of qubits 1.5. In other words, an encoding method is a map from the states of indistinguishable fermions to states of distinguishable qubits. To perform any computational task both the states and the operators must be mapped. In the following, we consider a system composed of M single-particle quantum state and N particles.

In the Jordan-Wigner encoding method [23] the occupation number of a single-particle quantum state is stored in the state of a qubit: $|0\rangle$ if the state is unoccupied and $|1\rangle$ if it is occupied

$$|n_1, n_2, ..., n_M\rangle \to |q_1, q_2, ..., q_M\rangle \qquad n_k = q_k \in \{0, 1\} \tag{2.35}$$

where n_k is the number of particles in state k and q_k is the state of the k-qubit, with $k = 1, 2, ..., M$. To map the Hamiltonian we need to encode the creation and annihilation operators, this can be done by considering how they act on a quantum state 2.20. Taking into account these considerations one obtains that

$$a_k \to Z_1 \otimes ... \otimes Z_{k-1} \otimes Q_k \tag{2.36}$$

$$a_k^\dagger \to Z_1 \otimes ... \otimes Z_{k-1} \otimes Q_k^\dagger \tag{2.37}$$

where the strings of Pauli operator Z recover the phase factor due to the anticommutation fermionic relations $(-1)^{\sum_{k=1}^{k-1} n_k}$ and

$$Q = |0\rangle \langle 1| = \frac{1}{2}(X + iY) \tag{2.38}$$

Thus the Hamiltonian is mapped to a linear combination of products of Pauli operators

$$H_q = \sum_l h_l \bigotimes_k \sigma_k^l \tag{2.39}$$

where h_j are coefficients associated to the Pauli string j and $\sigma_k^j \in \{X, Y, Z, I\}$. The advantage of the Jordan-Wigner encoding is the readability of the states because the occupation number is stored locally. Nevertheless, the parity is stored non-locally and computes the phase due to the application of a fermionic operator requiring the application of $O(M)$ operators.

In the parity encoding [24], the k^{th} qubit store the parity of all the states up to

$$|n_1, n_2, ..., n_M\rangle \to |q_1, q_2, ..., q_M\rangle \qquad q_k = \oplus_{k=1}^k n_k \tag{2.40}$$

where $\oplus$ denotes the module two addition. The creation and annihilation operators become

$$a_k \to \frac{1}{2}\big(Z_{k-1} \otimes X_k + iY_k\big) \otimes_{l=k+1}^{n} X_l \tag{2.41}$$

$$a_k^\dagger \to \frac{1}{2}\big(Z_{k-1} \otimes X_k - iY_k\big) \otimes_{l=k+1}^{n} X_l \tag{2.42}$$

and, in this case, the occupation number is non-locally stored.

The exact solution to our problem, the $|\psi_{FCI}\rangle$ state, is a linear combination of $O(M^N)$ determinants [25]. Because of this exponential scaling, even for small systems, the FCI solution can not be calculated on a classical computer. Nevertheless, a register of M qubits can be in a superposition of 2^M states, which means that a quantum computer can store the FCI solution in this quantum register. There exist other encoding methods as the Bravyi-Kitaev [26], that partially store on each qubit the parity and the occupation number, or [27] that efficiently encode the entire set of basis states. Mappings that reduce the number of qubits by taking advantage of some symmetry have been developed [28, 29] such as encoding methods that overcome the problem of the non-locality of the qubit Hamiltonian [30, 31, 32, 33, 34].

2.3.2 Variational quantum eigensolver

The variational quantum eigensolver (VQE) algorithm is one of the most promising that has been developed to determine the groundstate of a quantum system on NISQ devices [35, 36] because it does not require long coherence times compared to other algorithms like quantum phase estimation [37]. VQE is a hybrid quantum-classical algorithm that exploits the variational principle [6] to approximate the groundstate energy $\mathscr{E}$ with

$$\langle\psi(\boldsymbol{\theta})|\, H\, |\psi(\boldsymbol{\theta})\rangle \geq \mathscr{E} \tag{2.43}$$

where $\boldsymbol{\theta} \in \mathbb{R}^k$ is a set of k parameters and $|\psi(\boldsymbol{\theta})\rangle$ is a trial state called ansatz. As shown in figure 2.1, the algorithm is divided into three steps:

- prepare the state $|\psi(\boldsymbol{\theta})\rangle$ on a quantum computer. This is done by initializing the qubit in a reference state $|ref\rangle$, usually all qubits are in the state $|0\rangle$, and by applying a set of parametrized quantum gates $U(\theta_i)$ such that

$$|\psi(\boldsymbol{\theta})\rangle = U(\theta_k)U(\theta_{k-1})...U(\theta_1)\,|ref\rangle \tag{2.44}$$

- The Hamiltonian is mapped on qubits and the expectation values of the strings appearing in 2.39 are determined on the state $|\psi(\boldsymbol{\theta})\rangle$ by repeating the measurement process many times. This step, as the previous one, is executed on the quantum computer.

- The expectation value of the energy is reconstructed from the measurement process executed in the previous step

$$\langle\psi(\boldsymbol{\theta})| H |\psi(\boldsymbol{\theta})\rangle = \sum_j h_j \bigotimes_k \langle\psi(\boldsymbol{\theta})| \sigma_k^j |\psi(\boldsymbol{\theta})\rangle \tag{2.45}$$

  The number of measurements needed to determine the energy with a precision ϵ scale as $O(\frac{1}{\epsilon^2})$ [36, 38]. The vector of parameters $\boldsymbol{\theta}$ is updated by using a classical optimization method. This final step is the one executed on a classical computer and makes the algorithm hybrid.

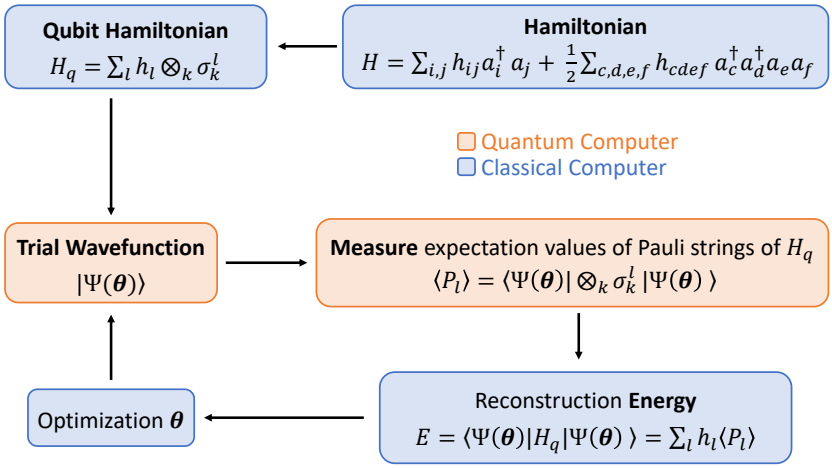

Figure 2.1: Scheme of the VQE algorithm described in text.

The three steps are repeated until energy convergence is reached. The construction of the ansatz is fundamental because determines the subset of Fock space spanned by the parameters. The ansätze can be divided into two main classes: the physically or chemically inspired ansätze and the hardware efficient ones. There are ansätze that lie between the two classes, as [39], that we do not consider because out of the scope of the discussion. The first class of ansätze adapt classical algorithms to run efficiently on quantum hardware. In particular, taking inspiration from the unitary coupled cluster method [40, 41], it can be defined the corresponding ansatz (UCC)

$$|\psi(\boldsymbol{\theta})\rangle = e^{T(\boldsymbol{\theta})-T(\boldsymbol{\theta})^\dagger} |ref\rangle \qquad T = \sum_i T_i \tag{2.46}$$

with

$$T_n = \sum_{i_1,...i_n \in unocc} \sum_{j_1,...,j_n \in occ} \theta^{j_1...j_n}_{i_1...1_n} a^\dagger_{i_1} ... a^\dagger_{i_n} a_{j_1} ... a_{j_n} \tag{2.47}$$

where *occ* and *unocc* indicate respectively the occupied states and the unoccupied one with respect to $|ref\rangle$. Usually, just single and double excitations are considered (UCCSD) and a review of the application to quantum chemistry can be found in [38]. The hardware efficient ansätze are composed of repeated blocks of quantum gates that are easy to implement on the quantum device as, for example, the circuit shown in figure 3.2. If the parameters are randomly initialized, the gradients strive to vanish [42] but, to overcome this problem, techniques have been proposed [43]. It has been demonstrated that they can be used to determine the groundstate of small molecules [44]. Compared to the hardware efficient ansätze, the UCC ones require the implementation of much more quantum gates and parameters. For these reasons, we decided to focus our work on the hardware efficient ansätze.

2.3.3 Final considerations

The model of computation described until now belong to the realm of the digital quantum simulations that maps the target problem onto a set of gates which a quantum computer can implement. The NISQ digital hardware suffers from some limitations: they are small because composed of $\mathcal{O}(10^2)$ qubits, the decoherence affects the qubits state, the quantum gates are noisy and there are errors in the measurement process. Quantum error correction cannot be used in these devices [22] but error mitigation techniques can be taken into consideration. [45, 46]

Classical simulators of quantum computers have been developed to avoid problems related to the imperfection of the actual hardware. State vector simulators simply represent quantum states as vectors of 2^N components for N qubits circuit, physically they are equivalent to an ideal quantum computer that executes an infinite number of measurements. Obviously, the required memory is exponential in the number of qubits, making it possible to use these simulators only on circuits with a small number of qubits. Measurement-based simulators work as ideal quantum devices, thus the number of times that a circuit is repeated limits the performed measurement introducing a statistical noise into the results. By introducing noise models into the measurement-based simulators, it is possible to simulate real devices. To implement a new algorithm the first step is to test it on benchmark systems using a state vector simulator and, if it works, go ahead to include statistical and hardware noise.

Despite its wide use, the VQE algorithm presents some problems: many measurements are required, the classical optimization procedure must optimize many parameters and the hardware limitations illustrated above affect the results. In part II of this work we show the strategies that we developed to try to overcome these problems by defining methods to develop hardware-efficient ansatz or by applying unitary operators to the Hamiltonian, as will be explained in detail later. Except where expressly stated, the results described below were obtained with simulations state vector to test the potentialities of the methods on small molecules and model Hamiltonians.

Part II

Results

Chapter 3

Wavefunction Adapted Hamiltonian Through Orbital Rotations (WAHTOR)

The use of Variational Quantum Eigensolver (VQE) for Quantum Chemistry is one of the most promising applications for Noisy Intermediate-Scale Quantum (NISQ) devices. A major limitation is represented by the need to build compact and shallow circuits ansätze having the variational flexibility to catch the complexity of the electronic structure problem. To alleviate this drawback we introduce a modified VQE scheme in which the form of the molecular Hamiltonian is adapted to the circuit ansatz through an optimization procedure. Exploiting the invariance of the Hamiltonian by molecular orbital rotations we can optimize it using gradients that can be calculated without significant computational overload. The proposed method, named Wavefunction-Adapted Hamiltonian Through Orbital Rotation (WAHTOR), is applied to small molecules in numerical state vector simulations. The results demonstrate that, at variance with standard VQE, the method is less dependent on circuit topology and less prone to be trapped into high-energy local minima. It is able to recover a significant amount of electron correlation even with only empirical ansätze with shallow circuit depth. Noisy calculations demonstrate the robustness and feasibility of the proposed methodology and indicate the hardware requirements to effectively apply the procedure using forthcoming NISQ devices.

3.1 Introduction

Computational Quantum Chemistry is among the most promising application that quantum computers will be able to tackle in the following years [47, 22]. As example, Proof-of-concepts calculations solving the time-independent Scrödinger equation for small molecular systems has paved the way for the development of robust and efficient algorithms that can exploit the exponential speed-up offered by quantum co-processors [48, 49, 50]. To exploit the capabilities of the quantum computing devices, the original eigenvalue problem involving the molecular Hamiltonian acting on fermionic particles has to be reformulated in terms of a qubit Hamiltonian using different mapping schemes such as Jordan-Wigner [23], Bravyi-Kitaev [26], or parity [24]. The resulting qubit Hamiltonian is a cost function composed by a sum of Pauli strings, that can be tackled by different quantum algorithms such as the phase estimator [51, 52, 53, 54, 25, 55] and the Variational Quantum Eigensolver (VQE) [56, 35, 57]. The ground state energy is estimated using the variational principle by measuring expectation values of the Pauli strings on a parametrized quantum circuit, i.e. wavefunction ansatz [50]. The choice of such ansatz turned to be crucial for the effectiveness of the procedure. Many proposed circuits are inspired by theoretical techniques used in quantum chemistry [58, 59, 60, 38, 61, 62]. Another class of circuits, the so-called heuristic ansätze are, on the contrary, build on hardware capabilities, regardless of the chemical interpretation. Although for the quantum-chemistry-inspired circuits approximations and accuracies are under control, such circuits are longer than the heuristic ones, which can provide, in general, better results at the same cost in terms of circuit depth [44, 63]. Since the short coherence time and/or the high level of noise is limiting the depth of the circuits (i.e. wavefunctions) that can be effectively evaluated on quantum computers, the search for compact circuit ansätze is a crucial issue for Theoretical Chemistry. To achieve this goal, it has been also recently proposed a strategy based on the optimization of non-unitary wavefunction through the nu-VQE method [64, 65]. In addition to its influence on noise level and decoherence, circuit length is also related to the problem of the presence of barren plateau in the energy landscape [66]. In the present work, we propose a method to enhance the effectiveness of any given variational ansatz by optimizing the Molecular Hamiltonian together with the variational parameters. We exploited the invariance of the Hamiltonian under molecular orbitals transformation in order to adapt its formulation to circuits with limited number of gates and parameters [67]. The optimization of the orbitals has been already proposed by W. Mizukami and coworkers with an approximate approach in the context of the UCC (Unitary Coupled

Cluster) ansätze [68]. Here, we fully exploit the potential of this additional optimization strategy by applying a general unitary transformation to the molecular orbitals using hardware-inspired ansätze. As shown in the present work, our approach is not only able to achieve a lower variational energy with respect to standard VQE, but it possesses the capability to significantly reduce the depth of the circuits as well as to alleviate the problems of being trapped into local minima.

The algorithm is described in the next section whereas in 3.3 are reported the computational details of the calculations and a full description of the anzätze we have used. Results and conclusions are following in section 3.4 and 3.5.

3.2 The WAHTOR algorithm

In this section, we will illustrate the algorithm we have developed to variationally adapt the molecular Hamiltonian to a given wavefunction ansatz using an optimization procedure based on orbital rotations which is driven by the calculations of energy gradients. The electronic molecular Hamiltonian is written as $H = T + V + U_e$, where T is the kinetic energy operator for electrons, V is the external potential operator due to the interaction with nuclei and external fields and U_e is the electron-electron interaction operator. Given a basis set of m orbitals $|i\rangle$ with $i = 0, .., m$, the electronic molecular Hamiltonian in second quantization is given by:

$$H = \sum_{i,j} h_{ij} a_i^\dagger a_j + \frac{1}{2} \sum_{c,d,e,f} h_{cdef} a_c^\dagger a_d^\dagger a_e a_f \tag{3.1}$$

where $i, j, c, d, e, f = 0, .., m$ and a_i,$a_i^\dagger$ are the annihilation and creation operators of an electron on the i^{th} orbital respectively and

$$h_{ij} = \langle i| \, T + V \, |j\rangle \, ; \quad h_{cdef} = \langle cd| \, U_e \, |fe\rangle \tag{3.2}$$

are the one-body and two-bodies integrals. We can transform this fermionic Molecular Hamiltonian in a corresponding bosonic Qubit Hamiltonian using an encoding method such as Jordan-Wigner [23], parity [28] or Bravyi-Kitaev mappings. [24] After these transformations the Hamiltonian can be represented in terms of Qubits:

$$H_q = \sum_l \hat{h}_l \bigotimes_k \sigma_k^l \tag{3.3}$$

where $\hat{h}_l$ represents the one-body and two bodies integrals upon mapping transformations and σ_k^l are the Pauli matrices. The sum is running over

a single index l which is of the order of 4^m, where m is the basis set size. Here, we point out that since the spectrum of the original Molecular Hamiltonian Eq. 3.1 is invariant upon a linear combination of the orbitals, also the transformed Qubit Hamiltonian Eq. 3.3 will not be univocally defined. If we introduce a unitary transformation U (namely a rotation) of the original orbitals such as:

$$|i\rangle = \sum_{\alpha} U_{\alpha i} |\alpha\rangle \tag{3.4}$$

both Hamiltonians H and H_q will change, without changing their corresponding eigenvalues. The main idea of the present paper comes from the fact that, although all the resulting rotated Hamiltonians are in principle equivalents, they are in general *not equivalent when evaluated on a given variational ansatz*. We can therefore use this additional flexibility to optimize the unitary operator U for a given variational ansatz (such as for instance the heuristic ansatz in refs. [44, 69]). Since the creation and annihilation operators of the orbitals of the two basis are related by the following transformation rules

$$a_i^\dagger = \sum_{\alpha} a_\alpha^\dagger U_{\alpha i}; \quad a_i = \sum_{\alpha} a_\alpha U_{i\alpha}^\dagger \tag{3.5}$$

the Hamiltonian in the new basis can be now written as:

$$H = \sum_{\alpha,\beta} h_{\alpha\beta} a_\alpha^\dagger a_\beta + \frac{1}{2} \sum_{\gamma,\delta,\epsilon,\zeta} h_{\gamma\delta\epsilon\zeta} a_\gamma^\dagger a_\delta^\dagger a_\epsilon a_\zeta \tag{3.6}$$

where

$$h_{\alpha\beta} = U_{\alpha i} h_{ij} U_{j\beta}^\dagger; \quad h_{\gamma\delta\epsilon\zeta} = U_{\gamma c} U_{\delta d} h_{cdef} U_{e\epsilon}^\dagger U_{f\zeta}^\dagger \tag{3.7}$$

A generic unitary matrix U can be expressed, as a consequence of the Spectral Theorem [1] in the following form:

$$U = e^{i\boldsymbol{R}\cdot\boldsymbol{T}} = U(\boldsymbol{R}) \tag{3.8}$$

where $\boldsymbol{T}$ is a complete set of Hermitian $m \times m$ matrices and $\boldsymbol{R} \in \mathbb{R}^{m^2}$. Using such representation the Hamiltonian can be now expressed as a function of the real vector $\boldsymbol{R}$:

$$H(\boldsymbol{R}) = \sum_{\alpha,\beta} h(\boldsymbol{R})_{\alpha\beta} a_\alpha^\dagger a_\beta + \frac{1}{2} \sum_{\gamma,\delta,\epsilon,\zeta} h(\boldsymbol{R})_{\gamma\delta\epsilon\zeta} a_\gamma^\dagger a_\delta^\dagger a_\epsilon a_\zeta \tag{3.9}$$

A generic wavefunction ansatz can be expressed as $|\Psi(\boldsymbol{\theta})\rangle = O(\boldsymbol{\theta}) |ref\rangle$, with $O(\boldsymbol{\theta})$ an operator that depends on $\boldsymbol{\theta}$ variational parameters and $|ref\rangle$ the reference initial state (for instance the HF state). Given a certain $\boldsymbol{R}$

(i.e. fixing the Hamiltonians), the standard Variational Quantum Eigensolver algorithm can be used to minimize the energy expectation value $E(\boldsymbol{R}, \boldsymbol{\theta}) = \langle \Psi(\boldsymbol{\theta}) | H(\boldsymbol{R}) | \Psi(\boldsymbol{\theta}) \rangle$ as a function of the ansatz parameters $\boldsymbol{\theta}$:

$$E[|\Psi\rangle_{\boldsymbol{R}}, \boldsymbol{R}] = \langle \Psi |_{\boldsymbol{R}} H(\boldsymbol{R}) |\Psi\rangle_{\boldsymbol{R}} \tag{3.10}$$

where $|\Psi\rangle_{\boldsymbol{R}} = |\Psi(\boldsymbol{\theta_{opt}})\rangle$ represent the wavefunction that minimize the energy for fixed $\boldsymbol{R}$ and parametrically depends on those parameters. We obtained a functional that depends on $\boldsymbol{R}$ explicitly and impicitly, indicated here by $E(\boldsymbol{R}) = E[|\Psi\rangle_{\boldsymbol{R}}, \boldsymbol{R}]$. Keeping in mind that at fixed $\boldsymbol{R}$ the energy is optimized with respect to the $\boldsymbol{\theta}$ parameters, by using the Hellmann-Feynman theorem, it is possible to calculate explicitly the derivative of the expectation value of the energy with respect to the Hamiltonian parameters $\boldsymbol{R}$:

$$\frac{dE(\boldsymbol{R})}{d\boldsymbol{R}} = \langle \Psi |_{\boldsymbol{R}} \frac{dH(\boldsymbol{R})}{d\boldsymbol{R}} |\Psi\rangle_{\boldsymbol{R}} = \sum_l \frac{d\hat{h}_l(\boldsymbol{R})}{d\boldsymbol{R}} \bigotimes_k \langle \Psi |_{\boldsymbol{R}} \sigma_k^l |\Psi\rangle_{\boldsymbol{R}} \tag{3.11}$$

The above equation shows that to evaluate these derivatives is necessary to calculate a weighted average of expectation values of Pauli strings, analogously to what has been already calculated in the VQE algorithm [70, 36, 71]. Remarkably, the number of the Pauli strings scale as 4^m, where m is the basis set size, as for the standard VQE procedure. For this reason, as discussed in the next sections, the additional computational cost requested for the gradient evaluation is only a small additional overload for the quantum processor. Following the gradients calculated in Eq. 3.11, the $\boldsymbol{R}$ vector can be therefore updated to minimize the total energy with respect to these external parameters. The new Hamiltonian can be therefore optimized again with respect to the wavefunction parameters $\boldsymbol{\theta}$ by a standard VQE and the procedure can be iterated until convergence threshold is reached. A scheme of the method is illustrated in Figure 3.1.

3.3 Computational details

Simulated systems.
The molecular Hamiltonian in Eq. 3.1 is calculated using the PySCF Python package [72]. The reference value of the correlation energy, i.e. the exact energy, is calculated by full-CI. The percentage of recovered correlation energy is estimated as follows:

$$E_{corr} = \frac{E_{calculated} - E_{HF}}{E_{full-CI} - E_{HF}} \tag{3.12}$$

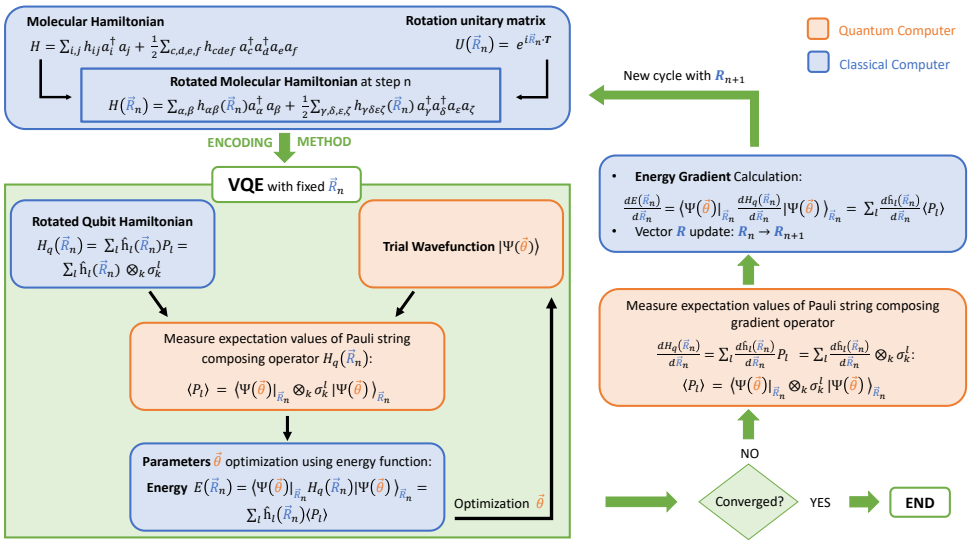

Figure 3.1: Wavefunction-Adapted Hamiltonian Though Orbital Rotations (WAHTOR). Exploiting the invariance of the Molecular Hamiltonian by orbital unitary transformation $U(\boldsymbol{R})$, we optimized the variational parameters $\boldsymbol{R}$ using the energy gradient of optimized VQE ansätze. The procedure is iterated as detailed in the above scheme.

where $E_{full-CI}$ is the exact energy, $E_{calculated}$ is the energy calculated using VQE or WAHTOR algorithm and E_{HF} is the Hartree-Fock energy. The corresponding qubit Hamiltonian (Eq. 3.3) is calculated using Qiskit Python package [73] with three different mapping schemes: Jordan Wigner (JW) [23], parity (P) [28] and Bravyi-Kitaev (BK)[26]. The majority of the simulations are carried out using JW mapping since it better preserves the physical meaning of the systems under consideration. The WAHTOR algorithm has been implemented by a Python program exploiting the QuTip [74, 75] and Qiskit [73] Python libraries. According to the molecule, the mapping and the choice of the basis set, we have considered four different molecular systems, ranging from 8 to 12 qubits:

- H_2-8qubits: molecular hydrogen at the equilibrium distance of 0.74 Å. We used the 6-31g basis set with three different mappings (JW,P,BK).
- LiH-12qubits: lithium hydride at the equilibrium distance of 1.595 Å. We used the sto-3g basis set with three different mappings (JW,P,BK).
- LiH-10qubits: same system as before but using parity mapping with the two qubits reduction. [28]

- H_4-8qubits: dissociation curve of the square H_4 molecule as example of strongly correlated system. We used sto-3g basis set and JW mapping.

Wavefunction ansätze.
As parametrized quantum circuit we have chosen the heuristic ansatz [44] which is built as follows: starting from the n-qubit Hartree-Fock reference state, single qubit rotations around y axis are applied, each one by a different angle θ. After such rotations, an entangling block composed by CNOT gates followed by another set of independent rotations on each qubit is applied, as reported in Figure 3.2. This entangling block (n Ry + $n-1$ CNOT gates)

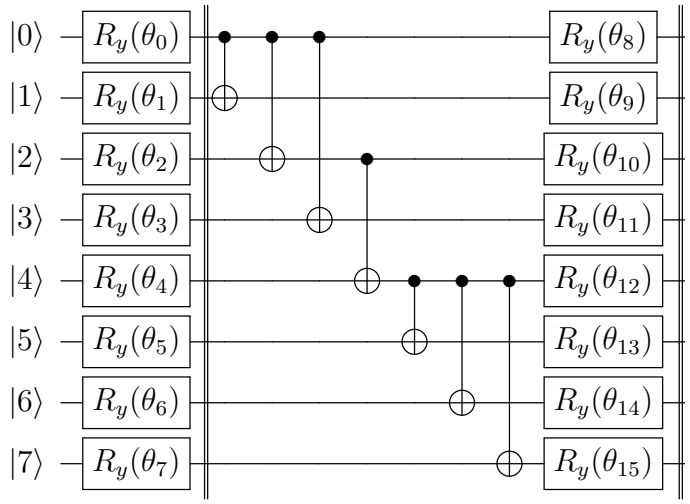

Figure 3.2: Circuit ansatz for 8 qubits with 8 initial rotations around the y-axis, 1 entangling block composed by 7 CNOTs gates and another set of 8 rotations around the y-axis.

can be therefore repeated a number of times, each one using different variational parameters. The total number of blocks determines the circuit depth. In particular, in our simulations, we consider mainly heuristic ansatzes with depth 2. One important issue we have investigated is that the arrangement of the CNOT gates in the block, referred hereafter as the entangler map, is an important topological variable of the ansatz that can deeply influence the variational energy. To investigate the effect of CNOT topology on the VQE and WAHTOR optimization for the H_2-8qubits system (data reported in Figure 3.5(a)), we considered a particular set of 144 entangler maps selected as described below. As shown in Figure 3.3, qubits are arranged such that qubits from 0 to 3 represent spin-up orbitals (orange registers), whereas qubits from

4 to 7 represent spin-down orbitals (green registers). The target qubits of all the 7 CNOTs are taken fixed in a ladder-type scheme, whereas the control qubits of each CNOT are varied among all the combinations described by the squares of Figure 3.3. Following these rules, we therefore considered 144 possible circuits. On the right side of the figure, three of such realizations are displayed as examples. Each entangler map is distinguished by a list of

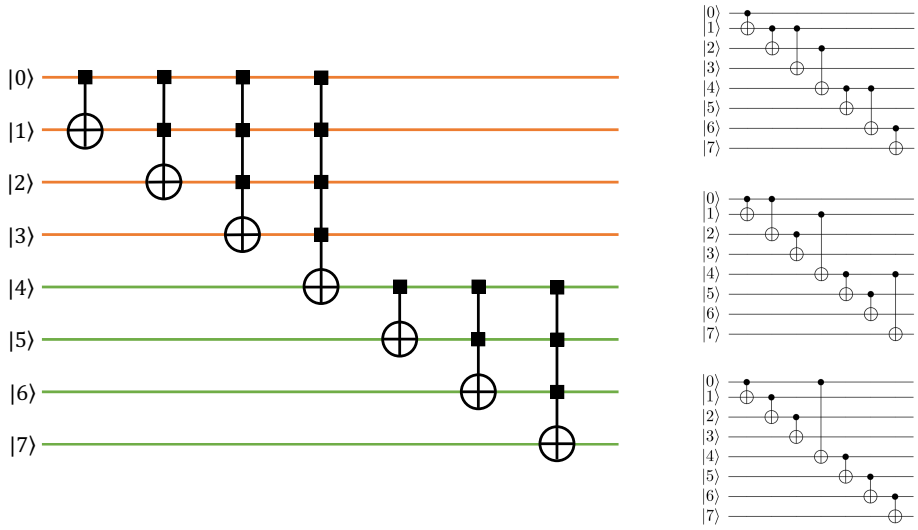

Figure 3.3: Scheme of construction of the entangler maps for H_2-8qubits calculations: the orange (spin up) and green (spin down) qubits are entangled using 7 CNOTs such that the target qubits of each CNOT are kept fixed and the control is varying. On the right are displayed, as an example, 3 out of 144 of such entangler maps.

number pairs, for instance $[[0,1],[0,2],[0,3],[2,4],[4,5],[4,6],[4,7]]$, in which each pair of numbers represent a CNOT gate having as control the first qubit and as target the second.

VQE and WAHTOR optimization and computational details.
For the VQE calculations, the initial rotation angles $\boldsymbol{\theta}$ of the chosen ansatz are generated randomly in the range $[0, 2\pi]$. For each ansatz we have reported the best energy obtained by 50 independent VQE calculations. As VQE optimizers we have used the L-BFGS-B [76] algorithm for state vector calculations and COBYLA [77] or L-BFGS-B [76] for the measure-based simulations, for which we used the QASM simulator of Qiskit [73]. The parameters were optimized up to a convergence threshold 10^{-8} Hartree. In the case of H_4-8qubits system, we have observed that HF orbitals were not a good

starting point, probably the due to the extreme multi-determinant character of the ground state. We have therefore decided to change our starting point for WAHTOR optimization by considering the localized molecular orbitals obtained using the *Boys* criterion [78], since localized orbitals let correlated systems be more computationally tractable [79, 80]. All WAHTOR calculations have been set up starting from the best VQE result and following a simple steepest descent procedure to optimize the $\boldsymbol{R}$ parameters according to the scheme illustrated in Figure 3.1.

3.4 Results

3.4.1 State Vector Simulations

We apply the new developed WAHTOR method and the traditional VQE to study two molecules: molecular hydrogen H_2-8qubits and lithium hydride LiH-12/10qubits. We used here an empirical ansatz defined by one or more blocks, each one built by a set of single qubit rotations followed by an entangling map of CNOTs connecting all qubits. As detailed before, the WAHTOR algorithm uses the gradient with respect to the parameters of the orbital rotation matrix to rotate the molecular Hamiltonian in order to 'adapt it' to the wavefunction ansatz. A remarkable and unique feature of such procedure is that the optimization is done adiabatically, i.e. the orbital and circuit parameters are always taken from the previous run, without the necessity to explore a large number of different starting points for the VQE parameters, as often happens to avoid local minima [64, 65]. We first consider noiseless simulations. To illustrate the effectiveness of the WAHTOR optimization we report in Figure 3.4 the values of the gradient norm with respect to $\boldsymbol{R}$ parameters and the correlation energy percentage as a function of the optimization steps (H_2-8qubits system with Jordan-Wigner mapping, depth 2 and the entangler map shown in Figure 3.2). As shown in the graph in figure 3.4, the gradient smoothly decreases to zero, whereas the correlation energy reaches the asymptotic value of about 98%. We remark here that the WAHTOR optimization is performed 'adiabatically' in the sense that the $\boldsymbol{R}$ and the circuit parameters are always taken from the previous run, without the necessity to explore a large number of different VQE runs at each WAHTOR optimization step. Since, as expected, the quality of the obtained results does depend on the entangler map, namely the arrangements of the CNOT gates in each entangler block of the ansatz, we have decided to compare systematically the performance of WAHTOR with those of VQE on a simple case. For this purpose, considering an H_2-8qubits system, we have chosen a set of 144

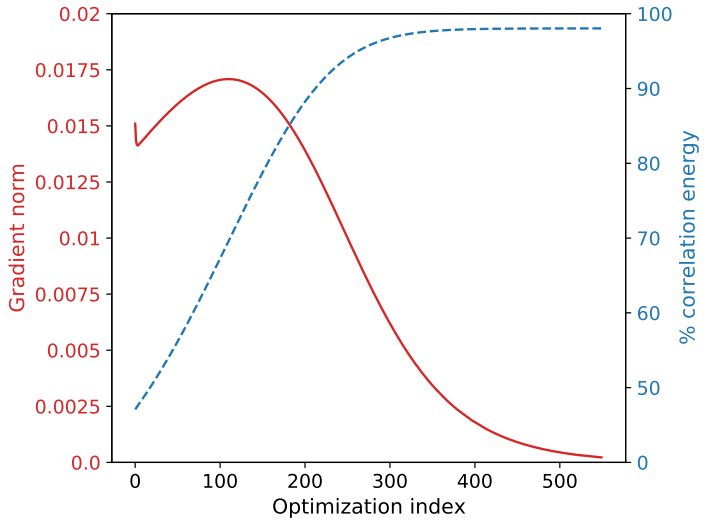

Figure 3.4: WAHTOR work for H_2 molecule. Energy optimization following the gradient on $\boldsymbol{R}$ parameters provided by the WAHTOR algorithm. Gradient norm (red line) and percentage of correlation energy (blue dashed line) are shown as a function of the optimization steps during adiabatic optimization. We used the H_2-8qubits system with Jordan-Wigner mapping, depth 2 and entangler map shown in Figure 3.2.

different hardware-efficient ansätze with depth 2. Details on the structure of the wavefunctions are shown in the computational details section. Figure 3.5(a) reports for each of the 144 entangler maps considered, the best VQE energy values (green crosses) and the final energy obtained by WAHTOR optimization (blue circles). The VQE energies are spread out in a range from 20% to 60% of correlation energy, with the exception of two entangler maps that reach approximately 79% and 98% of the correlation energy. The effect of using the WAHTOR algorithm lead to a significant improvement. The results are all clearly spanning a small set of three local minima that correspond approximately to 24%, 79% and 98% of the correlation energy. The majority of the optimizations (about 80%) reached the 79% of correlation energy whereas 12% the 98% and only the 8% remain at 24% of the correlation energy. We will investigate later in the text whether these minima correspond to the same physical state. One of the main problems troubling VQE is represented by the presence of a large number of local minima. This issue requires performing a significant amount of VQE evaluations when starting from circuit parameters randomly distributed [64, 65]. To investigate the effect of WAHTOR on this issue we consider 100 independent VQE opti-

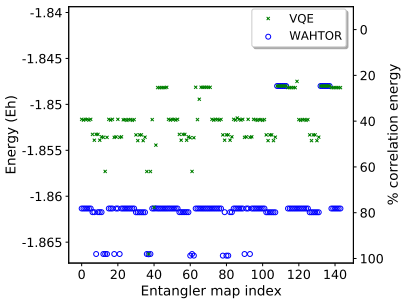

(a) simulations using different entangler maps

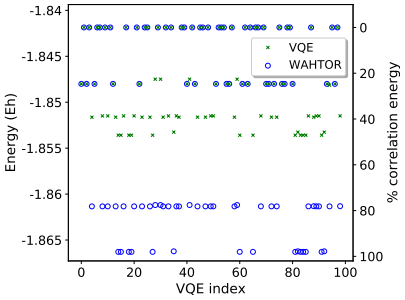

(b) indipendent simulations using the same entangler map

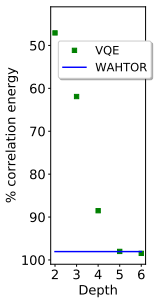

(c) increasing circuit depth

Figure 3.5: (a) Comparison between WAHTOR (blue circles) and VQE (green crosses) energies obtained using 144 ansätze with different entangler maps. We used the H_2-8qubits system with Jordan-Wigner mapping and circuit depth equal to 2. (b) Energies and Percentage correlation energies for different VQE initial ansatz parameters. The VQE (green crosses) and WAHTOR (blue circles) energies from different independent simulations of the $H2$-8qubits system: the encoding method used is the Jordan-Wigner and the ansatz is composed by 2 blocks with fixed entangler map, shown in figure 3.2. (c) Solid green squares represent VQE energies obtained with an increasing circuit depth. The system considered is the H_2-8qubits obtained with Jordan-Wigner mapping and the entangler map used in each ansatz is the same and equal to the one shown in figure 3.2. The blue line represents the WAHTOR energy obtained with the same system and a circuit ansatz with depth 2.

		VQE		WAHTOR	
entangler map	mapping	energy	%corr energy	energy	%corr energy
[[0, 1], [1, 2], [2, 3], [3, 4], [4, 5], [5, 6], [6, 7]]	JW	-1.84818	24.6	-1.86134	78.2
[[0, 1], [0, 2], [0, 3], [2, 4], [4, 5], [4, 6], [4, 7]]	JW	-1.85359	47.1	-1.86629	98.0
[[0, 1], [1, 2], [2, 3], [1, 4], [4, 5], [4, 6], [4, 7]]	JW	-1.85332	46.0	-1.86175	79.8
[[0, 1], [0, 2], [2, 3], [2, 4], [4, 5], [4, 6], [6, 7]]	JW	-1.85363	47.2	-1.86647	98.8
[[0, 1], [1, 2], [2, 3], [3, 4], [4, 5], [5, 6], [6, 7]]	P	-1.85426	49.8	-1.86646	98.7
[[0, 1], [0, 2], [0, 3], [2, 4], [4, 5], [4, 6], [4, 7]]	P	-1.84987	32.2	-1.86134	78.2
[[0, 1], [1, 2], [2, 3], [1, 4], [4, 5], [4, 6], [4, 7]]	P	-1.85406	49.0	-1.86646	98.7
[[0, 1], [0, 2], [2, 3], [2, 4], [4, 5], [4, 6], [6, 7]]	P	-1.85426	49.8	-1.86646	98.8
[[0, 1], [1, 2], [2, 3], [3, 4], [4, 5], [5, 6], [6, 7]]	BK	-1.86121	77.6	-1.86134	78.2
[[0, 1], [0, 2], [0, 3], [2, 4], [4, 5], [4, 6], [4, 7]]	BK	-1.86634	98.3	-1.86638	98.4
[[0, 1], [1, 2], [2, 3], [1, 4], [4, 5], [4, 6], [4, 7]]	BK	-1.86161	79.3	-1.86175	79.8
[[0, 1], [0, 2], [2, 3], [2, 4], [4, 5], [4, 6], [6, 7]]	BK	-1.86634	98.3	-1.86638	98.4

Table 3.1: VQE and WAHTOR results for H_2 molecule using different mapping and starting from different initial ansatz with depth 2.

mizations using the same fixed entangler map (green crosses of figure 3.5(b)) for an empirical ansatz with depth equal to 2 and 24 variational parameters. Starting from these points, WAHTOR energies (blue circles) show that if the starting VQE energies are sufficiently good (below 24% of correlation energy) the algorithm is able to jump the region of the VQE local minima (42.01% if correlation energy) often achieving 98.75% of the correlation energy. We note that to reach the same correlation energy value using VQE is necessary to increase the circuit depth at least by a factor 5 (using 48 variational parameters), as shown in Figure 3.5(c). We have also observed that although the unitary transformation depends in principle on 16 parameters, in practice, due to orbital symmetries, only one of such parameters is relevant for energy optimization. Therefore, in this example, the total number of variational parameters optimized in the WAHTOR procedure can be considered as 25, just one more than the VQE procedure. We have therefore demonstrated that we can obtain the same result using a much shorter circuit depth, with less than half CNOT gates, which is a crucial ingredient to avoid noise dominance in NISQ devices [81, 82]. Using the same method we tested the algorithm for different encoding methods. VQE and WAHTOR energies with different wavefunction ansatzes and mapping schemes have been reported in Table 3.1. The blue circles at 98% correlation energy in figures 3.5(a) and 3.5(b) are associated with WAHTOR optimized wavefunctions having all different $\boldsymbol{\theta}$ and $\boldsymbol{R}$ parameters. To investigate whether these points represent the same physical state we have rotated back for each case the final wavefunction on the original starting Hamiltonian and analysed the major components of such wavefunctions with respect to the exact solution (diagonalization). Figure 3.6 shows that the 98% points using different entangler maps (blue crosses

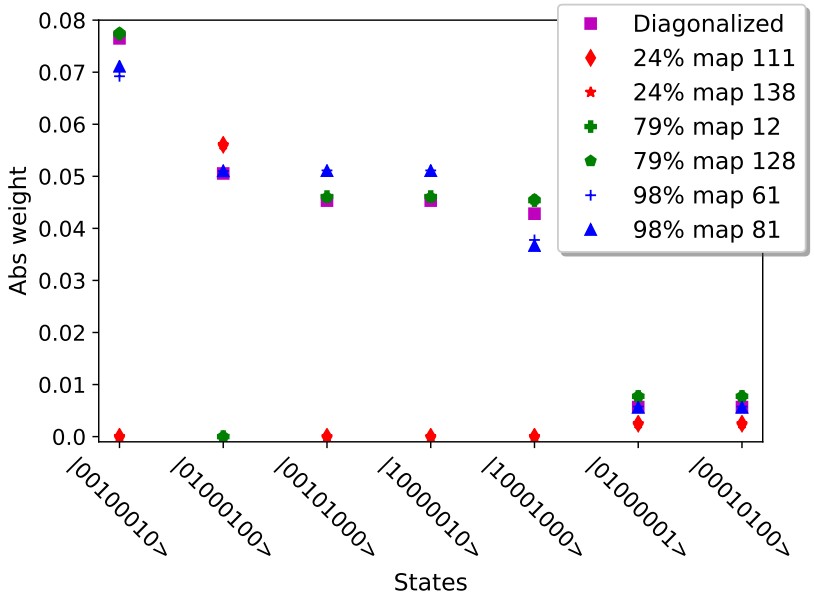

Figure 3.6: Image shows the seven states of the ground state to which the highest absolute values of the weights correspond (Hartree-Fock term is not included). Magenta points correspond to the exact ground state while red, green and blue points correspond to wavefunctions that characterize the local minima at, respectively, 24%, 79% and 98% of correlation energy. For each minimum two different wavefunctions (corresponding to the different entangler maps of Figure 3.5(a)) are shown and it follows that these correspond to the same physical state.

and triangles) do actually represents the same physical states since they possess all the most important excitations which are present in the exact result (magenta squares). Analogously, 24% and 79% data with different entangler maps also represent the same physical minima as shown by red and green points. In these latter cases, the wavefunctions are clearly missing some of the ingredients of the ground state; for instance, the 78% cases do not include the first double excitation. An important characteristic of a quantum chemistry calculation is the capability to describe chemically different situations (such as bonding, transition states or atomic limit). We investigate this flexibility property by measuring the percentage of the correlation energy along the H_2 dissociation curve using Jordan-Wigner mapping as reported in Figure 3.7. For each atomic distance, the best result obtained from 50 VQE simulation and the corresponding WAHTOR result are reported along the entire dissociation curve. Data shows that the new algorithm is able to

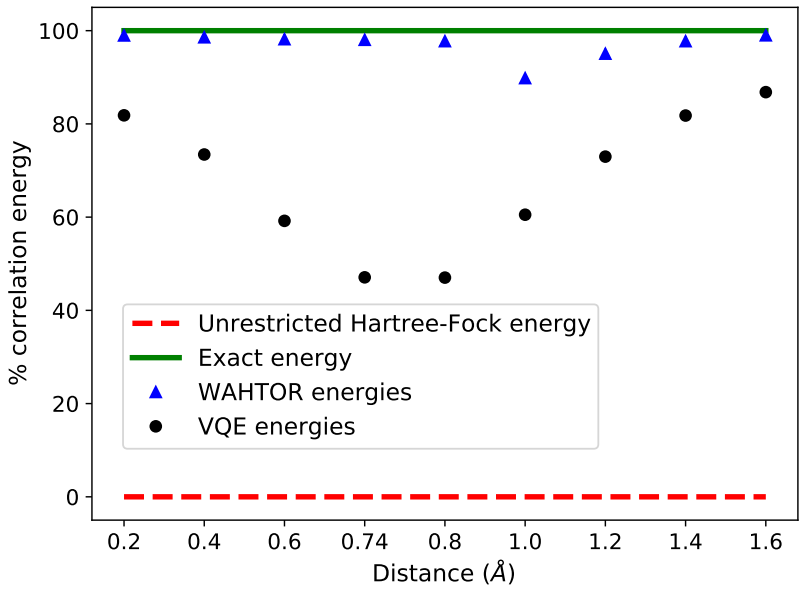

Figure 3.7: Performance of VQE and WAHTOR along the dissociation curve for H_2 molecule.

adapt to different chemical regimes, from bond formation to single atoms. To test the algorithm on a more complex system with a greater number of qubits, we consider the LiH molecule sto-3g basis set (system LiH-10qubits and LiH-12qubits with and without the two qubits reduction, respectively, as described in computational details section). The ansatz used consists of two blocks in which the entangler map is of ladder type. The typical trends for the energy and gradient norm for a LiH-12qubits are shown in Figure 3.8. In this case, despite the initial ansatz parameters not being optimized, the algorithm reached anyway the value of 93% of correlation energy. As in the case of the H_2 molecule, 50 simulations of the VQE algorithm and one WAHTOR simulation were carried out starting from the wave function parameters corresponding to the best energy result among out of 50 VQEs. Similarly to what was observed for the case of H_2-8qubits, WAHTOR is able to significantly improve the correlation energy of the minimal circuit depth of 2, reaching 93% of the correlation energy, whereas the VQE value only reaches 72%. Different lithium hydride systems have been considered in order to compare the WAHTOR and the VQE algorithm. Table 3.2 shows results obtained considering different encoding maps with the same ansatz structure. Note that the lowest energies reached by VQE and WAHTOR algorithms do not depend on the encoding method used. We also consider a system

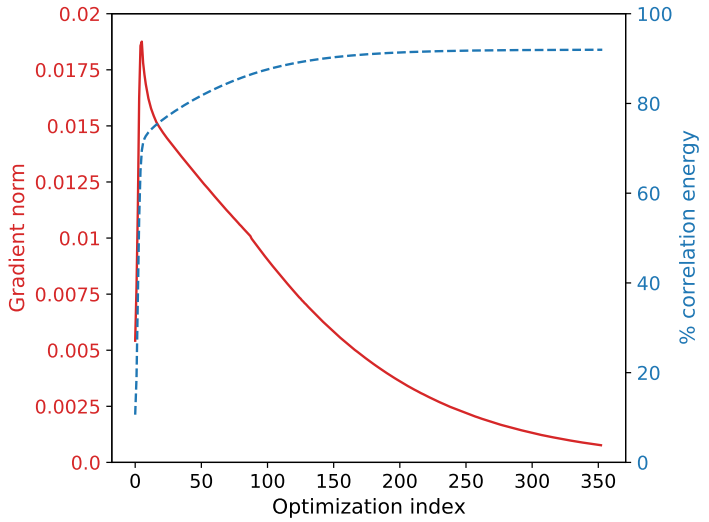

Figure 3.8: WAHTOR work for LiH molecule. The percentage of correlation energy (red line) and gradient norm (blue dashed line) for LiH-12qubits system, Jordan-Wigner mapping and simple ladder entangler map is reported as a function of the optimization steps.

with strong correlations, that is the dissociation of a square H_4 molecule. Figure 3.9 shows the VQE and WAHTOR correlation energy along the reaction coordinate that describes the H_4 to $4H$ dissociation process. Even in such extreme case of strong correlation, it is clear as WAHTOR is able to significantly improve the variational recovery of the correlation energy.

3.4.2 Noiseless measurement-based simulations

Since on quantum devices the evaluation of energy and gradients is carried out through measurement-based procedure, both quantities will be affected

		VQE		WAHTOR	
mapping	# qubits	energy	%corr energy	energy	%corr energy
JW	12	-8.87188	71.3	-8.87643	93.7
BK	12	-8.87185	71.2	-8.87643	93.7
P	12	-8.87202	72.0	-8.87643	93.7
P	10	-8.87202	72.0	-8.87643	93.7

Table 3.2: VQE and WAHTOR results for LiH molecule using different mapping.

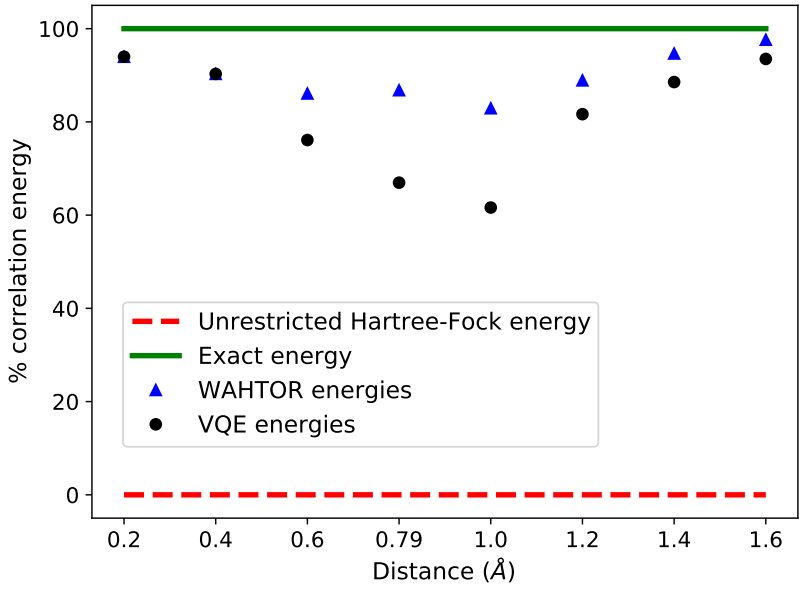

Figure 3.9: Performance of VQE and WAHTOR along the dissociation curve of a square H_4 molecule into 4 hydrogen atoms.

by statistical noise. In this section, we investigate the robustness of WAHTOR optimization against the noise on the energy gradient arising from measured-based simulations instead of state-vector simulations. The further optimization introduced by WAHTOR might in principle introduce additional instabilities along the optimization process with respect to traditional VQE. We investigated this issue considering the H_2-8qubits system with the same ansatz used in the previous section (depth 2 and the following entangler map: $[[0,1],[0,2],[0,3],[2,4],[4,5],[4,6],[4,7]]$). For the VQE optimizations of the WAHTOR algorithm we used state vector simulations while the energy derivatives are evaluated with the noiseless measurements. As optimization method for the VQE we have chosen the COBYLA [77] algorithms. Figures 3.10(a) and 3.10(b) show the correlation energy and gradient norm of the energy with respect to the $\boldsymbol{R}$ parameters as a function of the optimization steps. The data show that the measured-based simulations in the derivatives converge very close to the state vector simulations. In the case of H_2-8qubits system this happens already for 2048 shots. Obviously, as the number of shots increases, the convergence is achieved with a smaller number of optimization steps and the resulting curve looks smoother. The results for the larger system LiH-12qubits (shown in panels (c) and (d) of Figure 3.10) clearly require a larger amount of shots. In summary, the WAHTOR opti-

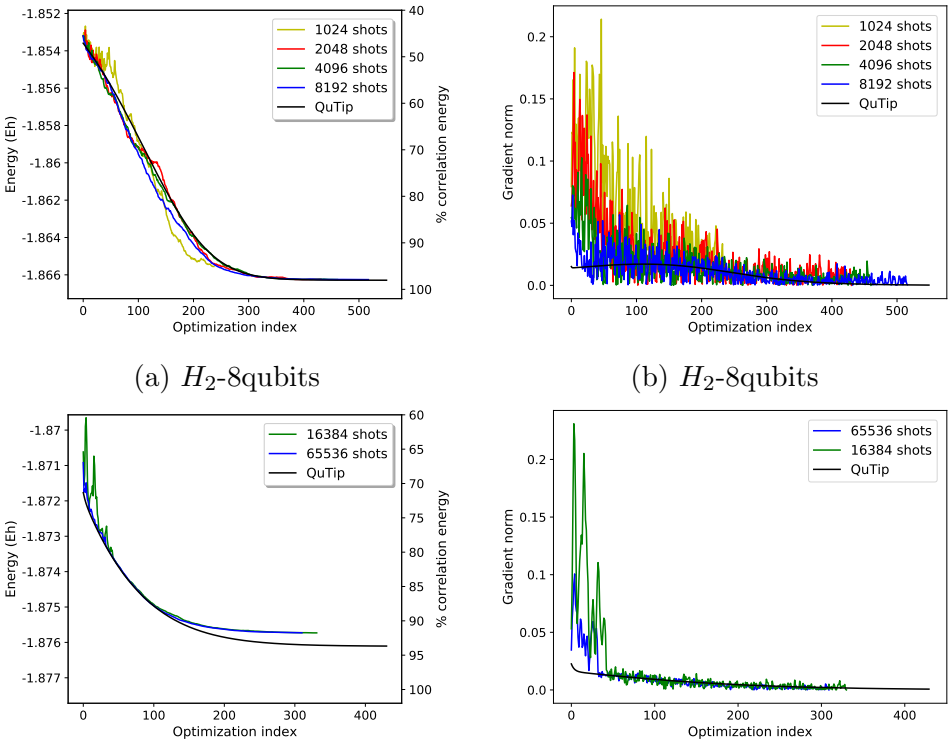

(a) H_2-8qubits (b) H_2-8qubits

(c) LiH-12qubits (d) LiH-12qubits

Figure 3.10: Effect of noiseless measurement-based evaluation of gradients in WAHTOR method. Panel (a) and (b): H_2-8qubits system. Panel (c) and (d): LiH-12qubits system. Energies (left panels) and gradient norms with respect to the $\boldsymbol{R}$ parameters (right panels), are reported for both systems using a different number of shots.

mization is possible also in presence of statistical noise with a limited amount of shots.

3.4.3 Noisy measurement-based simulations

The effect of noise has to be investigated to verify the performance of the proposed algorithm on real NISQ devices. The possibility to adapt the Hamiltonian to a given wavefunction ansatz using the energy gradient with respect to the $\boldsymbol{R}$ parameters will be valid only if this gradient is not covered by noise. We have therefore simulated our algorithm using a noise model which is built starting from parameters of the *ibmq_boeblingen* quantum hardware [81]. Starting from the noise model of this device, we considered a simplified noise model consisting of the average values of the error probabilities of

the single qubit gates, the CNOT gates, and the readout errors. We also considered models with reduced overall noise by multiplying all parameters by different factors, with the aim to find the minimum tolerated errors for the WAHTOR algorithm able to estimate energies that can be compared to those obtained by state vector simulations. The system considered is the H_2-8qubits molecule with the same ansatz chosen as the one used in previous simulations. Starting from the optimized parameters by the noiseless measured-based WAHTOR simulations, we performed noisy measurements of the energy of the H_2 molecule using the noise models described before. Figure 3.11 shows the energy results for each noise model (same model with different average values of errors): for each system, 20 energy measurements have been performed with 100 000 shots and the values reported correspond to their average value with the corresponding standard deviation. Data show that, without using error-mitigation techniques, the WAHTOR algorithm can be applied on devices with a CNOT gate error smaller than 0.001% and with a readout error smaller than 0.004%.

	readout error	single qubit gate error (1 pulse)	CNOT gate error
Reference Values	4,70%	0,038%	1,30%
A	0,047%	0,038%	0,13%
B	0,047%	0,00038%	0,13%
C	0,047%	0,00038%	0,013%
D	0,047%	0,00038%	0,0013%
E	0,0047%	0,000038%	0,013%
F	0,0047%	0,00038%	0,0013%
G	0,0047%	0,000038%	0,0013%

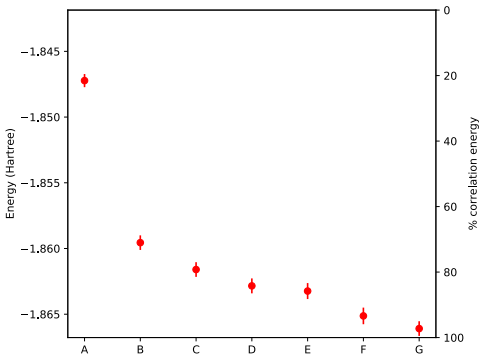

Figure 3.11: WAHTOR energy obtained from the average of 20 measurements made with 100 000 shots. Each point represents the average energy related to the noise model whose values are reported in the table on the left.

3.5 Conclusions

In this section, we have proposed a VQE strategy to adapt the Molecular Hamiltonians used in Quantum Chemistry to a given wavefunction ansatz by using a unitary transformation of the molecular orbitals. This strategy can be viewed as a reversal of perspective: instead of optimizing the circuit topology, we optimize the molecular Hamiltonian (or in general a cost function) to 'adapt' it to a given circuit ansatz. Through the explicit evaluations of energy gradients with respect to the parameters of the unitary transformation of the Hamiltonian we have demonstrated in prototypical cases that the amount of correlation energy can be significantly improved without modifying the topology of the ansatz. This flexibility allows adapting the Hamiltonian to the construction of circuits that reflect the connectivity of the hardware. For instance, using ansätze that can only provide about 45% correlation energy in VQE such procedure can gain up to the 98% (as illustrated in Figure 3.5(b)). The proposed optimization of the unitary transformation is robust against noise and it is especially convenient when applied in NISQ devices, in which the circuit depth is the main limitation to the application of quantum computing algorithms to real cases because of noise and decoherence. A second positive advantage of having a shallow circuit is the smaller propensity of being trapped into local minima since it has been demonstrated that depth is correlated to the presence of barren plateaux [66]. Since the downsizing of the Hilbert space is a crucial ingredient to reduce the number of logical qubits, an extension of the proposed methodology that might be worthwhile to investigate is the use of active space selections [83, 84]. Even without the use of such techniques, it seems anyway that the orbitals rotations in the WAHTOR algorithm allow a partial compensation of the effect of the reduction of the active space, similar to what was observed in ref.[68]. The optimization process applied here to the case of finding the ground state of the Molecular Hamiltonian can be in principle extended to other cost functions useful in Chemistry or in other fields that are invariant under some particular unitary transformations and might be therefore extended to other VQE optimizations.

Chapter 4

Optimization strategies in WAHTOR algorithm

By exploiting the invariance of the molecular Hamiltonian by a unitary transformation of the orbitals it is possible to significantly shorter the depth of the variational circuit in the VQE algorithm by using the WAHTOR algorithm. This work introduces a non-adiabatic version of the WAHTOR algorithm and compares its efficiency with three implementations by estimating Quantum Processing Unit (QPU) resources in prototypical benchmarking systems. Calculating first and second-order derivatives of the Hamiltonian at fixed VQE parameters does not introduce a significant QPU overload, leading to results on small molecules that indicate the non-adiabatic Newton-Raphson method as the more convenient choice. On the contrary, we find out that in the case of Hubbard model systems the trust region non-adiabatic optimization is more efficient. The preset work therefore clearly indicates the best optimization strategies for empirical variational ansatzes, facilitating the optimization of larger variational wavefunctions for quantum computing.

4.1 Introduction

Quantum computers and algorithms have brought about significant advancements in computational capabilities, potentially revolutionising numerous scientific fields. [85, 86, 87, 88, 89] Leveraging the principles of quantum mechanics, these technologies enable the manipulation and processing of information in ways that are fundamentally different from classical computers. [22, 90] Among the many applications of quantum algorithms, quantum simulations [91, 92] stand out as a field that stands to benefit significantly from these advancements, particularly in quantum chemistry. [56, 50, 5, 93] One

of the leading quantum algorithms for addressing quantum chemistry problems is the Variational Quantum Eigensolver (VQE). [35, 36, 44, 94, 95] VQE combines classical and quantum resources to find the ground state energy of a molecular system. By employing a parameterized quantum ansatz representing a trial wave function, VQE iteratively adjusts the parameters to minimize the energy through measurements performed on a quantum computer. This hybrid approach allows for exploring the complex quantum landscape associated with molecular systems. Despite its promise, VQE faces challenges in scaling to larger systems due to the exponential growth of the parameter space and, more generally, due to the implementation of the longer circuits describing wavefunctions on noisy devices. To overcome these obstacles, many algorithms have been developed to improve the performance of the VQE. [65, 69, 96, 97, 98] Moreover using heuristic ansätze [67, 82], rather than the chemically inspired ones [99, 38, 62], allows us to consider more shallow circuits. Another solution being explored is the development of pulse-based ansätze, which aims to optimize and shorten circuit lengths. [100, 101, 102] One of the methods that have emerged as a potential solution is the Wave Function Adapted Hamiltonian Through Orbital Rotations (WAHTOR). [103] This algorithm optimizes molecular orbitals by adapting the Hamiltonian to the chosen topology of the wave function ansatz, utilizing orbital rotations to facilitate more efficient and accurate simulations within the VQE framework. Essentially, the algorithm works as follows: once defined the initial Hamiltonian H in the Hartree-Fock basis, we perform a first VQE algorithm. Then we apply to the initial Hamiltonian a parameterized unitary operator $\hat{U}_1 = \hat{U}_1(\boldsymbol{R_1})$, corresponding to a change of the single-particle basis set. The vector of the rotation parameters $\boldsymbol{R_1}$ is chosen in order to find the operator $\hat{U}_1$ that reduces the expectation value of the energy. The transformed Hamiltonian $\hat{U_1}^{\dagger}(\boldsymbol{R_1})H\hat{U}_1(\boldsymbol{R_1})$ is used to perform a VQE optimization for the re-optimisation of the wave function. Once the ansatz optimisation is converged we determine, keeping the ansatz parameters fixed, a new operator $\hat{U}_2 = \hat{U}_2(\boldsymbol{R_2})$, corresponding to an additional rotation that is applied to the Hamiltonian used in the previous VQE, so the resulting unitary transformation is obtained by applying the operator $\hat{U}_1(\boldsymbol{R_1})\hat{U}_2(\boldsymbol{R_2})$ to the initial Hamiltonian to perform another VQE. We alternate a VQE run and the definition of a new Hamiltonian until energy convergence is reached. Thus the final Hamiltonian can be calculated by applying the operator given by the product of the single unitary operators $\hat{U} = \hat{U}_1(\boldsymbol{R_1})\hat{U}_2(\boldsymbol{R_2})\hat{U}_3(\boldsymbol{R_3})\ldots$ to the initial Hamiltonian, i.e. the one expressed in the Hartree-Fock basis. Orbital optimization in the context of the VQE quantum algorithm is a method also adopted in the ref. [68]: in this work, the optimization exploits

derivatives up to the second order and the optimizer moves along the direction of the Newton method. On the other end, the WAHTOR method is a useful approach that offers flexibility in choosing optimizers capable of leveraging the analytic derivatives of any order, as shown in the present work. Optimizers play a crucial role in the process, aiming to identify the optimal set of parameters that minimize the energy of a given system. [104, 105] Different optimizers employ a variety of strategies and algorithms that efficiently explore the energy landscape, resulting in faster convergence and improved accuracy. In this study, we compare the original algorithm, called adiabatic, with a new procedure, called non-adiabatic that we will illustrate in section 4.3. The main focus is to explore the potential of the non-adiabatic versions of the WAHTOR algorithm. Through the analysis of these optimizers, our objective is to examine their convergence behaviour, computational efficiency and accuracy. This evaluation aims to enhance our understanding of their functioning and contributions to the optimization of molecular orbitals in quantum chemistry simulations. It is important to note that the WAHTOR method extends beyond molecular systems, finding relevance in other quantum systems such as the Hubbard model. [106, 107, 108, 109] By exploring the performance of these optimizers on different systems, we can gain insight into their versatility and potential applications of the algorithm to different quantum systems. In section 4.2 we provide the computational specifics of the algorithm, including the systems studied, the ansatz used, and a description of the optimization strategies employed. In section 4.3, we present the mathematical treatment of the non-adiabatic algorithm and we analyze the performance of the optimization methods for each system considered. Specifically, we examine the optimization steps in relation to the number of measured strings, which reflects the utilization of QPU resources during the optimization. Lastly, in section 4.4, we discuss the results obtained.

4.2 Computational details

Implementation of derivatives
we do not consider mixing all orbitals with the same spin but we simply linearly combine orbitals with the same spin that possesses the same geometric symmetries. One can see the optimization of orbitals as a mixing of the starting orbitals weighted by the rotation vector $\boldsymbol{R}$. For the implementation of the WAHTOR algorithm, the matrices responsible for the basis change consider spin symmetry. This means that the spin-up and the spin-down single-particle states are not linearly combined and they are transformed using the same generic unitary transformation, represented by the matrix U.

This results in a set of $\frac{n^2+n}{2}$ symmetric and $\frac{n^2-n}{2}$ antisymmetric matrices as generators for a system with n single-particle states for each spin projection. In the case of molecules, by linearly combining only spin-orbitals with the same spatial symmetry, we can reduce the number of variables (or parameters) in the Hamiltonian lowering the computational cost.

Simulated systems

We tested the optimization methods of the WAHTOR algorithm on two molecular systems and on the Hubbard model, which represent an example of a strongly correlated system. For the molecule, the Hamiltonian has been calculated using the PySCF Python package.[72] The systems studied, along with their descriptions, are as follows:

- Hydrogen fluoride (HF): atoms were set at the bond distance of 0.917Å using the 'sto-3g' basis set. The system, obtained through the Jordan-Wigner encoding method and the frozen core approximation, comprises 10 qubits. For simulations, a heuristic ansatz with 2 blocks was employed. Each block includes a layer of rotations around the y-axis on each qubit, as well as a simple ladder map of entanglers (CNOT gates) in which each qubit is the target of the previous qubit and the control of the following qubit.

- Water molecule (H_2O): the atoms are arranged to form an isosceles triangle with oxygen positioned at the vertex, the distance between the oxygen and the hydrogen is equal to 0.957Å while the angle at the vertex, between the two equal sides of the triangle, is equal to $104,5°$. The 'sto-3g' basis set was utilized. The resulting system, obtained using the Jordan-Wigner mapping [110] and the frozen core approximation, consists of 12 qubits. The blocks of the ansatz are the same used for the HF molecule but with a depth of 4 instead of 2.

- 4-site ring Hubbard model in the half-filling regime: the Hamiltonian of the system is:

$$H = \sum_{<i,j>} \sum_{\sigma=\uparrow,\downarrow} -\left(a^\dagger_{i\sigma} a_{j\sigma} + a^\dagger_{j\sigma} a_{i\sigma}\right) + V \sum_{i=1}^{4} n_{i\uparrow} n_{i\downarrow} + \mu \sum_{i}^{4} (n_i - 2)^2 \quad (4.1)$$

  where $n_{i\sigma} = a^\dagger_{i\sigma} a_{i\sigma}$ with $\sigma = \{\uparrow, \downarrow\}$, V is the on-site potential, $n_i = n_{i\uparrow} + n_{i\downarrow}$, μ is the chemical potential preserving the requested number of particle for each spin and $< i, j >$ denote the nearest-neighbour. We use the value $V = 8$ and $\mu = 8$, which is a strongly correlated regime. We applied the Jordan-Wigner mapping obtaining an 8-qubit system and the heuristic ansatz considered is composed of 7 blocks:

each odd block consists of a pattern of entanglers given by the map $[0,1],[1,2],[2,3],[4,5],[5,6],[6,7]$ and each even block by the topology $[0,4],[1,5],[2,6],[3,7]$. The first two blocks of the ansatz are shown in figure 4.1.

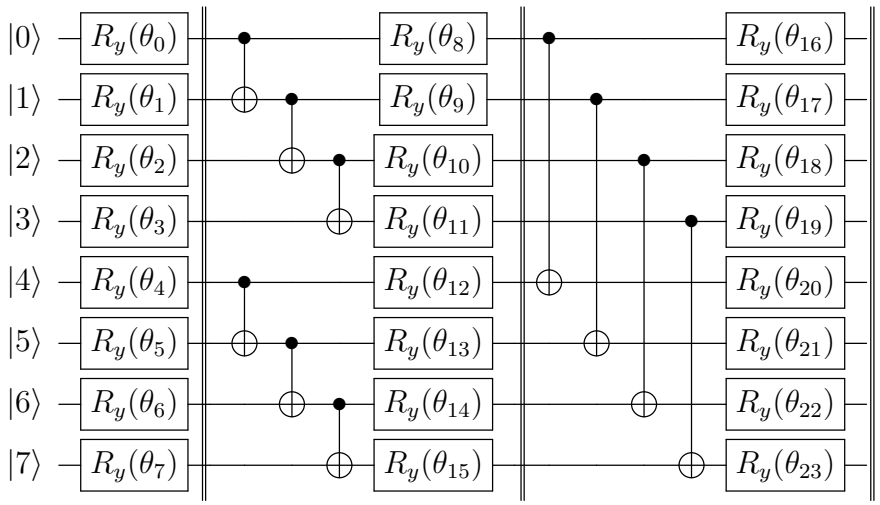

Figure 4.1: Entangler map for the Hubbard system.

Ansatz optimization

The ansatz parameters are represented with the vector $\boldsymbol{\theta}$, initialized randomly in the range $[0, 2\pi)$. For all the simulated systems, the VQE algorithm optimizes these parameters using the BFGS optimizer in the state vector mode and the convergence threshold is set to $10^{-6}Eh$. The Qiskit library [73] has been used to prepare the quantum circuit, map the fermionic system into qubits and evaluate the cost function.

Hamiltonian optimization strategies

Two optimization strategies have been considered for the WAHTOR algorithm: the first is the adiabatic optimization, as described in ref. [103] and the second is the non-adiabatic optimization, illustrated in the next section. The distinction between adiabatic and non-adiabatic methods lies in the variational quantum state that is taken into account during any calculation of the energy derivatives with respect to the Hamiltonian parameters. In the first case, according to the Hellmann-Feynman theorem, the parametrized quantum state is the one that minimizes the energy functional with respect to that value of the Hamiltonian parameters. [103] For the non-adiabatic method, the energy is simply a function of the Hamiltonian parameters so that the

resulting quantum state, in general, is not at its variational minimum or, if it is, the energy derivatives of order greater than one can be calculated as the expectation value of the Hamiltonian derivatives operator. Derivatives calculation requires classical and quantum resources, for this reason we implemented three different optimization strategies of the Hamiltonian for the non-adiabatic algorithm:

- non-adiabatic trust region: the cost function is approximated with a quadratic model into a region around the current point. The radius of this trust region is determined at each step and the optimum value of the cost function is determined inside this region. [104] In each step of the Hamiltonian optimization routine, the first and second derivatives of the cost function are determined using the equations described in the next section. The new Hamiltonian is found and another step of this routine start. The cycle continues until convergence is reached.

- non-adiabatic Newton-Raphson: in the Hamiltonian optimization routine, the $\hat{U}(\boldsymbol{R})$ operator is determined by taking

$$\boldsymbol{R} = -(\nabla^2 E(\boldsymbol{R}, \boldsymbol{\theta})|_{\boldsymbol{R}=\boldsymbol{0}})^{-1} \nabla E(\boldsymbol{R}, \boldsymbol{\theta})|_{\boldsymbol{R}=\boldsymbol{0}} \tag{4.2}$$

  following the idea of the Newton-Raphson optimizer [111]. The operator $\hat{U}(\boldsymbol{R})$ give us the new Hamiltonian.

- non-adiabatic BFGS: this method exploits the BFGS (Broyden-Fletcher-Goldfarb-Shanno) optimization algorithm to update the cost function. [112, 113, 114, 115] A quadratic model of the objective function is built but, in this case, the Hessian matrix is approximated using the incremental ratio of the gradient. In our implementation, this method does not use derivatives of the cost function so even the gradient is approximated. In this case, the derivatives are not calculated but their estimation is repeated until convergence is reached.

The three strategies illustrated above and the adiabatic strategy have been compared to evaluate the convergence behaviour and assess their advantages and limitations in terms of Quantum Processing Unit (QPU) resources. We remark that the QPU resources are not directly linked to the number of optimization steps for the Hamiltonian since also the number of optimization steps for the $\boldsymbol{\theta}$ parameters of the wavefunction depends on whether the optimization has been carried out adiabatically or non-adiabatically. We, therefore, assume as a good estimation of the QPU resource directly the number of Pauli strings evaluations performed on quantum computing units.

4.3 Results

4.3.1 Non-adiabatic WAHTOR algorithm

In this subsection, we illustrate in detail the non-adiabatic WAHTOR algorithm. Note that the notation is different from the one used in the previous chapter. The idea behind this method is to transform the Hamiltonian with the aim to adapt it to a given empirical ansatz. To this aim, we can exploit the property that the eigenvalues of the Hamiltonian H

$$H = \sum_{i,j} h_{ij} a_i^\dagger a_j + \frac{1}{2} \sum_{c,d,e,f} g_{cdef} a_c^\dagger a_d^\dagger a_e a_f \tag{4.3}$$

and the eigenvalues of $\hat{U}^\dagger H \hat{U}$ are the same if $\hat{U}$ is a unitary operator. Here we introduced a set of N single-particle states with the corresponding creation and the annihilation operators, respectively $a_i^\dagger$ and a_i for $i = 1, \ldots, N$. For the unitary operator, we choose the following parametrized form:

$$\hat{U} = \hat{U}(\boldsymbol{R}) = e^{\sum_{jk} (i\boldsymbol{R}\cdot\boldsymbol{T})_{jk} a_j^\dagger a_k} \tag{4.4}$$

where $\boldsymbol{T}$ and $\boldsymbol{R}$ are two vectors, the components of the former are the generators of the unitary matrix's Lie group with dimension NxN, whereas the latter is a vector of real components that are the variational parameters corresponding to the specific transformation applied to the Hamiltonian. The new operators $b_i^\dagger = \hat{U} a_i^\dagger \hat{U}^\dagger$ and $b_i = (b_i^\dagger)^\dagger$ satisfy the fermionic anticommutation relations

$$\{b_i^\dagger, b_j^\dagger\} = 0 \qquad \{b_i, b_j^\dagger\} = \delta_{ij} \qquad i, j = 1, \ldots, N \tag{4.5}$$

It follows that we can interpret these operators as the ones associated with a different set of N single-particle states that can be used to describe our quantum system. So, by exploiting the relation

$$b_k^\dagger = \sum_{j=1}^{n} U(\boldsymbol{R})_{jk} a_j^\dagger \qquad U(\boldsymbol{R}) = e^{i\boldsymbol{R}\cdot\boldsymbol{T}} \tag{4.6}$$

the transformed Hamiltonian $\hat{U}^\dagger H \hat{U}$ can be expressed in the initial single-particle basis set as

$$H(\boldsymbol{R}) \equiv \hat{U}^\dagger(\boldsymbol{R}) H \hat{U}(\boldsymbol{R}) = \sum_{i,j} h(\boldsymbol{R})_{ij} a_i^\dagger a_j + \frac{1}{2} \sum_{c,d,e,f} g(\boldsymbol{R})_{cdef} a_c^\dagger a_d^\dagger a_e a_f \tag{4.7}$$

where $h(\boldsymbol{R})$ and $g(\boldsymbol{R})$ are the transformed tensors of respectively h and g

$$h(\boldsymbol{R}) = e^{-i\boldsymbol{R}\cdot\boldsymbol{T}} h e^{i\boldsymbol{R}\cdot\boldsymbol{T}} \tag{4.8}$$

$$g(\boldsymbol{R}) = e^{-i\boldsymbol{R}\cdot\boldsymbol{T}} \otimes e^{-i\boldsymbol{R}\cdot\boldsymbol{T}} g e^{i\boldsymbol{R}\cdot\boldsymbol{T}} \otimes e^{i\boldsymbol{R}\cdot\boldsymbol{T}} \tag{4.9}$$

Now, we represent with $|A_i\rangle$ and $|B_i\rangle$, for $i = 1, \ldots, 2^N$, the Slater determinants obtained by applying on the vacuum state $|\varnothing\rangle$ the operators belonging respectively to the sets $\{a^\dagger\}$ and $\{b^\dagger\}$. It follows that for every parametrized state $|\Psi(\boldsymbol{\theta})\rangle = \sum_{i=1}^{2^N} c_i(\boldsymbol{\theta}) |A_i\rangle$, the application of the operator $\hat{U}$ give the new ket

$$|\Phi(\boldsymbol{\theta})\rangle = \hat{U} |\Psi(\boldsymbol{\theta})\rangle = \sum_{i=1}^{2^N} c_i(\boldsymbol{\theta}) |B_i\rangle \qquad c_i(\boldsymbol{\theta}) \in \mathbb{C} \qquad i = 1, \ldots, 2^N \tag{4.10}$$

Since the coefficients of the linear combination do not change, $|\Psi(\boldsymbol{\theta})\rangle$ or $|\Phi(\boldsymbol{\theta})\rangle$ can be represented by a quantum circuit with the same value of the $\boldsymbol{\theta}$ parameters by mapping on the qubits the single-particle states corresponding respectively to the set $\{a^\dagger\}$ or $\{b^\dagger\}$. The energy cost function

$$E(\boldsymbol{R}, \boldsymbol{\theta}) = \langle \Psi(\boldsymbol{\theta})| H(\boldsymbol{R}) |\Psi(\boldsymbol{\theta})\rangle \tag{4.11}$$

depends on both set of parameters $\boldsymbol{\theta}$ and $\boldsymbol{R}$. Energy can be optimized with respect to $\boldsymbol{R}$ parameters by calculating its n-order analytical derivatives:

$$\begin{aligned} \frac{d^n E(\boldsymbol{R}, \boldsymbol{\theta})}{d\boldsymbol{R}^n} &= \sum_{i,j} \frac{d^n h(\boldsymbol{R})_{ij}}{d\boldsymbol{R}^n} \langle \Psi(\boldsymbol{\theta})| a_i^\dagger a_j |\Psi(\boldsymbol{\theta})\rangle \\ &+ \frac{1}{2} \sum_{c,d,e,f} \frac{d^n g(\boldsymbol{R})_{cdef}}{d\boldsymbol{R}^n} \langle \Psi(\boldsymbol{\theta})| a_c^\dagger a_d^\dagger a_e a_f |\Psi(\boldsymbol{\theta})\rangle \end{aligned} \tag{4.12}$$

from which one can see the dependence on the n-order derivatives of $h(\boldsymbol{R})$ and $g(\boldsymbol{R})$. In particular, we can write down the first and second-order derivatives in $\boldsymbol{R} = \boldsymbol{0}$, that will be used along the optimization:

$$\begin{aligned} \frac{dh(\boldsymbol{R})}{dR_{l_1}}|_{\boldsymbol{R}=\boldsymbol{0}} &= i[T_{l_1}, h] \\ \frac{dg(\boldsymbol{R})}{dR_{l_1}}|_{\boldsymbol{R}=\boldsymbol{0}} &= i[T_{l_1} \otimes I + I \otimes T_{l_1}, g] \end{aligned} \tag{4.13}$$

and

$$\begin{aligned} \frac{d^2 h(\boldsymbol{R})}{dR_{l_1} dR_{l_2}}|_{\boldsymbol{R}=\boldsymbol{0}} &= -\frac{1}{2}([T_{l_1}, [T_{l_2}, h]] + [T_{l_2}, [T_{l_1}, h]]) \\ \frac{d^2 g(\boldsymbol{R})}{dR_{l_1} dR_{l_2}}|_{\boldsymbol{R}=\boldsymbol{0}} &= -\frac{1}{2}([T_{l_1} \otimes I + I \otimes T_{l_1}, [T_{l_2} \otimes I + I \otimes T_{l_2}, g]] + \\ &+ [T_{l_2} \otimes I + I \otimes T_{l_2}, [T_{l_1} \otimes I + I \otimes T_{l_1}, g]]) \end{aligned} \tag{4.14}$$

where I is the identity operator while l_1 and l_2 specify the components of the vector $\boldsymbol{R}$ along which we derive. The proofs of these equations can be found in

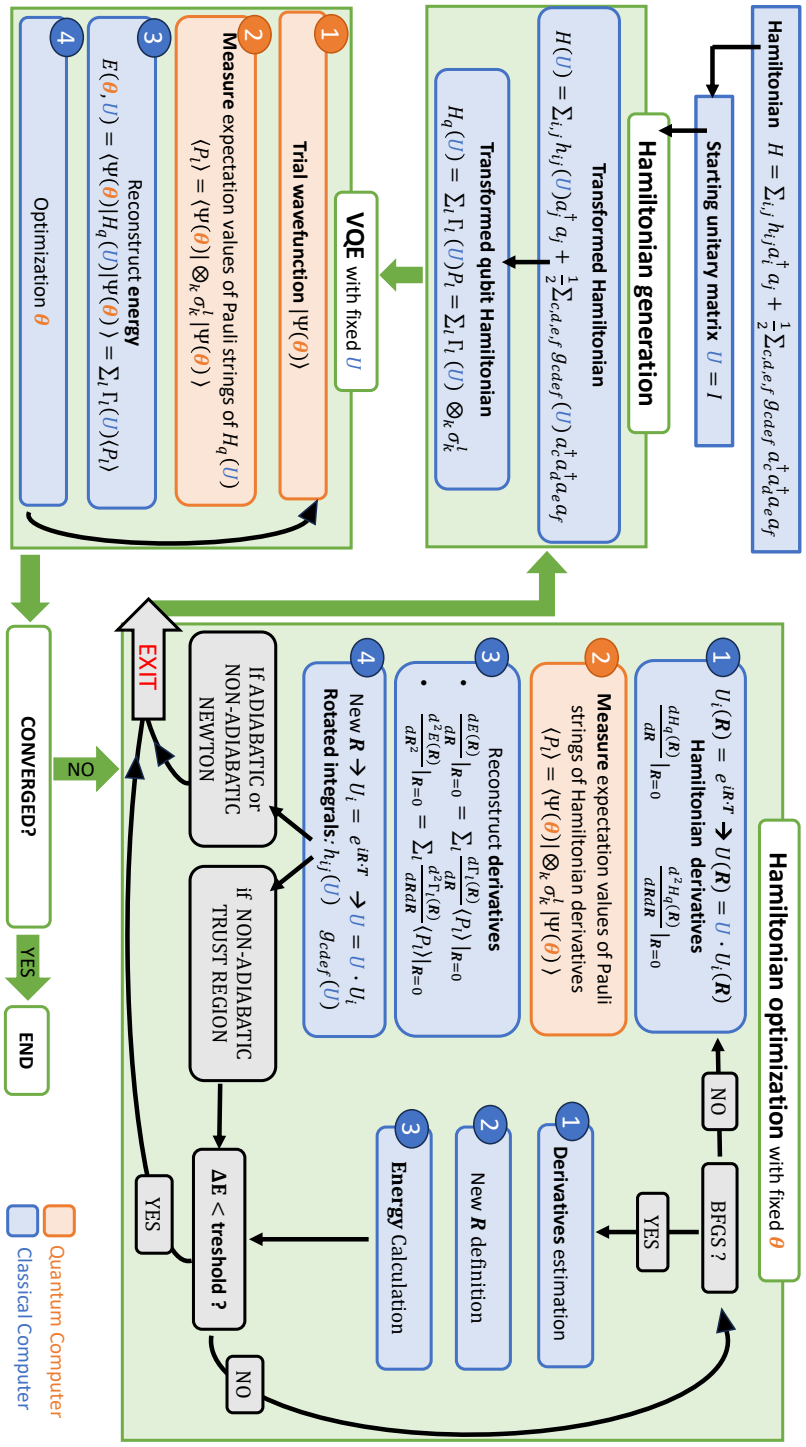

Figure 4.2: The scheme of the WAHTOR algorithm for both the optimization strategies, adiabatic and non-adiabatic defined in this article.

the chapter 10. The non-adiabatic WAHTOR is based on the optimization of wave function, i.e. the execution of a VQE, and of the Hamiltonian. More specifically once it has been defined the initial Hamiltonian H, a VQE optimization of the ansatz parameters $\boldsymbol{\theta}$ is performed. Then the minimum of $E(\boldsymbol{R}, \boldsymbol{\theta})$ with respect to $\boldsymbol{R}$ is found by exploiting one of the methods illustrated in section 4.2, resulting in a $\hat{U}_1$ operator that is used to define the new Hamiltonian $\hat{U}_1^\dagger H \hat{U}_1$ that is taken into account to perform a new VQE. The procedure is repeated until the energy difference between two consecutive VQEs is below the chosen threshold. At each step i in which an operator $\hat{U}_i$ is generated, the Hamiltonian is updated and the converged one is $\hat{U}^\dagger H \hat{U}$, where $\hat{U} = \hat{U}_1 \hat{U}_2 \hat{U}_3 \dots$. The converged quantum state $|\psi(\boldsymbol{\theta}_{opt})\rangle$ minimizes the expectation value of $\hat{U}^\dagger H \hat{U}$. At the same time, $\hat{U} |\psi(\boldsymbol{\theta}_{opt})\rangle$ can be seen as the state that minimizes H and, as shown above, this one can be represented by the same quantum circuit of $|\psi(\boldsymbol{\theta}_{opt})\rangle$ if the qubits map the fermionic modes $\{b^\dagger\}$ instead of $\{a^\dagger\}$. In figure 4.2 the non-adiabatic and adiabatic strategies for the WAHTOR algorithm are reported. We stress the fact that, for the adiabatic version in each Hamiltonian optimization step, we define an energy functional and exploit the Hellmann-Feynman theorem to calculate analytically the first derivatives. For the non-adiabatic method, since we are considering an energy function, we can calculate the derivatives of each order in each Hamiltonian optimization step. Obviously, the first derivatives are determined in the same manner for both strategies. From a computational point of view, the VQE algorithm involves evaluating the Pauli strings that make up the Hamiltonian at each step. On the other hand, when computing derivatives for Hamiltonian optimization, the wave function has fixed parameters, resulting in consistent Pauli strings for the derivative operators. As a result, the Pauli strings of the derivatives are computed only during the first time that they appear during the optimization and are not recalculated thereafter. It is worth noting that a significant portion of the Pauli strings composing the derivatives are identical to those of the Hamiltonian. Instead of recomputing them, we utilize the Pauli strings evaluated during the last optimization step of the VQE algorithm.

4.3.2 Quantum chemistry and Hubbard model results

In this subsection, we report the results obtained by applying the optimization strategies illustrated above to the considered benchmarking systems, ranging from 8 to 12 qubits. Figure 4.3 shows the energy as a function of the evaluated Pauli strings for the HF molecule. All the optimizers start from the same VQE state corresponding approximately to the energy of -27.978 Hartree. Then a new Hamiltonian is generated through the calculation or

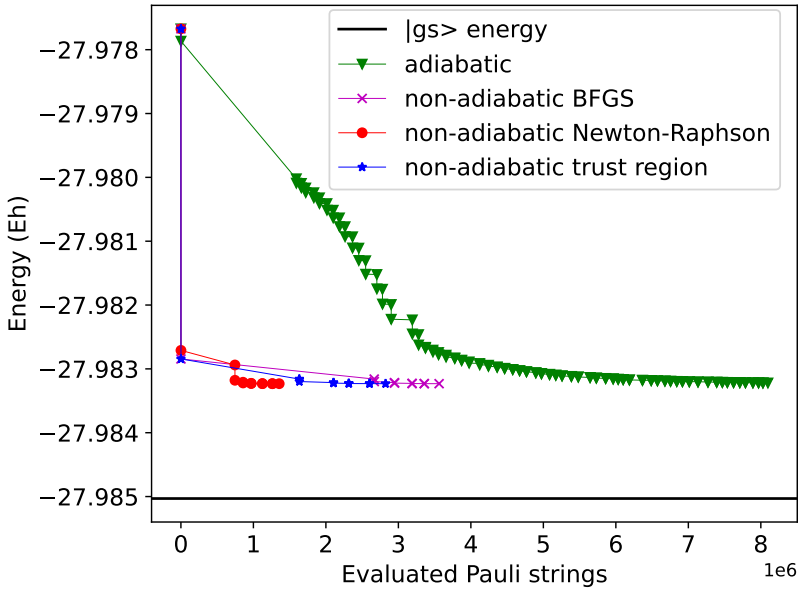

Figure 4.3: Performance of the different optimization strategies for the HF molecule. The obtained energies are reported as a function of the number of evaluated Pauli strings.

the estimation of the required derivatives, giving rise to a new point on each curve. Then a new step of optimization for the ansatz parameters is performed followed by a new generation of the Hamiltonian, as described in the scheme in figure 4.2. The procedure is repeated until convergence is reached. The curves are built by reporting the energy values obtained in each step and all the optimization strategies converge approximately to the same energy value. As can be observed in figure 4.3, during the derivatives calculation steps, the number of evaluated Pauli strings is negligible with respect to the ones evaluated during the ansatz parameters optimization steps. Moreover, the Pauli strings that must be evaluated to determine the derivatives are partially included in the set corresponding to the Hamiltonian. Thus their values have been calculated only in the last step of the last ansatz optimization procedure. In addition, for the non-adiabatic methods, the expectation values of the strings can be used in the same Hamiltonian optimization, until the ansatz parameters are changed. Figure 4.3 shows that the non-adiabatic Newton-Raphson method requires one more VQE than the other non-adiabatic methods to converge, but the corresponding Hamiltonians are composed of a smaller number of Pauli strings with respect to the BFGS and the trust region optimization strategies. As a consequence, the non-adiabatic

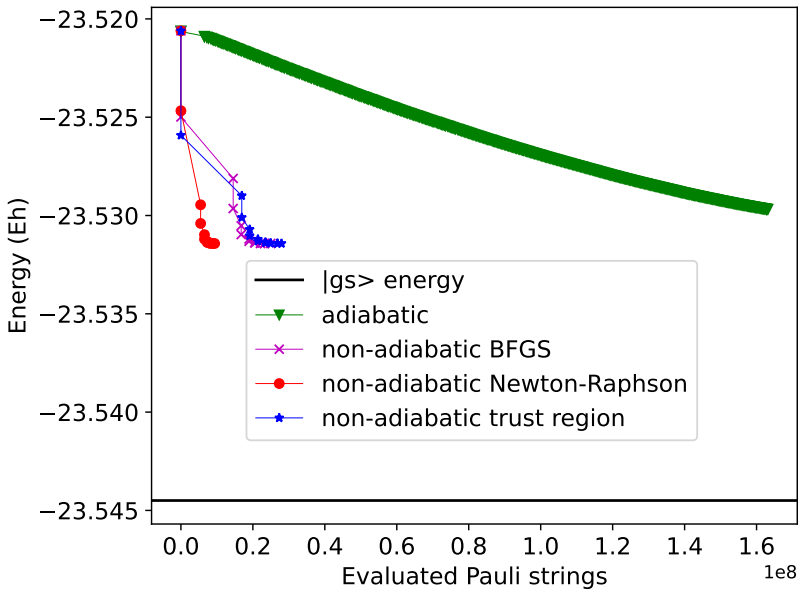

Figure 4.4: Performance of the different optimization strategies for the H_2O molecule. The obtained energies are reported as a function of the evaluated Pauli strings.

Newton-Raphson optimization method results to be the most efficient one. On the contrary, the adiabatic steepest descent is the most expensive optimization procedure, as expected. The same considerations can be inferred for the H_2O molecular system by considering figure 4.4. In this case, the adiabatic steepest descent method not only requires much more QPU resources to be performed but also converges to higher energy with respect to the other optimization strategies. Even in this case, the non-adiabatic Newton-Raphson method is the most efficient strategy and it requires one less VQE than the other non-adiabatic strategies. Finally, in figure 4.5, we report the results obtained for the 4-sites Hubbard model in the half-filling regime. The black curve in the figure refers to the exact lowest energy eigenstate. In this case, the optimization curves are substantially different from the ones obtained for the molecules due to the presence of a region with flat energy gradients. Nevertheless, the non-adiabatic schemes quickly get out of the plateau, with the non-adiabatic trust region method resulting to be the most efficient, in contrast to what is observed in molecules.

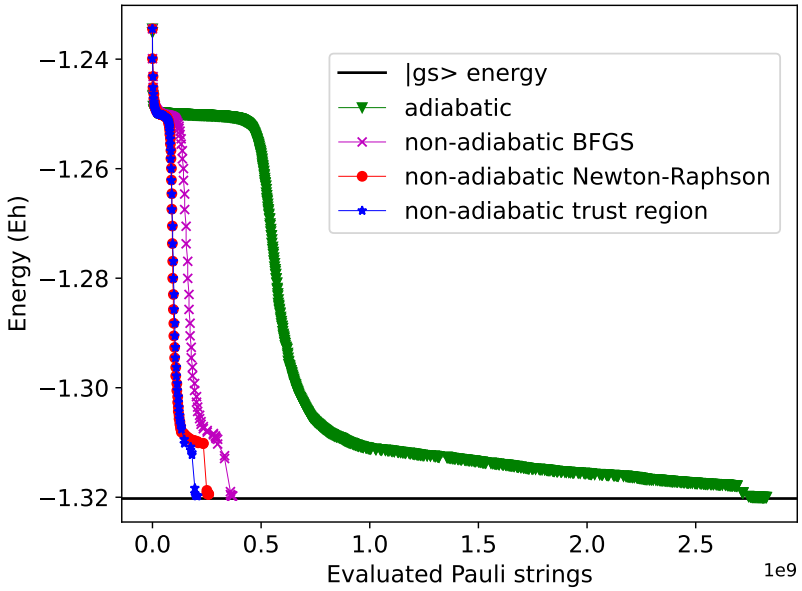

Figure 4.5: Performance of the different optimization strategies for the Hubbard system. The obtained energies are reported as a function of the evaluated Pauli strings.

4.4 Conclusions

We illustrated the non-adiabatic version of the WAHTOR algorithm [103] described in chapter 3. We compared the efficiency of three different implementations of the non-adiabatic version of the algorithm with the adiabatic one on three benchmark systems corresponding to different cost functions and qubits numbers. We showed that the QPU resources spent during the energy optimization are significantly reduced in all cases with respect to the adiabatic algorithm. This happens because the number of VQEs steps is significantly reduced during the Hamiltonian optimization, and these steps are quite demanding in terms of QPU resources.

Moreover, the resources are further reduced considering that some of the Pauli strings composing the derivatives of the cost function with respect to the Hamiltonian parameters have been evaluated in the last step on the last VQE. Each Pauli string is just measured one time until the ansatz parameters change, increasing the efficiency of the algorithm with this post-processing procedure. In particular, the non-adiabatic Newton-Raphson method was the cheapest algorithm for molecules whereas the non-adiabatic trust region was the most efficient for the Hubbard system. Both methods require the

calculation of the first and second-order derivatives, for which the analytic expression can be obtained using equations 4.12, 4.13 and 4.14. The non-adiabatic BFGS method does not require the calculation of the derivatives and never results to be the most efficient, but the estimation of the second-order derivatives is enough to reduce significantly the quantum resources requested with respect to the adiabatic method. We infer that the hessian of the cost function, or its approximation, is necessary to reach our scope. Moreover, as shown in chapter 10, we have an analytic expression of the derivative of every order for $\boldsymbol{R} = \mathbf{0}$. They can be used to implement a non-adiabatic strategy that uses higher-order derivatives, such as the Halley method, that could give an advantage for systems that remain trapped in local minima with the strategies tested up to now.[116, 117]

Chapter 5

Natural orbitals and compactness of quantum mutual information

Natural orbitals, as defined in the electronic structure and quantum chemistry theories as the molecular orbitals diagonalizing the one-particle reduced density matrix of the groundstate, have represented for decades the perfect basis set to describe electron correlation. In this chapter we show, in the case of a few representative molecules, how natural orbitals are the orbitals providing the lowest variational energies in empirical ansätze for quantum computing calculations. Interestingly, the resulting quantum mutual information matrix built on such orbitals is also maximally compact, providing a clear picture of how such orbital choice is able to provide the optimal basis to describe electron correlation. In such a way, the correlation is encoded in a smaller number of qubit pairs contributing to the quantum mutual information matrix. The optimization procedure, achieved thanks to the WAHTOR algorithm, reduces the circuit depth for correlated empirical ansatz.

5.1 Introduction

Electronic structure theory and its implementation into algorithms and computer programs allow the study of many physical and chemical processes with both theoretical and application interests. In cases where electron correlation plays an important role, high-level classical electronic structure and quantum chemistry tools are necessary, albeit they become limited by the bad scaling of the required computational time with the size of the system. Quantum devices may offer a new opportunity to tackle these problems, in principle

leading to exponential advantage. [51, 118, 37, 1] Many algorithms have been developed, including hybrid quantum-classical algorithms that use classical and quantum resources in combination, exploiting at best features of both devices. One of the most widely used algorithms is the variational quantum eigensolver (VQE) [56, 35], which has the advantage to be suited to be used with also with noisy intermediate-scale quantum (NISQ) devices [81]. The electronic structure problem is tackled by writing the molecular Hamiltonian in the second quantisation scheme and mapping fermions into qubits using one of the many encoding methods available. [23, 26, 5] The Hamiltonian is therefore written as a weighted sum of strings of Pauli operators. A variational wave function is therefore optimised by a classical computer using the quantum computer to evaluate expectation values of the Hamiltonian, efficiently calculated on the quantum processor. Variational wave functions, i.e. variational quantum circuits, used in the VQE algorithm are often inspired by existing quantum chemistry methods that have been reformulated for the creation of chemically-inspired ansätze used in quantum algorithms such as unitary Coupled Cluster (UCC). Although these ansätze represent the quantum circuit translation of well-known and widely used high-level methods in quantum chemistry, their circuit realization can be composed by a large number of quantum gates. On NISQ devices, which are limited by the coherence time and by the noise of quantum gates, heuristic ansätze are rather considered, since they can better exploit the capabilities of the hardware, at the cost of losing the chemical/physical meaning of their construction. In this paper, we analyse the mutual information matrix of shallow depth ansätze in which we optimised both the variational parameters and the orbitals used to construct the ansätze. To achieve this goal we used the non-adiabatic WAHTOR algorithm illustrated in chapter 4. The algorithm was introduced in order to have a good description of the system considered using a short circuit, improving the energy results without increasing the number of the quantum gates in the circuit. The WAHTOR algorithm finds the optimal unitary transformation of the Hartree-Fock orbital for a given ansatz of a fixed topology. In this perspective, the Hamiltonian is optimised (or, in another perspective, orbitals are optimised) in order to adapt it to the connectivity of the ansatz. From the computational point of view, this optimization is achieved by using the gradient of the energy with respect to the parameters of the unitary transformation, without significant overload. By analysing the resulting optimised orbitals we have observed that they are converging very closely to the natural orbitals basis [17, 119, 4], namely the orbitals determined by the unitary transformation that diagonalizes the one-particle reduced density matrix of that ground state. WAHTOR procedure seems therefore to lead to the finding of "maximally correlated orbitals"

which were indeed identified as natural orbitals over the years. In addition, anticipating our results, we have discovered that in this WAHTOR-optimised / natural orbital basis set, the sparsity of the mutual information matrix is indeed increased. This result is expected based on the conjecture [17] that, in the natural orbital basis set, the quantum state is expressed with fewer determinants, thus reducing the number of significantly correlated qubits pairs when the molecule is mapped on a spin system. Section 5.2 shows the computational details of the systems under consideration and in section 5.3 we show how, for the systems of study, the optimized basis sets converge to these of natural orbitals. Finally, in the last section 5.4, we focus on the key results obtained and related discussions.

5.2 Computational details

Simulated systems
We considered seven different molecular systems: H_2, LiH, HF, BeH_2, H_2O, H_2S, and NH_3. Depending on the systems we used different basis sets and frozen core approximations, as detailed in table 5.1. We use the Jordan-Wigner encoding method [23] with a number of qubits ranging from 8 to 14. The Hartree-Fock orbitals and the terms of the molecular Hamiltonian have been obtained using the PySCF Python package. [72] WAHTOR algorithm has been implemented by a in-house produced Python program exploiting the Qiskit Python libraries. [73] The variational energy results are reported in Hartree and the percentage of correlation energy is defined by

$$E_{corr} = \frac{E_{calculated} - E_{HF}}{E_{full-CI} - E_{HF}} \tag{5.1}$$

where $E_{full-CI}$ is the exact energy, $E_{calculated}$ is the energy calculated using VQE or WAHTOR algorithm and E_{HF} is the Hartree-Fock energy. Table 5.1, in addition to showing the energy results obtained, provides the value of the dimensionless parameter $\delta \in [0, 1]$

$$\delta = \frac{\sum_i (|\langle W_i|NO_i\rangle| - |\langle HF_i|NO_i\rangle|}{N - \sum_i |\langle HF_i|NO_i\rangle|} \tag{5.2}$$

that measures how much the converged WAHTOR orbitals ($|W\rangle$) are close to the natural ones ($|NO\rangle$), calculated from the exact Full-CI state. Here N is the number of orbitals considered and $|HF\rangle$ are the Hartree-Fock ones. So the closer the δ value is to 1, the more the optimized orbitals are similar to the reference natural orbitals (corresponding to $\delta = 1$); the closer it is to

zero, the more the optimized orbitals are closer to the Hartree Fock orbitals (corresponding to $\delta = 0$).

Implementation of quantum algorithm

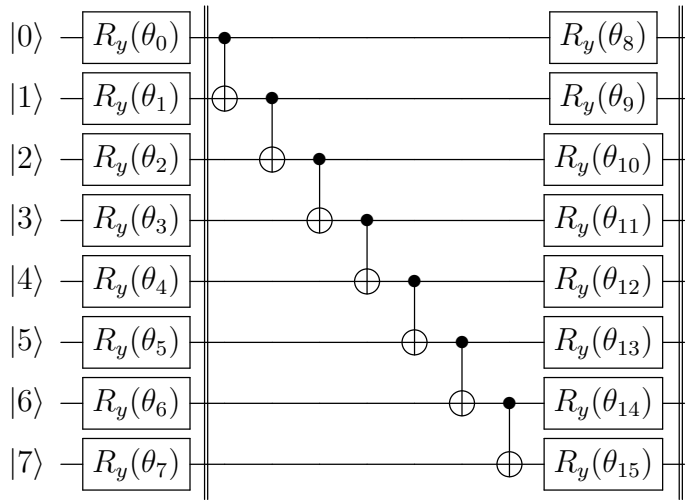

Figure 5.1: Ladder entangler map for an 8-qubits system. The quantum gates between the two barriers compose the block (identified by bold lines in the figure). Each block is repeated a certain number of times d, which is defined as the depth of the circuit.

The parametrized quantum circuit chosen in the present work belongs to the so-called heuristic ansätze build as follows. Firstly, a repetition of single qubit rotations around the y-axis is applied to the n-qubits Hartree-Fock reference state. After such rotations, an entangling block composed of CNOT gates followed by another set of independent rotations on each qubit has been applied. The block composed by CNOT gates and rotations can be therefore repeated a certain number of times, each time using different variational parameters, as shown in figure 5.1. The total number of blocks determines the circuit depth. In this chapter, we considered depth 2 for diatomic molecules and depth 4 for molecules composed of 3 or 4 atoms. CNOT gates are arranged to form a ladder, as shown in figure 5.1 for each molecule considered here except for NH_3, for which we considered an ansatz topology with less than 13 CNOT gates. For each molecular system, we execute 100 VQE runs starting from different variational parameters and the lowest energy result was considered as starting point for the WAHTOR algorithm. We optimized the ansatz parameters using the L-BFGS-B optimizer.[76] The convergence is reached when in two successive WAHTOR iterations the VQE energies differ

Table 5.1: Basis set, number of qubits, VQE and WAHTOR percentage correlation energy results and geometric distance from the reference natural orbitals for each molecule under investigation.

molecule	atomic positions (Å)	basis set	qubits	% VQE	% WAHTOR	δ
H_2	H 0.0 0.0 0.0 H 0.0 0.0 0.74	6-31g	8	47.08	98.05	0.998
LiH	Li 0.0 0.0 0.0 H 0.0 0.0 1.595	sto-3g	10	72.14	94.75	0.999
HF	F 0.0 0.0 0.0 H 0.0 0.0 0.917	sto-3g	10	71.51	93.03	0.999
BeH_2	H 0.0 0.0 0.0 Be 0.0 0.0 1.334 H 0.0 0.0 2.668	sto-3g	12	45.40	45.42	$\|HF\rangle \equiv \|NO\rangle$
H_2O	O 0.0 0.0 0.0 H 0.757 0.586 0.0 H -0.757 0.586 0.0	sto-3g	12	51.65	73.54	0.972
H_2S	S 0.0 0.0 0.0 H 0.0 0.9616 -0.9269 H 0.0 -0.9616 -0.9269	sto-3g	12	74.76	87.42	0.998
NH_3	N 0.0 0.0 0.1211 H 0.0 0.9306 -0.2826 H 0.8059 -0.4653 -0.2826 H -0.8059 -0.4653 -0.2826	sto-3g	14	36.42	41.85	0.988

less than 10^{-6} Hartree. All simulations are executed using the statevector simulator.

Implementation of derivatives

For the implementation of the WAHTOR algorithm, the matrices that determine the basis change take spin symmetry into account, i.e. the spin-up and the spin-down spin-orbitals are never linearly combined. In this way, as generators for a system with n orbitals, we have a set of $\frac{n^2+n}{2}$ symmetric and $\frac{n^2-n}{2}$ antisymmetric matrices. To further reduce computational efforts, we do not consider mixing all orbitals with the same spin but we simply linearly combine orbitals with the same spin that possesses the same geometric symmetries. Since the number of energy derivatives depends on the number of non-zero rotation parameters, it is considerably reduced by taking into account the above-mentioned symmetries.

Quantum mutual information matrix

To study the correlation present in our wave functions, VQE, WAHTOR-optimised or diagonalised ground states, we consider the quantum mutual information between the qubits that map the spin-orbitals of the system under consideration. The quantum mutual information between qubits i and j is defined as

$$I_{ij} = (S_i + S_j - S_{ij})\delta_{ij} \tag{5.3}$$

where S_{ij} and S_j are, respectively, the one and two qubits Von Neumann entropy defined as follows

$$S_k = -Tr(\rho_k log \rho_k) \tag{5.4}$$

Here k is a set of one or two indices belonging to the set of all qubits Ω and ρ_k is the reduced density matrix obtained from the density matrix ρ tracing out over all the indices not belonging to k

$$\rho_k = Tr_{\{\Omega - k\}}(\rho) \tag{5.5}$$

We represent the quantum mutual information as a symmetric matrix with elements along the diagonal equal to zero by definition, as done in [82]. The value of the correlation between the qubits can be observed in the upper or the lower triangular part of this matrix.

5.3 Results

In this section, we describe the results obtained by applying VQE and WAHTOR algorithms to the molecules considered.

The obtained energy values are summarised in table 5.1 where in the fifth and sixth columns, we show the percentage of correlation energy for the VQE and WAHTOR algorithms respectively. We note that, for each molecule, our method always improves the VQE results. Interestingly, in the case of BeH_2 the orbital optimization does not change significantly the energy value, the reasons for this pitfall will be clearer after the orbital analysis and we will come back to this point later in the text. In the last column of the table we reported the δ parameter, as defined in section 5.2. This parameter is a measure of the distance between optimised orbitals and natural orbitals, ranging from $\delta = 0$ (Hartree-Fock orbitals) to $\delta = 1$ (pure natural orbitals). Our WAHTOR procedure is therefore leading to orbitals which are extremely close to natural orbitals. We can therefore make the conjecture that the WAHTOR algorithm is guiding the Hamiltonian (i.e. rotating the orbitals) in such a way they are getting closer to natural orbitals, which can be in principle obtained only by diagonalizing the one-body density matrix. In the case of BeH_2 molecule, table 5.1 reports a value of $\delta = 1$. This means that, in this case, the Hartree-Fock and the natural orbitals coincide. As a consequence, our algorithm does not optimize the VQE results, as shown in the same table. This exception is therefore further supporting our conjecture. In order to better understand and interpret the obtained result, let us proceed with a deeper analysis of the correlation between the spin-orbitals of the molecules. As an example, in the following, we will investigate the H_2O molecule, albeit the same conclusions can be found when analysing the other systems. We would like first to point out that, by using the Jordan-Wigner mapping, the occupancy of each spin-orbital is associated with the state of a single qubit. Therefore, on a given quantum state, the correlations between the occupations of the spin-orbitals can be analyzed through the study of the correlations between the qubits. For this purpose, we use the quantum mutual information matrix defined in the previous section to better understand the map of electron correlation in our states. In particular, figure 5.2 shows the maps for the states of the H_2O molecule that we consider significant. Considering that the first half of the qubits represent the orbitals with spin up while the second half represents the same orbitals with reversed spin, each mutual information map is clearly symmetrical with respect to the diagonal and we can focus only on the lower or upper triangular part. We define the VQE and WAHTOR states as the ones obtained after the application of the corresponding algorithm. Then the VQE state is expressed in the Hartree-Fock molecular basis set and shown in panel (a) of the figure 5.2 while the WAHTOR state, expressed in the converged basis set, is reported in panel (b). Panels (c) and (d) show the groundstate mutual information matrices both for the Hartree-Fock molecular orbitals and

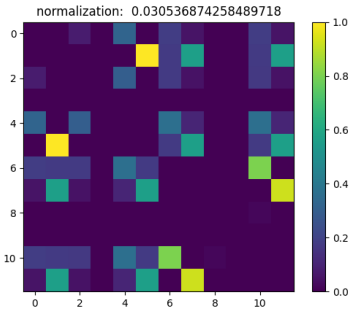

(a) VQE state in HF molecular orbitals

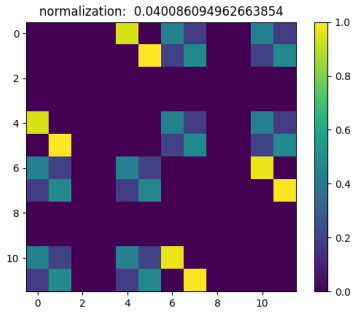

(b) WAHTOR state in converged molecular orbitals

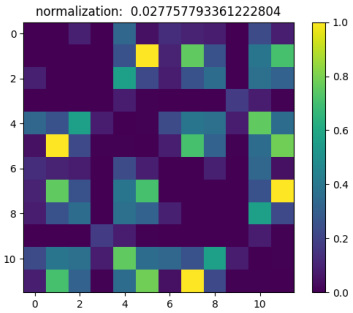

(c) Groundstate in HF molecular orbitals

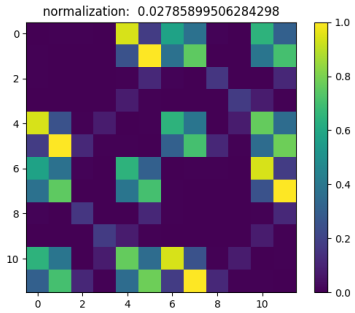

(d) Groundstate in converged molecular orbitals

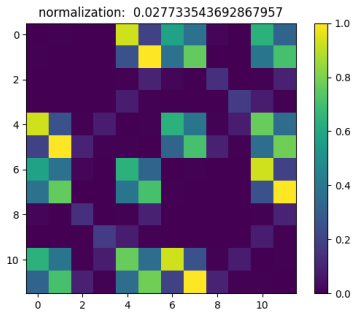

(e) Groundstate in natural molecular orbitals

Figure 5.2: Quantum mutual information maps for H_2O molecule. States and basis sets considered are described in the main text.

for the WAHTOR converged molecular orbitals, respectively. Finally, panel (e) is related to the groundstate of the H_2O system in the natural orbital basis set. Since the molecular Hamiltonian is symmetric for spin inversion, the groundstate preserves this symmetry: this feature can be seen from any groundstate mutual information matrix, see panels (c), (d) and (e) of figure 5.2, as the matrix values related to the correlation between orbitals with the same spin are equal to each other, i.e., considering the upper triangular part of the matrix, the two triangular blocks above the diagonal have the same coloured spots. Note that this symmetry is broken in the VQE state (figure 5.2(a)) and recovered in the WAHTOR state (figure 5.2(b)). Moreover, the number of green and yellow coloured spots in panel (b) is increased with respect to the ones in panel (a) while the number of blue spots decreases. This means that the quantum mutual information, during the optimization, has been compacted on a lower number of qubits pairs. This feature can be observed also comparing the groundstate expressed in Hartree-Fock and converged molecular basis set in panels (c) and (d) respectively.

Figure 5.3 quantifies the variations in quantum mutual information between qubits pairs sorted in a decreasing way for the states mentioned above, related to the matrices in figures 5.2(a), 5.2(b), 5.2(c) and 5.2(d). The number of correlated qubits pairs for the WAHTOR state and the ground state in converged basis are less than pairs in the VQE and in the ground state in Hartree-Fock basis, respectively. Meanwhile, the values of correlations between the qubit pairs of the state in the converged basis set are higher than the ones in the corresponding state in the canonical basis. This confirms what we observed in figure 5.2 for the H_2O molecule. In chapter 10, we show that these conclusions can be extracted from the other molecules considered in this work when we compare the groundstate in Hartree-Fock and in the converged basis set. Focusing on the converged molecular basis set, it has been conjectured [17] that, for a given accuracy, the natural orbitals are the basis set in which the wavefunction is expressed with the lowest number of Slater determinants. In terms of correlations between spin-orbitals, we expect that as the number of determinants in the wavefunction increases, as more the number of coloured spots in the quantum mutual information matrices increases. This is exactly what we observe in our systems and we suggest that the Hamiltonian optimization procedure converges to the natural orbitals if we order them in such a way that the i-th orbital is the most similar to the i-th converged orbital. In order to study the similarity of the WAHTOR-optimized orbitals to the natural orbitals of the system, the δ parameter, defined above, was calculated. In table 5.1 are reported the values of δ for the different benchmark molecules and we note that these are close to one, regardless of the considered system. Then we can state that

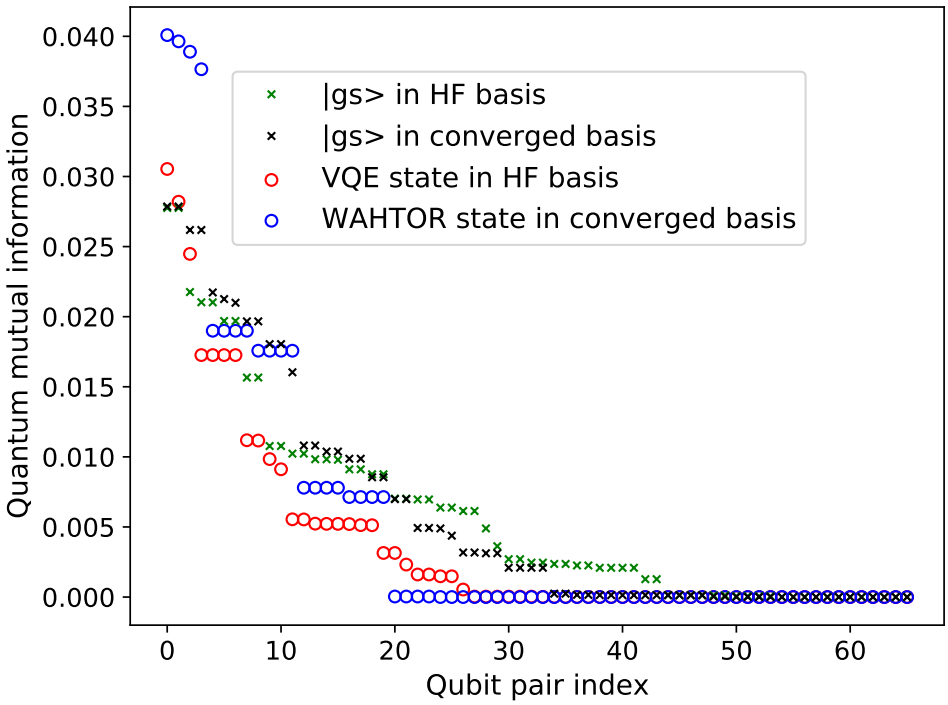

Figure 5.3: Quantum mutual information for H_2O molecule, qubits pairs are ordered in descending way. The quantum mutual information is spread out on a smaller number of qubit pairs in the converged basis set with respect to the Hartree-Fock one.

the orbitals converge to the natural ones because this conjecture is verified for different molecular geometries, qubit sizes and energy results. The most striking result is the NH_3 molecule, for which we considered a specific heuristic depth 4 ansatz topology. Although this is not sufficient to obtain good energy results neither with VQE nor with WAHTOR, δ parameter shows that the optimized molecular basis set converges to the natural orbitals. For the H_2O molecule, this can also be seen in figure 5.2 comparing the panels (d) and (e) and noting that the images are identical because they represent the groundstate in the same basis set. Similar considerations can be deduced for the other molecules by comparing the images in chapter 10.

5.4 Conclusions

In this chapter, we showed that the natural orbitals are the ones that provide the lowest variational energy for the systems under consideration when the

orbitals are optimized by using the WAHTOR algorithm. A parameter δ has been defined to quantify the distance between the converged orbitals and the natural ones. Results show that the algorithm converges to the natural orbitals regardless of the symmetries, the number of qubits and the accuracy of the VQE results (at least for the reasonable values shown in this chapter) for the molecules under consideration, as shown in 5.1. In terms of the quantum mutual information, this is translated into an increased sparsity of the corresponding matrix.

Chapter 6

SU(N) fermions

6.1 Introduction

Hubbard's model is fundamental to investigating strongly correlated many-body quantum systems. We refer to the Hubbard system with N spin components as SU(N) fermions, these models can be found in high energy physics [120] and in condensed matter physics. [121] SU(N) fermions can be even experimentally realized with ytterbium atoms, as shown in. [122] Finding the groundstate of these systems is a challenging task and quantum algorithms could give us the opportunity to reach this goal. [109] In this chapter, we generalize the unitary transformation introduced in chapter 3 by considering the proper Bogoliubov transformations and by applying the method to the SU(N) fermionic systems.

6.2 The method

Consider a system made of M lattice sites and L spin components. The corresponding single-particle states are associated with a set of creation and annihilation operators $\{a^\dagger_{o\sigma}, a_{o\sigma}\}$, where $o = 1, \ldots, M$ and $\sigma = 1, \ldots, L$. The Hubbard model Hamiltonian describing the strongly interacting $SU(N)$ fermionic system is

$$H = \sum_{o \neq p}^{M} -\left(t_{op} a^\dagger_{o\sigma} a_{p\sigma} + t^*_{op} a^\dagger_{p\sigma} a_{o\sigma}\right) \sum_{o=1}^{M} \sum_{\sigma \neq \tau}^{L} U_o n_{o\sigma} n_{o\tau} + \sum_{o \neq p}^{M} V_{op} n_o n_p \qquad (6.1)$$

where $n_{o\sigma} = a^\dagger_{o\sigma} a_{o\sigma}$ and $n_o = \sum_{\sigma=1}^{L} n_{o\sigma}$ is the number operator for site o. Here, $t_{op} \in \mathbb{C}$ is the hopping term between sites o and p, $U_o \in \mathbb{R}_0^+$ is the repulsive on-site potential on site o and $V_{op} \in \mathbb{R}_0^+$ is the density-density repulsive

interaction between sites o and p. By varying the values of these parameters, different phases can be investigated. To apply the method defined in chapters 3 and 5, we define a set of cumulative indices $i, j, c, d, e, f = o + (\sigma - 1)M$, going from 1 to ML , and write the model Hamiltonian as

$$H = \sum_{ij=1}^{ML} h_{ij}^1 a_i^\dagger a_j + \sum_{cdef}^{ML} h_{cdef}^2 a_c^\dagger a_d^\dagger a_e a_d \tag{6.2}$$

where h_{ij}^1 is the one-body integral and h_{cdef}^2 is the two-body one, both of them can be derived from the values of the parameters in equation 6.1. As shown in chapters 3 and 5, the Hamiltonian is invariant under a change of single-particle basis. This means that, given a unitary matrix Υ, one can define a set of operators $\{b_i^\dagger\}$ satisfying the anticommutation relations 2.15 such that

$$b_i^\dagger = \sum_\alpha \Upsilon_{\alpha i} a_\alpha^\dagger \qquad \Upsilon\Upsilon^\dagger = I \tag{6.3}$$

Where I is the identity matrix. We called the new operators $b_i^\dagger$, as done in section 2.2, to avoid confusion in the following discussion. By defining the $\hat{k}$ operator as follow

$$\hat{k} = \sum_{ij} k_{ij} a_i^\dagger a_j \qquad k^\dagger = -k \tag{6.4}$$

the unitary operator $e^{\hat{k}}$ is obtained, so that the $\tilde{H} = e^{-\hat{k}} H e^{\hat{k}}$ has the same spectrum of H. So, for a fixed state $|\psi\rangle$, the optimal $\tilde{H}$ that minimize $\langle\psi| \tilde{H} |\psi\rangle$ respect to the parameters k_{ij} can be determined. The WAHTOR algorithm alternates the optimizations of the parametrized ansatz with the optimization of the Hamiltonian described above to reach the lowest energy expectation value. By exploiting the Nambu formalism we define the vector $\mathbf{\Psi}$ and $\mathbf{\Psi}^\dagger$ as

$$\mathbf{\Psi} = \begin{pmatrix} a_1 \\ . \\ . \\ . \\ a_{ML} \\ a_1^\dagger \\ . \\ . \\ . \\ a_{ML}^\dagger \end{pmatrix} = \begin{pmatrix} a \\ a^\dagger \end{pmatrix} \qquad \mathbf{\Psi}^\dagger = \begin{pmatrix} a^\dagger & a \end{pmatrix} \tag{6.5}$$

and the corresponding transformed ones, $\mathbf{\Phi} = \begin{pmatrix} b & b^\dagger \end{pmatrix}^T$ and $\mathbf{\Phi}^\dagger = \begin{pmatrix} b^\dagger & b \end{pmatrix}$. In this formalism, the transformation considered in chapter 3 assume the

following form

$$\mathbf{\Phi} = W^\dagger \mathbf{\Psi} = \begin{pmatrix} \Upsilon^\dagger & 0 \\ 0 & \Upsilon^T \end{pmatrix} \mathbf{\Psi} \tag{6.6}$$

where with W we represent the unitary transformation and 0 is the zero square matrix of dimension $2M$ (since $L = 2$). Now, we want to generalize this approach by considering a transformation that is linear in the creation and annihilation operators and such that $(b^\dagger)^\dagger = b$, thus

$$\mathbf{\Phi} = W^\dagger \mathbf{\Psi} = \begin{pmatrix} \Upsilon^\dagger & \Lambda^\dagger \\ \Lambda^T & \Upsilon^T \end{pmatrix} \mathbf{\Psi} \tag{6.7}$$

We require that the transformed operators verify the anticommutation relations, i.e. $\{\Phi_i, \Phi_j^\dagger\} = \delta_{ij}$, giving rise to a set of quasiparticles. In terms of the W matrix, this means that $WW^\dagger = I$, so any unitary matrix defined as in equation 6.11 can be taken into account. Such a transformation is known as Bogoliubov transformation [123, 124] and is extensively used in high energy physics and in condensed matter physics [125, 126]. It can be easily seen that any matrix satisfying the following properties

$$FWF = W^* \qquad F = \begin{pmatrix} 0 & I \\ I & 0 \end{pmatrix} \qquad WW^\dagger = I \tag{6.8}$$

is associated with a Bogoliubov transformation. These matrices form a subgroup of the unitary ones, indeed

$$FW_1W_2F = FW_1FFW_2 = W_1^*W_2^* \tag{6.9}$$

To better describe this group we rotate all the matrices by defining $S = GWG^\dagger$, where

$$G = \sqrt{\frac{i}{2}} \begin{pmatrix} I & -iI \\ iI & -I \end{pmatrix} \qquad GG^\dagger = I \qquad G^TG = F \tag{6.10}$$

From the properties of G we obtain that $S = S^*$ and $S^TS = I$, so the S matrices belong to the orthogonal group $O(2ML)$. Their determinant is 1 or -1 but we are interested in the matrices that can be obtained from the identity by varying some parameters because they will be used to parametrize the Hamiltonian. Thus we consider the subgroup $SO(2ML)$ of orthogonal matrices with the determinant 1, the set of the so-called proper Bogoliubov matrices. Finally, in analogy with the notation used in chapter 3, we can write

$$W(\boldsymbol{R}) = e^{i\boldsymbol{R}\cdot\boldsymbol{T}} \qquad T_j = -iG^\dagger t_j G \qquad t_j^T = -t_j \tag{6.11}$$

where $\boldsymbol{R}$ is a real vector and $\boldsymbol{t}$ is the vector such that the components are a set of generators of $SO(2ML)$. By defining the hermitian matrix $k = \boldsymbol{R} \cdot \boldsymbol{T}$, we have that $k^\dagger = k$ and $FkF = -k^*$. From these properties, we obtain that

$$e^{i\hat{k}} \Psi_j e^{-i\hat{k}} = \Phi_j \qquad \text{where} \qquad \hat{k} = \frac{1}{2} \sum_{ij} k_{ij} \Psi_i^\dagger \Psi_j \tag{6.12}$$

that is a generalization of the relation shown in chapter 2.2. The transformed of the creation or annihilation operators Ψ_j are the generalized ones Φ_j that verify the anticommutation relations, so we can interpret them as generalized creation or annihilation operators corresponding to the quasiparticle introduced above. Note that, in this case, the vacuum state $|\tilde{\varnothing}\rangle$ is different from the starting one $|\varnothing\rangle$ because it is defined as the state that is annihilated by the application of any b_i operator. By using the equation 6.12, it follows that

$$b_i |\tilde{\varnothing}\rangle = e^{i\hat{k}} a_i e^{-i\hat{k}} |\tilde{\varnothing}\rangle = 0 \quad \rightarrow \quad |\tilde{\varnothing}\rangle = e^{i\hat{k}} |\varnothing\rangle \tag{6.13}$$

Resuming, we can generate a set of quasiparticles parametrized by $\boldsymbol{R}$ through the equation 6.11 such that the generalized vacuum state verify the equation 6.13. The Hamiltonian can be expressed in terms of quasiparticles by defining the one-body and two-body integrals in the Nambu formalism as

$$H^1_{ij} = h^1_{ij} \theta(ML - i) \theta(ML - j) \tag{6.14}$$

$$H^2_{cdef} = h^2_{cdef} \theta(ML - c) \theta(ML - d) \theta(ML - e) \theta(ML - f) \tag{6.15}$$

where $\theta(x) = 1$ if $x \geq 0$ and $\theta(x) = 0$ if $x < 0$. Thus Hamiltonian assumes the following form

$$H = \sum_{i,j=1}^{2ML} \Psi_i^\dagger H^1_{ij} \Psi_j + \sum_{c,d,e,f=1}^{2ML} \Psi_c^\dagger \Psi_d^\dagger H^2_{cdef} \Psi_e \Psi_f \tag{6.16}$$

that, in the single quasiparticles basis set, becomes Finally, by exploiting the relation in equation 6.7, we obtain the requested parametrized Hamiltonian in terms of quasiparticles

$$H = \sum_{i,j=1}^{2ML} \Phi_i^\dagger H^1(\boldsymbol{R})_{ij} \Phi_j + \sum_{c,d,e,f=1}^{2ML} \Phi_c^\dagger \Phi_d^\dagger H^2(\boldsymbol{R})_{cdef} \Phi_e \Phi_f \tag{6.17}$$

where

$$H^1(\boldsymbol{R})_{ij} = \sum_{\alpha,\beta=1}^{2ML} W(\boldsymbol{R})^\dagger_{i\alpha} H^1_{\alpha\beta} W(\boldsymbol{R})_{\beta j} \tag{6.18}$$

$$H^2(\boldsymbol{R})_{cdef} = \sum_{\gamma,\delta,\epsilon,\zeta=1}^{2ML} W(\boldsymbol{R})^\dagger_{c\gamma} W(\boldsymbol{R})^\dagger_{d\delta} H^2_{\gamma\delta\epsilon\zeta} W(\boldsymbol{R})_{\epsilon e} W(\boldsymbol{R})_{\zeta f} \tag{6.19}$$

The transformed Hamiltonian $H(\boldsymbol{R}) = \tilde{H}$, by exploiting the relation 6.12, is simply

$$H(\boldsymbol{R}) = \sum_{i,j=1}^{2ML} \Psi_i^\dagger H^1(\boldsymbol{R})_{ij} \Psi_j + \sum_{c,d,e,f=1}^{2ML} \Psi_c^\dagger \Psi_d^\dagger H^2(\boldsymbol{R})_{cdef} \Psi_e \Psi_f \tag{6.20}$$

Given a parametrized quantum circuit representing the quantum state $|\Lambda(\boldsymbol{\theta})\rangle$, the cost function introduced in chapter 4 can be taken into account

$$\langle \Lambda(\boldsymbol{\theta})| \, H(\boldsymbol{R}) \, |\Lambda(\boldsymbol{\theta})\rangle \tag{6.21}$$

and be minimized with respect both sets of parameters by using one of the strategies illustrated in figure 4.2.

6.3 Computational details

In this section, we specify the details of the investigated systems. We choose the Jordan-Wigner encoding method so each qubit encodes the occupation of the fermionic single-particle state. All the simulations have been executed using the statevector simulator. For each system, we considered two parametrized unitary transformations: the first one is the Bogoliubov transformation in equation 6.11, referred as W_B, while the second one, called W_r, corresponds to the basis change and is represented by the matrix in equation 6.6. Obviously, W_r is a subgroup of W_B but we consider both of them to compare the possible improvement given by the description in terms of quasi-particles. Moreover, for both transformations, we applied the same unitary matrix on the different spin components. Thus we have M^2 and $2M^2 - M$ parameters respectively for the W_r and the W_B matrices, as can be easily deduced from the dimension of the groups associated.

6.3.1 Simulated systems

We considered systems with three sites and three components of spin, belonging to the SU(3) group, this means that all systems are composed of 9 qubits. We consider a closed linear chain with translation invariance symmetry, so the parameters in equation 6.1 assume the same values on each site and the interaction is between nearest-neighbours. The following values for the parameters in equation 6.1 are considered:

- t=1 U=5 V=0
- t=1 U=10 V=0

- t=1 U=5 V=10

We are looking for the eigenstate of the Hamiltonian with one particle in each site with the lowest energy, $|GS_{111}\rangle$. Since the groundstates of the benchmark systems do not verify this condition we introduce the penalty C in the cost function

$$C = \mu \sum_i (n_i - 1)^2 \tag{6.22}$$

where μ is the chemical potential and n_i is the number of particles at site i. The value of the μ parameter must be at least equal to the value such that $C = E_{GS} - E_{111}$, where E_{GS} is the energy of the groundstate while E_{111} is the energy corresponding to $|GS_{111}\rangle$. We choose $\mu = U + V$ for each system to guide the ansatz optimization on states with the right number of particles. When we consider the W_B, C change is value even during the Hamiltonian optimization because the number of particles is not preserved by this transformation, so the penalty must be considered in the cost function during this step. All the energy results are expressed in Hartree (Eh).

6.3.2 Ansatz construction

For the parametrized quantum circuit we have chosen the heuristic ansatz built by applying an R_Y quantum gate on each qubit followed by an entanglement block repeated d times, where d is the depth of the circuit. The fermionic single-particle state referred to by the lattice site m and colour l is mapped on the qubit corresponding to the index $i = m + M(l - 1)$. This means that the qubits from index 0 to index 2 are related to the first colour, the ones ranging from index 3 to index 6 are related to the second colour and the last three are associated with the third colour. In figure 6.1 we reproduced an example of the ansätze used in our simulations, the entanglement block is delimitated by the vertical barrier and, in this case, it is repeated just one time. Each block is composed of 8 CNOTS gates, the first 6 entangle the qubits corresponding to the same colours while the remaining ones entangle the different colours. In our simulations, we have considered circuits with depths 6,7 and 8.

6.4 Results

In this section, we describe the results obtained for the model Hamiltonian illustrated above. For each considered system, we executed 30 VQE runs and, for each of them, two Hamiltonian optimizations were performed, one with

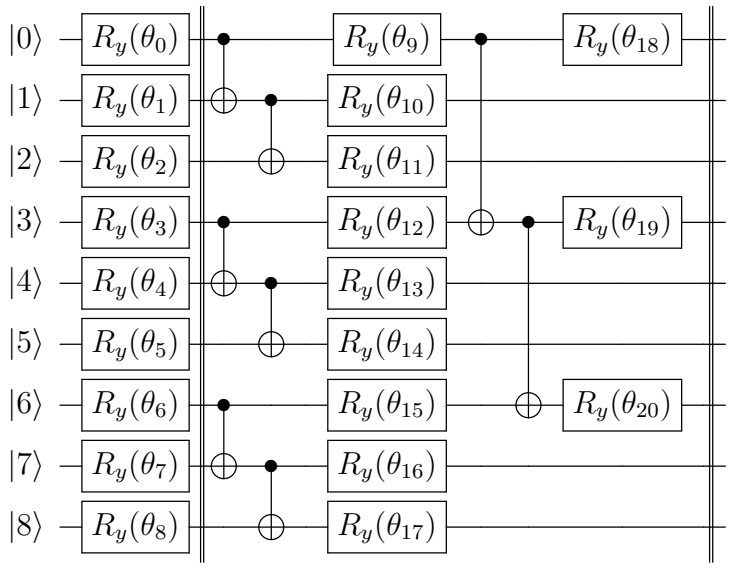

Figure 6.1: Ladder entangler map for SU(3) systems. The quantum gates between the two barriers compose the block that is repeated the number of times defined by the circuit depth.

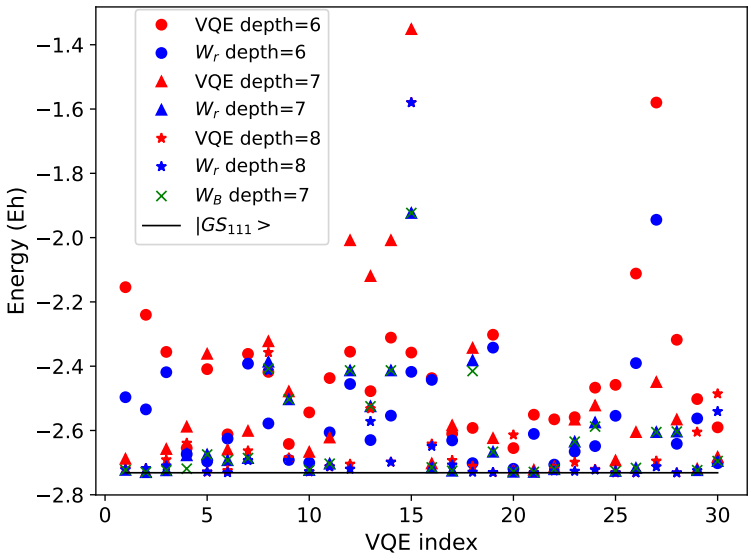

Figure 6.2: Energy results for the system with parameters t=1, U=5, V=0, $\mu = 5$.

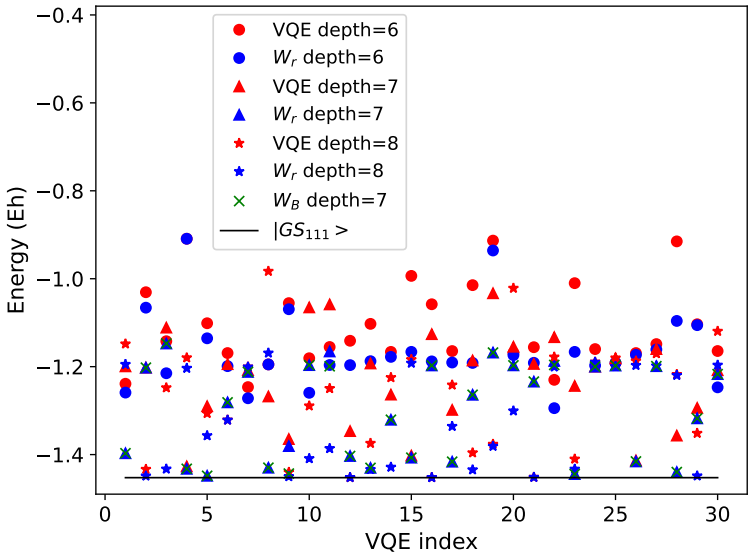

Figure 6.3: Energy results for the system with parameters t=1, U=10, V=0, $\mu = 10$.

W_r and the other one with W_B. In all the following figures, red marks are associated with the VQE results for different depths while the blue ones are related to the WAHTOR results, corresponding to the Hamiltonian transformation W_r. For each depth, ranging from 6 to 8, we have an associated marker. The energy obtained by optimizing the Hamiltonian through the Bogoliubov transformation W_B is represented with green crosses. Finally, black lines show the energy of the groundstate with the requested number of particles for each colour $|GS_{111}\rangle$. In all the figures the energies are reported for each VQE index, this means that each run is completely independent of the other ones. Moreover, for each index, we show the energy results obtained by optimizing the Hamiltonian using the W_r and the W_B transformations defined above, starting from the VQE state associated with that index. This procedure is executed for each depth when W_r is taken into account, giving rise to three different markers for each colour, as shown for example in figure 6.2. The Hamiltonian has been optimized with W_B only for the ansatz corresponding to depth 7. In figure 6.2 we show the energy results obtained for the first considered system, corresponding to the parameters t=1, U=5, V=0 and $\mu = 5$. We note that the Hamiltonian optimization procedure decreases significantly the energy obtained from the VQE for each considered ansatz. By increasing the depth, we statistically improve the probability to reach the lowest possible energy for both VQE and the Hamiltonian opti-

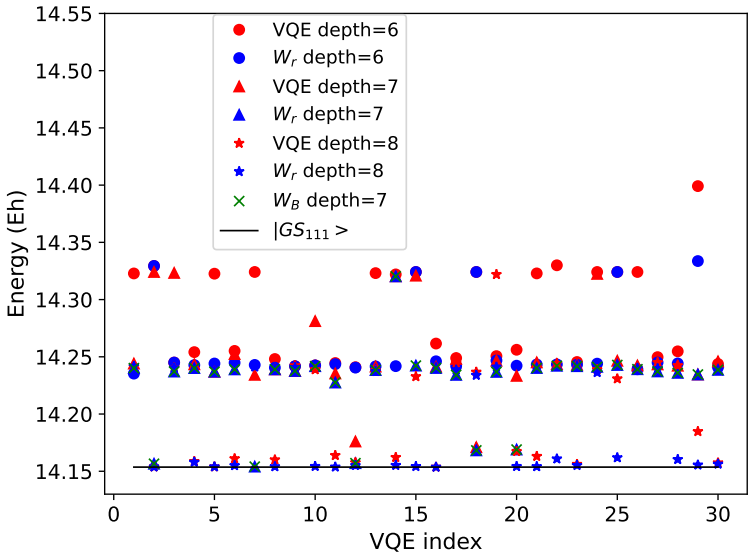

Figure 6.4: Energy results for the system with parameters t=1, U=5, V=10, $\mu = 15$.

mization algorithms. Note that the results corresponding to lower depth can achieve lower results with respect to a higher depth for certain VQE indices, as shown for index 5 (compare depth 6 with depth 7). This is not weird because, obviously, runs corresponding to different ansatz are completely independent of each other. By focusing on the ansatz corresponding to depth 7, we note that the Bogoliubov transformation does not statistically improve the results obtained with the W_r transformation, showing that the latter is enough to reach the groundstate. Similar results have been obtained for the system corresponding with parameters t=1, U=10, V=0, μ=10, as shown in figure 6.3. Also in this case the VQE energies are improved when the optimization of the Hamiltonian is performed but, in contrast, at least a depth of 7 is requested to reach the groundstate and a depth of 8 for statistically relevant results. For the W_B transformation, the same conclusions inferred above are still valid. Finally, in figure 6.4 we report the results related to the system with parameters t=1, U=5, V=10, μ=15. The distribution of the results is different with respect to the cases shown above because many data are localized around two energy values (14.24 and 14.32 Hartree), giving rise to two local minima. To reach the groundstate at least depth 7 is required but we note that, to statistically reach the goal, depth 8 is necessary. For this system, W_B and W_r transformations give the same results.

Chapter 7

Quantum Information Driven Ansatz (QIDA)

Hardware-efficient empirical variational ansätze for Variational Quantum Eigensolver simulations of Quantum Chemistry suffer by the lack of a direct connection to classical Quantum Chemistry methods. In the present work, we propose a method to fill this gap by introducing a new approach for constructing variational quantum circuits, leveraging quantum mutual information associated with classical Quantum Chemistry states to design simple yet effective heuristic ansätze with a topology that reflects the correlation of the molecular system. Quantum Chemistry calculations, such as Møller-Plesset (MP2) perturbation theory, firstly provide an approximate natural orbitals basis, which, in chapter 5, shown to be the best candidate basis set for developing compact empirical wavefunctions. Secondly, they provide information about the correlation between qubits of the quantum circuit, enabling the development of a direct design of entangling blocks for the circuit. The resulting ansatz is then utilized with a VQE to obtain a variational groundstate of the electronic Hamiltonian. To validate our approach, we perform a comprehensive statistical analysis over various molecular systems (H_2, LiH, H_2O) and apply it to the more complex NH_3 molecule. Our results demonstrate that the proposed methodology gives rise to highly effective ansätze, surpassing the standard empirical ladder-entangler ansatz in performance. Overall, our approach provides a promising solution for designing efficient variational quantum circuits for large molecular systems.

7.1 Introduction

The advent of quantum computers promises to drastically reduce the computational cost of specific tasks with respect to their classical counterparts. With applications ranging from cryptography [85] to finance [89], the public interest in the field has in recent years grown immensely [127], particularly for its academic applications in the field of natural sciences.[128] In line with one of the precursors proposals of quantum computing [47], one of the most promising fields is thought to be Quantum Chemistry, which aims to tackle the electronic structure of large molecules where electron correlation play a crucial role. A widely known method for near-term applications in quantum chemistry is the Variational Quantum Eigensolver (VQE) [35, 129, 66], used to variationally approximate the groundstate of a molecular Hamiltonian by routinely measuring on the Quantum Processing Unit (QPU) the energy of a parameterized quantum circuit, i.e. the wavefunction ansatz. Different approaches to building an ansatz have been developed. Between all of them, two major classes can be found. The first consists in translating classical quantum chemistry approaches into the language of quantum computation. One of the most striking examples is the Unitary Coupled Cluster (UCC) method [130, 99, 131, 132, 133, 69, 38] which is a unitary implementation of the widely used Coupled Cluster classical method. The second approach, on the contrary, starts from wavefunctions that are directly built exploiting the characteristic of the quantum hardware, regardless of connection with the chemistry of the problem. This empirical approach defines the so-called heuristic ansatz [44, 103], which is composed of repetitions of blocks of rotations and entanglements, set up without any information about the chemical problem. Compared to the former approach, this one better exploits the capabilities of the quantum hardware, at the price of losing the chemical meaning of the variational ansatz. Our work falls within the realm of the latter method, integrating knowledge derived by a classically computed Møller-Plesset (MP2) [134] groundstate (GS) to infer the expected properties of the VQE ansatz circuit. The central physical quantity for our analysis is the Quantum Mutual Information (QMI), which even in classical quantum chemistry has proven to be a useful guide to improve existing algorithms.[135] To further enhance the results offered by our scheme, we also make use of the tool of the Natural Orbitals (NO). In the following sections, we introduce the Quantum Information Driven Ansatz (QIDA) method, giving a full explanation and applying it to its full extent to the benchmark systems H_2, LiH, H_2O, we then test its effectiveness on the NH_3 molecule.

7.2 QIDA

7.2.1 Quantum mutual information metrics

The aim of measuring correlations in quantum systems can be achieved in many ways, and to this day it constitutes a field of research by itself. [136, 137] One of the most prominent and oldest measures is the Von-Neumann quantum mutual information.[138] Let $\mathscr{H}_A$ and $\mathscr{H}_B$ be two Hilbert spaces and ρ_{AB} be a density matrix, the quantum mutual information I of ρ_{AB} is defined as:

$$I(A,B) = S(A) + S(B) - S(A,B) \tag{7.1}$$

where S are the Von Neumann entropies defined as

$$\begin{aligned} S(A,B) &= -tr(\rho_{AB} log(\rho_{AB})) \\ S(A) &= -tr(\rho_A log(\rho_A)) \\ \rho_A &= tr_B(\rho_{AB}) \end{aligned} \tag{7.2}$$

As shown by equation (7.2), given an N-partite Hilbert space $\mathscr{H}_N = \bigotimes_i^N \mathscr{H}_i$ and a quantum state $\rho \in \mathscr{H}_N$, we can find the matrix $I(i,j)$ by tracing out all but the subsystems i,j. In our case, subsystems are N qubits forming the quantum register. By construction, the matrix is symmetric and the elements along the diagonal must be zero. The use of the QMI for our purpose was motivated by its simplicity and widespread knowledge in both the quantum and the classical information theory fields. Furthermore, the QMI has already been exploited to measure the correlation between orbitals in the past.[135, 139] We will later show the properties of I matrix through representation such as figure 7.1.

7.2.2 Natural orbitals

In the next sections, we make use of the NO as a tool to decrease the complexity of the circuit, using them for both QMI calculations and as orbitals for the VQEs. The NO of a given state $|\Psi\rangle$ are defined as the molecular orbitals for which the one-body Reduced Density Matrix (RDM)

$$\rho_{ij} = \langle\Psi| a_i^\dagger a_j |\Psi\rangle \tag{7.3}$$

is diagonal. Due to this diagonal condition the NO allow a more classical interpretation of the electrons' placement over the orbitals themselves. Furthermore, it has been claimed by Löwdin [17] that, in the NO basis, the configuration interaction expansion of the state under study is expressed

with the minimal number of Slater determinants. Consequently, we expect to see a sparser I matrix by replacing the Hartree-Fock [140] (HF) canonical Orbitals (HFO) with the NO. This can be seen by image 7.1, representing the I matrix for the set of benchmarking molecules taken into account in this work. For each row, by moving from columns 1(a,d,g,j HFO) to columns 2(b,e,h,k NO), the number of coloured spots decreases in favour of some dominating ones, showing that the correlation concentrates more on fewer qubits. The usefulness of this feature will become clear in the following. As we introduced, the NO are defined by diagonalization of a groundstate's RDM, implying prior knowledge of the exact solution to the problem, a.k.a. the Full Configuration Interaction [141, 4] (FCI) solution. To overcome this problem, we consider the approximated solution obtained from an MP2 calculation [134] and retrieve the natural orbitals associated with the unitary transformation diagonalizing the RDM of this state.

7.2.3 The scheme

Resource-efficient classical quantum chemistry methods can already contain useful information for a quantum computing algorithm to solve electronic problems. This is not a new concept as indeed the starting point for VQE calculations is always the HFO basis. Starting from some other random basis wouldn't in theory compromise the principles under which the VQE works. In this chapter, we show a method that makes use of the QMI coming from a classical calculation to infer an entangling block for a hardware-efficient ansatz. As a first step, we perform a Post-HF (PHF) calculation to obtain an approximation of the GS $|\psi_{PHF,GS}\rangle$. The choice of the method is usually dictated by the size of the problem. We perform a second order Møller-Plesset (MP2)[134] calculation which scales with $O(n^5)$[4] in the number of orbitals. As a following step, we map the state $|\psi_{PHF,GS}\rangle$ on a qubit register to obtain $|\psi_{q,PHF,GS}\rangle$. At this point, we find the corresponding I matrix by using equation 7.1. Some explicit examples of these matrices are given in figure 7.1, and their values range from 0 to 1 because of an imposed normalization. Overall, we can consider these values of I as a measure of correlation [142], without discerning between the classical correlation and the quantum one. Effectively, by fixing a threshold $\mu \in [0, 1)$, we can now identify two separate sets of the pairs that fall either above or below μ. We then impose the entangling block of the VQE to be composed of CNOTs only between qubits i, j for which $I(i, j) > \mu$, leaving aside the direct imposition of the correlation of the remaining pairs or assigning it to further development of the algorithm. In this framework, coherently to usual heuristic approaches [103], the CNOT is chosen as an entangler (i.e. correlator) between qubits. Of course, other

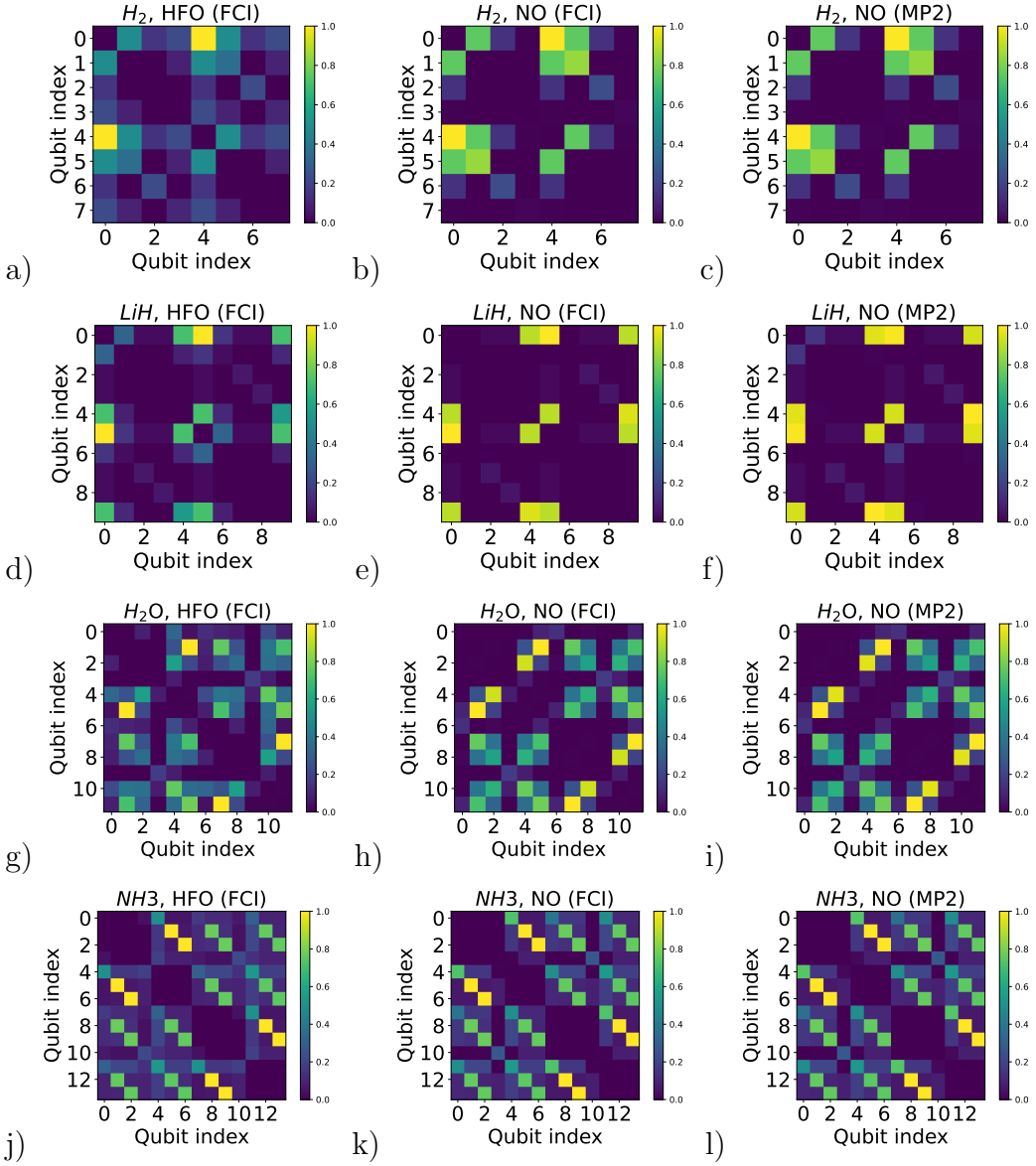

Figure 7.1: Representation of the quantum mutual information matrices $I(i,j)$ for qubits mapping the spin-orbitals of the molecular systems considered. The rows span over the molecules, while the columns span over the orbitals and the states: starting from the left we meet FCI state in HFO, FCI state in NO and MP2 state in NO.

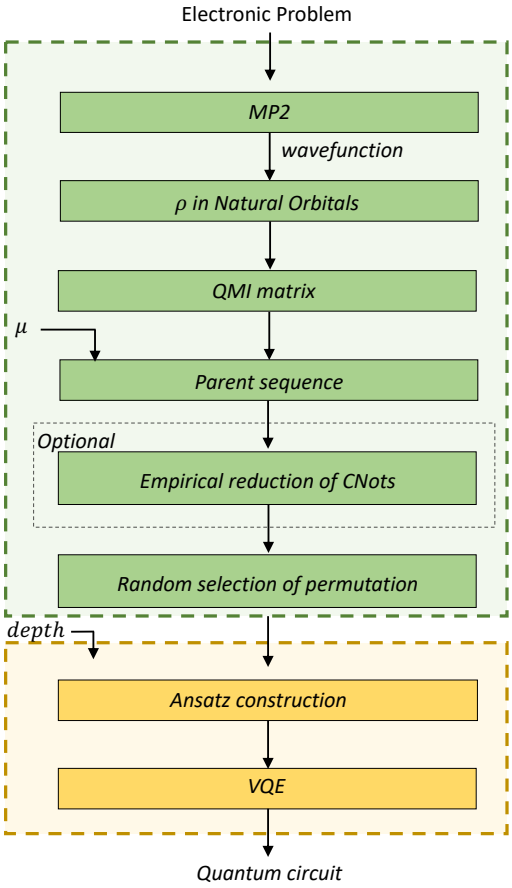

Figure 7.2: Description of the proposed scheme to obtain an ansatz from information inferred by a post-Hartree-Fock method, MP2 in this case.

two-qubit quantum gates could also make up for the same role. The general idea is that a bigger μ only selects the more relevant correlations between qubits and, by tuning the parameter, one can now choose how many CNOTs to include, sacrificing at choice the descriptiveness of the ansatz. At this point, one could further reduce the number of CNOTs of the ansatz with what is explained in the next section or proceed with the remaining technicalities of the scheme. Eventually, after having chosen a μ and having applied a reduction method, one will have selected a list of CNOTs to be applied as an ansatz, we called this list *parent* sequence. The reason for this name is that the algorithm proposed here doesn't specify the order of the involved CNOTs, and since one has to entangle at least $\mathrm{O}(n)$ qubits in a n qubit register to achieve meaningful results, the number of possible orderings will grow as $n!$. We show below that choosing a random permutation between the

$n!$, will still give better statistical results than the common ladder-entangler block with less or equal CNOTs.

Empirical reduction

The method as shown so far has the drawback of retaining the scaling of the number of CNOTs to $O(n^2)$. In this regard, we found that is possible to reduce this scaling by removing the CNOTs that encourage cross-entanglement between different qubits. We can clarify what is meant by cross-entanglement by pointing out at figure 7.1-g, in this specific case all the pairs obtained from qubits 1,5,7 have an I greater than the chosen μ between each other. Thus

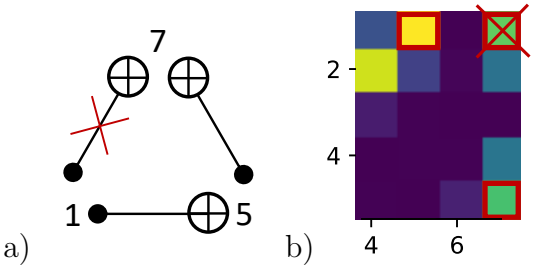

Figure 7.3: Cross-entanglement reduction, all numbers refer to the qubit indices. a) We have three CNOTs but we do not consider the one connecting the qubits 1 and 7. b) Representation on I map of the reduction, the red frame identifies the pairs that we will connect with a CNOT on the circuit while the crossed one is left out.

the original algorithm would prescribe all three pairs to have a CNOT, but with a variational algorithm and multiple depths in place, it is sufficient to connect the said qubits once each. This mainly means that it is possible to remove one of the three CNOTs, as represented in figure 7.3[a]. We represent graphically this operation by putting a red frame to the considered spots and erasing the one that will not appear on the circuit, as done in figure 7.3[b]. The approach followed by our implementation to bring this concept to the circuit was to select only the first spot from each line of the upper triangular part of the I matrix such that $I(i, j) > \mu$. As an example, figure 7.4 shows the pairs taken into account for the H_2O and NH_3 molecules.

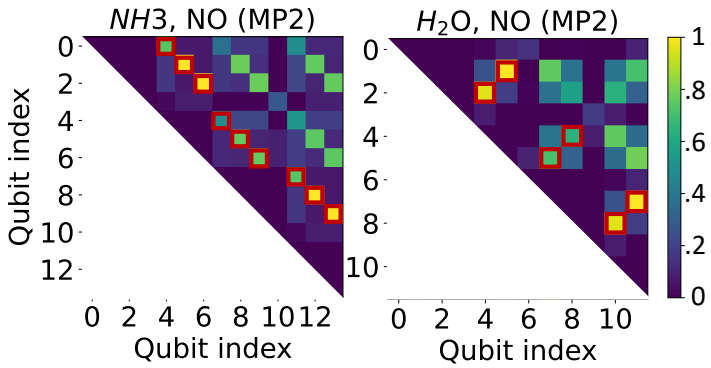

Figure 7.4: Empirical reduction criterion applied to H_2O and NH_3 molecules. As described in the main text, spots with red frames identify the qubits pairs that will be entangled with the two-qubit gate (CNOT in our case).

7.3 Computational details

7.3.1 Tested Systems

The classical part involved in our algorithm is retrieved from the PySCF python package [72], while the MP2 wavefunctions are obtained by an adaptation of the MolCAst package.[143] The percentage of correlation energy E_c is defined as

$$E_c = \frac{E_{HF} - E_X}{E_{ex,c}} \qquad with \quad E_{ex,c} = E_{HF} - E_{FCI} \tag{7.4}$$

Where E_x is the energy obtained from the variational calculation and E_{HF} and E_{FCI} are the Hartree-Fock and full configuration interaction energy. The core software used for quantum computing simulation is the Python package Qiskit.[73] The Jordan-Wigner [23] encoding method has been considered in each simulation to map the fermionic system on a qubit register. In table 7.1 we list the data corresponding to the molecules under investigation.

7.3.2 Ansätze construction

We explained in subsection 7.2.3 how we find a parent sequence of CNOTs to be applied as an ansatz on the quantum circuit. Anyway, given the factorial scaling of possible orderings, for parent sequences longer than 6 CNOTs the analysis has been taken on a restricted random selection of orderings. For the randomly chosen ansätze, given the convention in the field of preferring top-down entanglement, we preferred a uniform distribution for the qubits

Mol.	Coordinates (Å)	Qubits	$E_{ex,c(\frac{Kcal}{mol})}$	μ	#
H_2	H 0.0 0.0 0.0 H 0.0 0.0 0.74	8	15.636	0.5	6
LiH	Li 0.0 0.0 0.0 H 0.0 0.0 1.595	10	12.6446	0.5	6
H_2O	O 0.0 0.0 0.0 H 0.757 0.586 0.0 H -0.757 0.586 0.0	12	31.006	0.5 0.7 0.5 *red.*	12 9 6
NH_3	N 0.0 0.0 0.1211 H 0.0 0.9306 -0.2826 H 0.8059 -0.4653 -0.2826 H -0.8059 -0.4653 -0.2826	14	41.287	0.5 *red.*	9

Table 7.1: Summary of data of the systems under analysis and computational details. H_2 has been analyzed with 631-G basis while every other molecule used STO-3G basis set and frozen core approximation. Last column show the number of elements in each parent sequence.

to be the target of a CNOT. We could have preferred a uniform distribution of the possible top-down CNOTs but this choice shows a bias toward the latter qubits (qubit i could receive i possible CNOTs with counting starting from 0). After every application of the chosen entangling block, we apply a $R_Y(\theta)$ quantum gate on every qubit. These two sections of the circuit together are referred to as *block* and with the term *depth* we refer to the number of blocks in use in the ansatz. To show the advantage of our QMI-aided ansatz over the ladder-entangler one, we analyze the results at different depths maintaining the same entangling blocks, with the secondary scope of looking if, for a specific depth, the advantage decreases. Such a result is foreseeable as the restricted entangling block suggested by our algorithm it is not even guaranteed to connect all the qubits, and indeed it does not happen in the analyzed cases. Net of pathological examples, it is then reasonable that a more expensive ladder-entangler block that links all the qubits will generally outperform our approach with the growth of the depth.

Table 7.1 show the values of the μ parameters investigated and the corresponding parent sequences. As regards the choice of the μ parameter, since the systems under analysis are not yet big enough to show a clearly diminishing number of CNOTs as a function of μ, we only consider one value for each system. An exception is made for H_2O molecule, for which we consider the two values 0.5 and 0.7. An example of ansatz construction for the H_2O molecule is given by figure 7.5. It has been obtained by choosing one of the

permutations of the parent sequence generated by setting $\mu = 0.5$ and taking into account the empirical reduction. For all the following plots we performed analysis on 100 different possible permutations of the original parent sequence.

Even for the random maps, we performed analysis on 100 of them. In both cases, we performed 50 VQE runs for each entangling block with random starting parameters to guarantee sufficient statistical value for a single kind of ansatz. An exception is made for the ladder-entangler block, which has been given 300 VQE since it represents the reference entangling block for comparison [1].

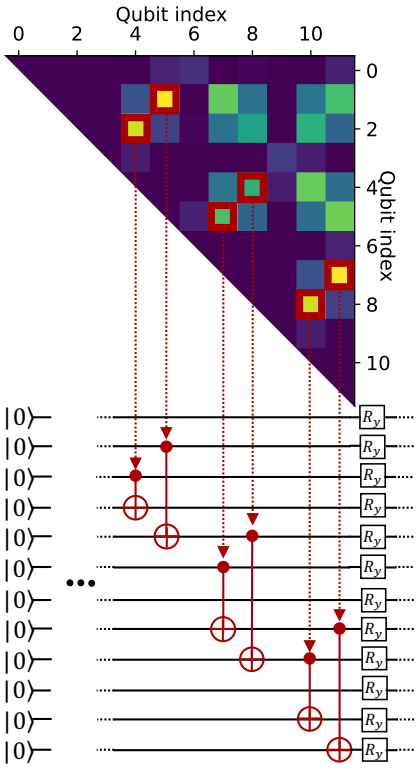

Figure 7.5: Pictorial representation of the method for H_2O molecule. Here empirical reduction has been applied to the parent sequence obtained by $\mu = 0.5$. The chosen permutation is clearly for illustrative purposes.

7.4 Results

In this section, we will show the results obtained by applying the method described above to the systems in table 7.1. First of all, we notice that the choice of the NO explained in section 7.2.2 is a favourable one to increase the sparsity of the I matrix, i.e. reduce the number of qubits pair with significant values of the QMI as more as possible. This concept is illustrated in figure 7.1: for each molecule under investigation, we have two maps corresponding to the FCI state expressed in the HFO and NO, respectively the one on the left and the one in the centre. It is clear that the choice of the NO increase the sparsity of the QMI matrix and this makes the ansatz construction easier. By comparing the images on the centre with the one right, the same figure

[1] Further exception for depth 4 of the ladder-entangler ansatz of the water molecule, in this case, we did 2000 repetitions to give more statistical value to figure 7.9

shows the close proximity of the QMI matrices obtained from the FCI and the MP2 states expressed in NO (also claimed in [139]), giving consistency to the choice of MP2 state as starting point for our ansätze. As regards the impact of different orderings of the parent sequence, we analyze their difference in performance with figure 7.6 that shows the results for the H_2O molecule. We set $\mu = 0.5$ and, from the parent sequence, 100 different entangler maps have been generated. Each of them gives rise to an ansatz once the depth is set at 2 and they are reported on the horizontal axis of figure 7.6. For each ansatz, we performed 50 VQEs run and reported, on the left vertical axis, the maximal value of the percentage of the correlation energy that has been obtained. The right vertical axis gives the probability that the energy of one of the 50 VQEs lies within 30% of the maximum, the value shown on the left vertical axis. Note that the clustering on the basis of vertical left axes value and orders are not meaningful of any intrinsic property and were dictated to facilitate the pairing of respective black and red spots. Here we see that, as expected, some entangling maps perform statistically better than others. We notice

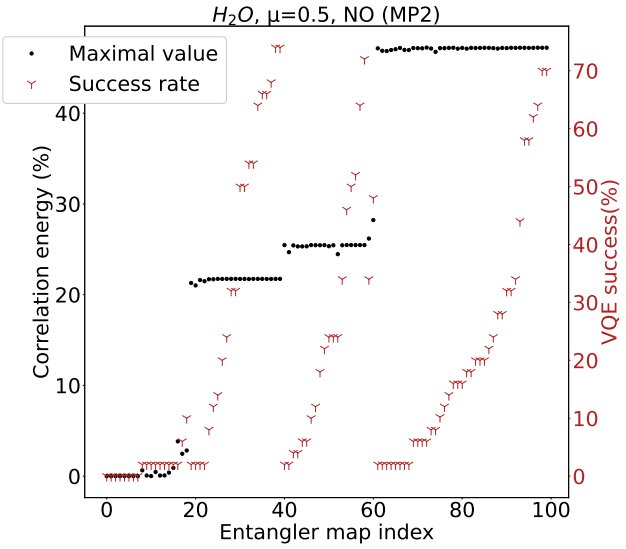

Figure 7.6: Multiple VQEs experiments for H_2O molecule with different ordering of the same parent sequence corresponding to $\mu = 0.5$. Depth is equal to 2 for each ansatz generated by an entangler map. 50 VQEs run are performed for each ansatz and the left vertical axis shows the maximum value of the % of the correlation energy while the right axes (red) represent the percentage of those 50 VQEs that are within 30% of their respective maximum (black spot).

that figure 7.7 is obtained by taking multiple statistical sets that in figure

7.6 are represented in one figure and transposing them over a single column, with this procedure being repeated for all the depths and ansätze shown. In this manner, we effectively represent the probability distribution one would sample from using the QIDA method with the steps described by figure 7.2. Figure 7.7 gives us the opportunity to statistically characterize the quality of the results obtained from different parent sequences. For H_2, LiH, H_2O molecules, we considered one or more different values for the μ parameter that gives rise to parent sequences, as reported in table 7.1 that also illustrate if the reduction explained in 7.2.3 has been taken into account. For each parent sequence, we extract 100 random entangling blocks, as described in the subsection 7.3.2. These blocks are repeated to define ansätze with depths ranging from 1 to 4 and the corresponding VQE results are reported by the violins referred to as QIDA in figure 7.7. The different kinds of QIDA ansätze are compared with the violins obtained from the random ansätze (details in subsection 7.3.2) and the ladder-entangler one over depths ranging from 1 to 4. Analyzing the depth, we see that there is a plateau for the maximal E_c retrieved. Furthermore, we see that right from depth 1 we spread within the whole interval of the reachable values, with an expected E_c greater than the one of the ladder-entangler ansatz at depth 4. Furthermore, we note that the maximal value of the percentage of the correlation energy is obtained by the ladder-entangler ansatz for depths equal to or bigger than 3, for H_2 molecule, and 4, for LiH and H_2O molecules. By comparing the mean values and the dispersion of the results around it, we see that QIDA ansätze assure that the probability to obtain better approximations of the FCI state is increased. The rationale behind these results, and thus the explanation for the success of our method, lies in the multiconfigurational nature of the wavefunction that the VQE is aimed at finding. As the ladder-entangler ansatz does not include anything about the specific problem for which is being used, nor is based on any chemically motivated background, the resulting ansatz, for the molecular system under investigation, will not necessarily be aimed at finding the determinants with higher modulus square of the amplitudes. On the contrary, the imposition of correlation where suggested by the approximated groundstate through the QMI will partially direct the optimization over the space with the expected correlation between qubits, rendering the optimization process easier for the optimizer. The diversity in the outcome can be justified by a wrong ordering of the entangling ansatz with respect to an ideal one. In this regard, for H_2O molecule, the only system for which we analyzed different values of μ, we saw no evidence of any substantial advantage in decreasing the value of μ from 0.7 to 0.5 besides a light decrease in expected E_c value. We explain this by considering that since passing from the former to the latter only adds the three CNOTs between qubits pair 2-8,

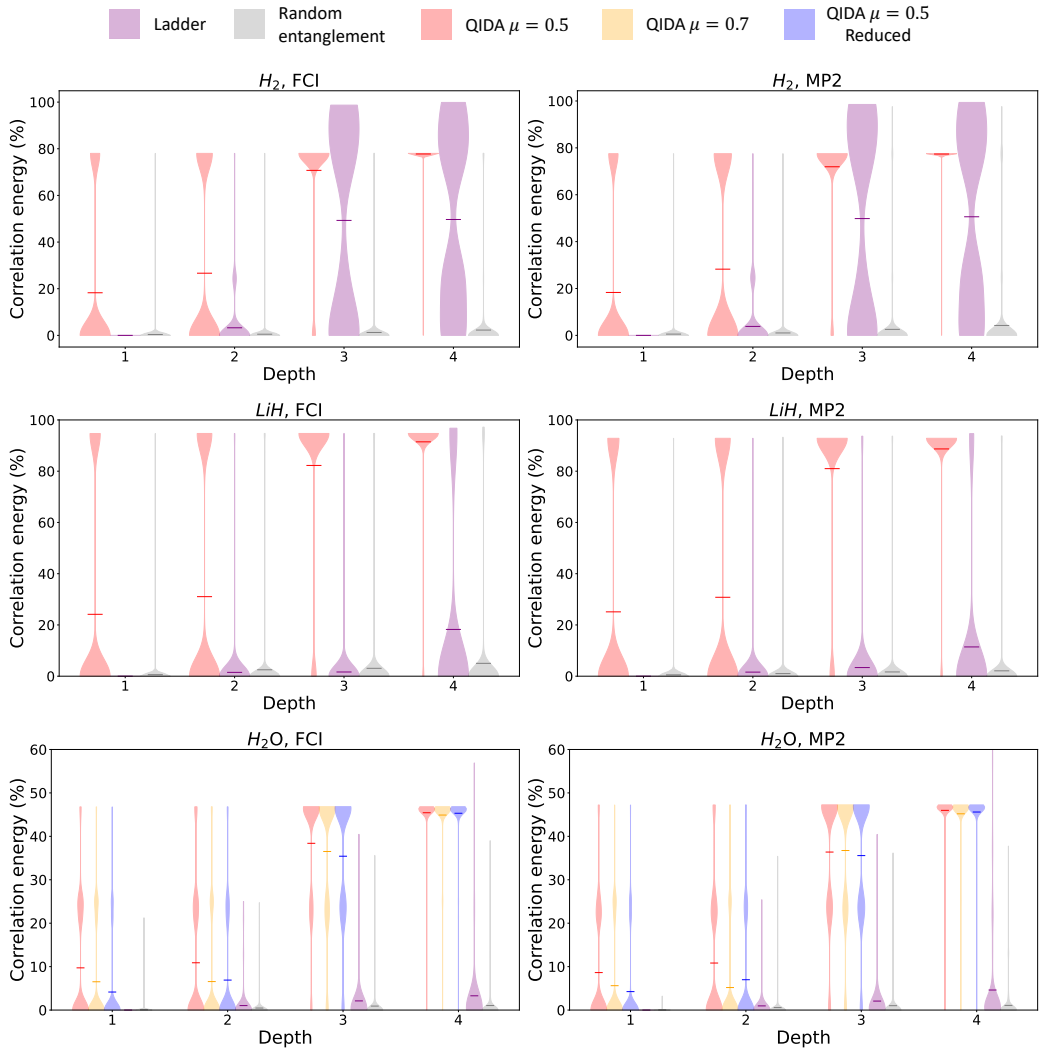

Figure 7.7: Average performance of our ansätze compared to the ladder-entangler ansatz and random ones. Each violin column corresponding to a QIDA ansatz represents the total distribution of the energy results obtained by executing 50 VQEs run for each block considered belonging to a parent sequence. For the ladder-entangler ansatz, the VQE algorithm has been repeated 300 times. The violins are all normalized only between themselves to satisfy the maximal allowed width.

2-10, 4-8 and, by what is explained in 7.2.3, those CNOTs can be considered redundant by the cross-entanglement analysis of the H_2O molecule (figure 7.1i).

Every result shown up to now serves as proof of the expected performance of the QIDA method. The rationale behind this was simply to give a statistical analysis as extensive as possible to describe the effectiveness of the method described in this work. In figure 7.8 we reported the energy results obtained by applying the method illustrated in figure 7.2 to the NH_3 molecule to compare the outcomes of the VQEs of our scheme with the ones corresponding to the ladder-entangler map. Thus, for this specific case, we tested our method by repeating 10 VQE for 18 different permutations of the parent sequence, while for the ladder entangling maps we performed 100 VQEs. Figure 7.8 shows then an indisputable advantage for both the maximal value and statistical distribution of the converged VQEs energies. Furthermore, given the CNOTs connectivity of the ansatz, we achieve this with a reduction in the number of CNOTs from 52 of the ladder-entangler ansatz to 36 of our method. Finally, the trend showed by the molecules in figure 7.7 suggests that the distribution of the reduced QIDA ansatz in figure 7.8 has already reached a plateau corresponding to the maximal value. Furthermore, net of statistical bias, it shows that the ladder-entangler ansatz is still far away from finding even a fraction of the percentage of the correlation energy. The previously discussed reduction of the number of needed CNOTs is also relevant for figure 7.7. For example, looking at figure 7.7[f], the reduced QIDA ansatz at depth 2 and the ladder-entangler ansatz at depth 4 have comparable statistical distributions of the energy results, with the former method having only 12 CNOTs against the 44 CNOTs of the latter method. Moreover, these distributions have been

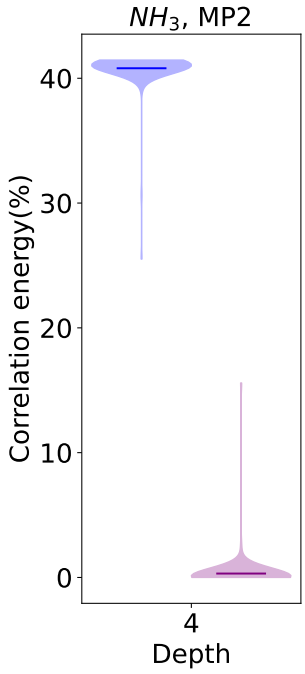

Figure 7.8: Statistical comparison of ladder-entangler ansatz (purple) with 100 repetitions and QIDA with 200 total VQEs run(Blue).

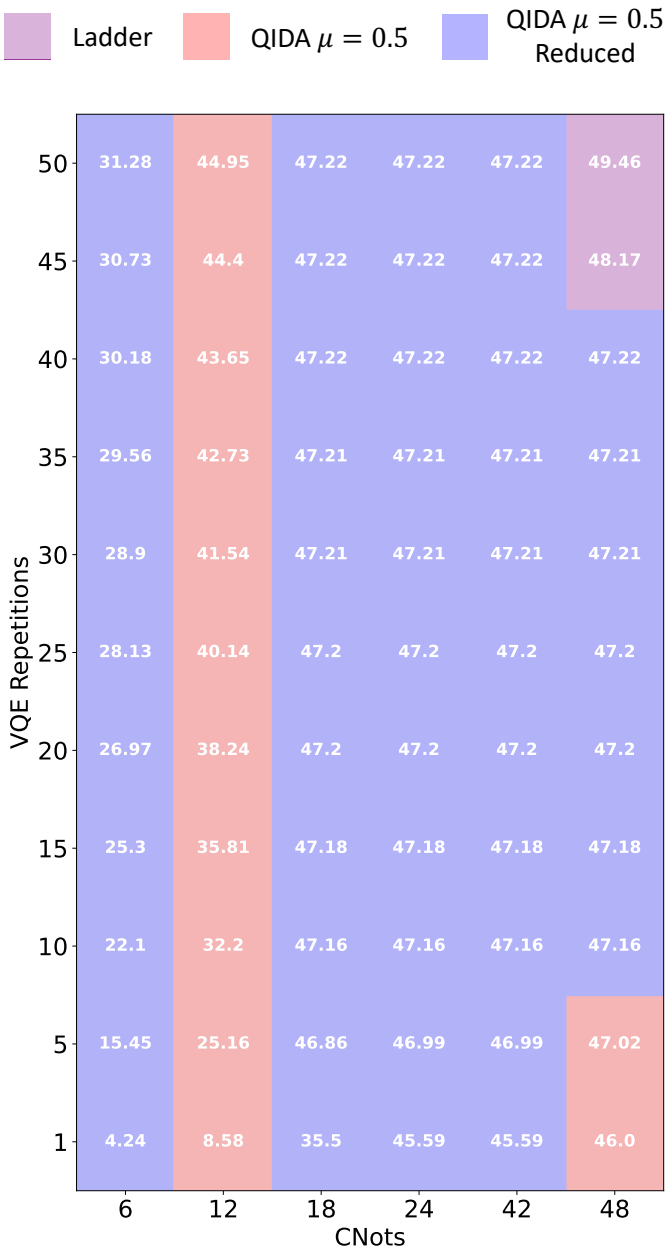

Figure 7.9: Resources analysis of best performing ansatz given resources (x,y). The shown numerical values are the expectation values of the maximum of y VQE repetitions with an ansatz possessing no more than x CNOTs. The colour of each spot is the one corresponding to the parent sequence that gives the highest results. The system under consideration is the H_2O molecule.

obtained by repeating the VQE experiments many times. In terms of computational cost, the CNOTs and the number of VQE experiments can be seen as quantum resources, respectively x and y, and we want to investigate the relation between the energy results and these variables. Given a certain parent sequence σ, we introduce the quantity $\epsilon_{\sigma,\delta,i}$ that is the energy obtained at the $i-th$ VQE experiment by the ansatz composed of δ repetitions of σ, the sequence under investigation. Moreover, we introduce the function

$$f_\sigma(x) = max(\delta) \quad s.t. \quad CNOT(\sigma) * \delta \leq x \tag{7.5}$$

which, fixed a sequence, finds the maximal number of repetitions that give rise to an ansatz such that the number of CNOTs is less or equal to x. Here, $CNOT(\sigma)$ give the number of CNOTs corresponding to the sequence under consideration. Finally, for each sequence σ, we define the function

$$E_\sigma(x,y) = \langle max_{k=1}^{y} max_{\delta=1}^{f_\sigma(x)}(\epsilon_{\sigma,\delta,k})\rangle \tag{7.6}$$

that gives the expectation value of the maximal percentage of the correlation energy for each value of the computational resources (x, y) introduced above. As expected, for each pair (x, y) the function 7.6 assumes different values by varying σ and the maximal one is reported in figure 7.9. The associated spot has the colour of the corresponding σ, defined in figure 7.7. The advantage of QIDA is noticeable in the overall results with respect to the ladder-entangler ansatz, particularly when the reduction is taken into account. Nevertheless, when the number of CNOTs and VQE repetitions is increased, the ladder-entangler ansatz statistically gives better results but without increasing significantly the ones obtained with our method. This is not surprising because, as mentioned above, the former connects all the qubits and possesses more parameters giving the possibility to catch electronic correlations that the latter cannot reproduce even if the depth of the circuit is increased. However, if noise is to be taken into account, we infer that the ladder-entangler ansatz will likely degrade any such advantage owned in the noiseless case because of the greater number of CNOTs gates with respect to QIDA ansatz. Overall, these results bring forward the idea of the QIDA ansatz as a modular starting circuit for a more refined fully entangled one that can catch the missing correlations, as was proposed at the beginning of this chapter.

7.5 Conclusions

We have presented a novel approach to constructing correlations inspired hardware efficient ansätze for quantum chemistry simulations. Our method

leverages the wavefunction of a well-scaling classical method, such as MP2, to generate ansätze that achieves correlation energies comparable or superior to currently used heuristic ansätze, while requiring substantially fewer CNOTs.

To demonstrate the effectiveness of our approach, we simulated various molecular systems using statevector simulations. We stressed the fact that the results in figure 7.9 have been obtained with statevector simulations. Then, for noisy simulations, we expect that QIDA ansätze will become even more efficient with respect to the ladder-entangler one because the number of two-qubit quantum gates is significantly reduced. Additionally, we observed a growing performance disparity with the number of qubits 7.8, with our QIDA method consistently demonstrating superior performance compared to the ladder-entangler ansatz.

Furthermore, we propose a modular approach to using QIDA in conjunction with other blocks to obtain a refinement of the method and recover the missing correlations. The idea is to first employ QIDA to identify the leading correlations between qubits in order to deliver to the optimized ansätze with appropriate starting ingredients, excluding from the Hilbert space the subspace involving entanglement between uncorrelated qubits. This constraint can be relaxed by applying subsequent fully entangled blocks. This approach has the potential to reduce the overall computational cost of quantum chemistry simulations while maintaining or improving the accuracy of the results.

In summary, this method is promising for generating hardware-efficient ansätze for quantum chemistry simulations. We have demonstrated the effectiveness of our QIDA method on the small molecules, increasing the percentage of the correlation energy values with fewer CNOTs compared to existing ansatz methods. These findings suggest that our QIDA can be a valuable tool in the ongoing efforts to improve the efficiency and accuracy of quantum chemistry simulations.

Chapter 8

Spin-symmetric ansätze

8.1 Introduction

Developing strategies to determine the groundstate of physical systems play a fundamental role in electronic structure calculation. Quantum algorithms could give an exponential speed-up in this field and the variational quantum algorithm (VQE) is one of the most promising algorithms for NISQ devices. The parameters of the hardware-efficient ansatz implemented for this algorithm span a subset of the Fock space to find the values that minimize the expectation value of the Hamiltonian of the system under consideration. There are no certainties that the groundstate is included in the spanned subset nor that classical optimisation can reach such state. Thus the definition of the variational form of the ansatz is a crucial point, even if the Hamiltonian is optimized, as shown in chapter 3. In the previous chapter 7, we illustrated a strategy that exploits the quantum mutual information between spin-orbitals of an approximated groundstate to determine the ansatz. Here, we show another method that takes advantage of a particular symmetry of the Hamiltonian.

8.2 Spin-inversion symmetry

We consider a set of n single-particle states and two spin projections. The 2^{2n} basis vectors of the Fock space are

$$|\alpha_{1\downarrow}\alpha_{1\uparrow}\dots\alpha_{n\downarrow}\alpha_{n\uparrow}\rangle = \prod_{i=1}^{n}(a_{i\downarrow}^{\dagger})^{\alpha_{i\downarrow}}(a_{i\uparrow}^{\dagger})^{\alpha_{i\uparrow}}\,|\varnothing\rangle \tag{8.1}$$

where $\alpha_{i\sigma} = 0, 1 \quad \forall i = 1, \ldots, n \quad \sigma = \uparrow, \downarrow$ and $|\varnothing\rangle$ is the vacuum state. Now define the spin-inversion operator

$$R = \prod_{i=1}^{n} R_i = \prod_{i=1}^{n} [a_{i\uparrow}^\dagger a_{i\downarrow} + a_{i\downarrow}^\dagger a_{i\uparrow} + (1 - N_i)^2] \tag{8.2}$$

where $N_i = a_{i\uparrow}^\dagger a_{i\uparrow} + a_{i\downarrow}^\dagger a_{i\downarrow}$ is the number operator for the mode i. It easy to show that

$$R_i = R_i^\dagger \qquad [R_i, R_j] = 0 \qquad R_i R_i = I \tag{8.3}$$

where I is the identity operator. As a consequence, the R operator is Hermitian and unitary

$$R = R^\dagger \qquad R R^\dagger = I \tag{8.4}$$

From these properties, it follows that

$$R^\dagger a_{l\sigma}^\dagger R = R a_{l\sigma}^\dagger R = a_{l\bar{\sigma}}^\dagger (1 - 2N_{l\sigma}) \tag{8.5}$$

where $\bar{\sigma}$ is the spin-projection opposite with respect to σ and $N_{l\sigma} = a_{l\sigma}^\dagger a_{l\sigma}$. By applying the R operator to the basis states 8.1 and considering the relation above we see that

$$R \, |\alpha_{n\downarrow} \alpha_{n\uparrow} \ldots \alpha_{1\downarrow} \alpha_{1\uparrow}\rangle = |\alpha_{n\uparrow} \alpha_{n\downarrow} \ldots \alpha_{1\uparrow} \alpha_{1\downarrow}\rangle \tag{8.6}$$

When acting on a state, the first two terms in each R_l exchange the spin of the particles if there is only one in the mode l while annihilating the state if the mode is empty or doubly occupied, the last term act as an identity operator if the mode l is empty or doubly occupied and annihilate the state if it is individually occupied. The phase factor into the parenthesis of the equation 8.5 takes into account the -1 sign appearing when the particles in the doubly occupied state are exchanged. Thus R exchanges the occupation numbers of the spin-up and spin-down projections of each single-particle mode, this explains the name given to the operator. Consider a system such that

$$\langle \psi_a | \, H \, | \psi_b \rangle = \langle R\psi_a | \, H \, | R\psi_b \rangle \qquad \forall a, b \in 2^{2n} \tag{8.7}$$

where a, b are the indices corresponding to the vectors of the Fock space. In this case, we obtain that $H = R^\dagger H R = RHR$ because R is Hermitian, so the two operators commute

$$[R, H] = 0 \tag{8.8}$$

Suppose that the groundstate $|\psi_{GS}\rangle$ of our system is non-degenerate. Since R is unitary, as a consequence of the previous equation, we have that

$$R \, |\psi_{GS}\rangle = |\psi_{GS}\rangle \tag{8.9}$$

We can take advantage of this equivalence by modifying the cost function of the variational quantum algorithms like VQE and WAHTOR. Consider the parametrized ansatz $|\psi(\boldsymbol{\theta})\rangle$, the state $R|\psi(\boldsymbol{\theta})\rangle$ is pure as well as $|\psi(\boldsymbol{\theta})\rangle$ because R is unitary. The root fidelity [144] $F(\boldsymbol{\theta})$ between these two states is

$$F(\boldsymbol{\theta}) = |\langle\psi(\boldsymbol{\theta})| R |\psi(\boldsymbol{\theta})\rangle| \tag{8.10}$$

and can efficiently be calculated on a quantum computer because R is Hermitian and the number of Pauli strings appearing in the mapped operator scale as $O(n)$. Since $F(\boldsymbol{\theta}) = 1$ if and only if $R|\psi(\boldsymbol{\theta})\rangle = |\psi(\boldsymbol{\theta})\rangle$, we can define the following cost function

$$C(\boldsymbol{\theta}) = \langle\psi(\boldsymbol{\theta})| H |\psi(\boldsymbol{\theta})\rangle + \lambda(1 - F(\boldsymbol{\theta})) \tag{8.11}$$

where λ is a real positive parameter. Since the additional term in the cost function $C(\boldsymbol{\theta})$, during the classical optimization of the $\boldsymbol{\theta}$ parameters the optimizer tends to explore the subset of the Hilbert space corresponding to states that are invariant under the application of the R operator, the symmetry possesses by the $|\psi_{GS}\rangle$. Another way to take advantage of this symmetry is to build an ansätze that preserves it for each value of the parameters. Consider a state $|\psi\rangle$ that can be obtained by applying a set of N unitary operators $U_1, \ldots, U_M$ to the state $|\phi\rangle$

$$|\psi\rangle = U_M \ldots U_1 |\phi\rangle = RRU_M RR \ldots RRU_1 RR |\phi\rangle \tag{8.12}$$

where the last equality follows from the properties 8.4. If one defines the operators

$$\tilde{U}_i = RU_i R \qquad i = 1 \ldots M \tag{8.13}$$

the state above can be expressed as

$$|\psi\rangle = R\tilde{U}_M \ldots \tilde{U}_1 |\tilde{\phi}\rangle \tag{8.14}$$

where $|\tilde{\phi}\rangle = R|\phi\rangle$. Thus $|\psi\rangle$ can be obtained by applying the operators U_i to the initial wavefunction $|\phi\rangle$ or, equivalently, by considering the spin inversion of the initial wave function $|\tilde{\phi}\rangle$ followed by the application of the set of operators $\tilde{U}_i$ and another spin-inversion operator. If the single-particle states are represented with lines and the operators with black boxes acting on them, we can graphically illustrate with figure 8.1 the two ways to build $|\psi\rangle$. We aim to construct a state such that $|\psi\rangle = R|\psi\rangle$. Without loss of generality, we can consider an initialized state such that $|\phi\rangle = R|\phi\rangle$. Given a set of M unitary operators V_i, we obtain that $\tilde{V}_i = RV_iR$ for $i = 1, \ldots, M$. Suppose that these operators commute, thus

$$[\tilde{V}_i, V_i] = 0 \tag{8.15}$$

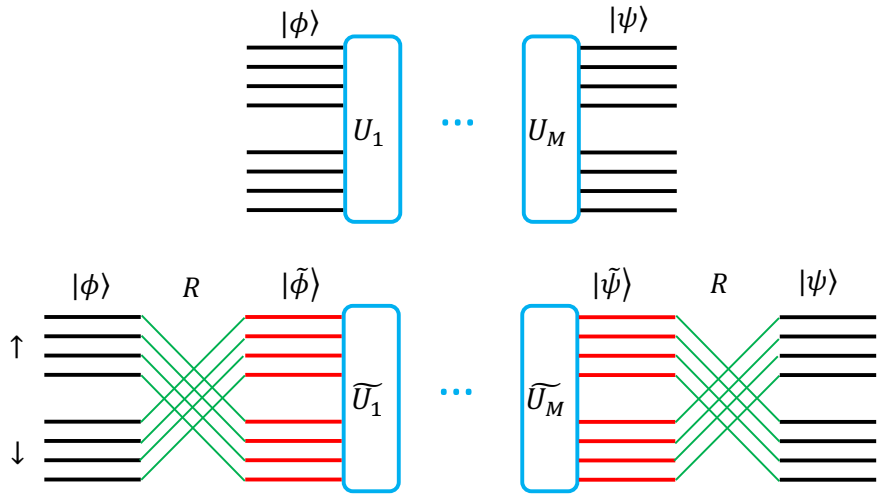

Figure 8.1: Illustration of the two different ways to build the state $|\psi\rangle$. Each line represents a single-particle state where the spin-up and spin-down are identified respectively with $\uparrow$ and $\downarrow$. The operators acting on them are depicted as black boxes.

We will see later that this condition can be verified for the cases of our interest. Now, we can define $U_i = V_i\tilde{V}_i$. It follows that

$$\tilde{U}_i = RV_i\tilde{V}_iR = RV_iRV_iRR = \tilde{V}_iV_i = V_i\tilde{V}_i = U_i \tag{8.16}$$

Finally, from the equation 8.14 we get

$$R\,|\psi\rangle = RR\tilde{U}_M \ldots \tilde{U}_1\,|\phi\rangle = U_M \ldots U_1\,|\phi\rangle = |\psi\rangle \tag{8.17}$$

that satisfy the required condition. In order to investigate how to implement a hardware-efficient ansatz that preserves this symmetry on a quantum computer, we need to define a set of quantum gates that can be implemented on our device. Our method can be applied to quantum gates that act on any number of qubits but, to perform an easy implementation, we just consider the $CNOT$ and the R_Y quantum gates acting, respectively, on two and one qubits. By taking into account the Jordan-Wigner encoding method, we can define the fermionic representation of the $CNOT$ quantum gate as

$$V^C = a_{i\sigma}a^\dagger_{i\sigma} + (a_{j\tau} + a^\dagger_{j\tau})a^\dagger_{i\sigma}a_{i\sigma} \prod_{\Gamma(k,\rho)<\Gamma(j,\tau)} (1 - 2N_{k\rho}) \tag{8.18}$$

where $i, j, k = 1, \ldots, N$ and $\sigma, \tau, \rho = \uparrow, \downarrow$. Here, $i\sigma$ and $j\tau$ specify the fermionic modes on which the CNOT acts. We introduced the function

$\Gamma(k,\rho) = 2k - \delta_{\rho\downarrow}$ to take into account the phase factor due to the occupied fermionic modes $k\rho$ that in formula 8.1 appear to the left of the mode $j\tau$. Suppose that $i \neq j$. By using the relation 8.5, the corresponding spin-inverted operator can be easily calculated

$$\tilde{V}^C = a_{i\bar{\sigma}}a^\dagger_{i\bar{\sigma}} + (a_{j\bar{\tau}} + a^\dagger_{j\bar{\tau}})a^\dagger_{i\bar{\sigma}}a_{i\bar{\sigma}}(1 - 2N_{j\tau}) \prod_{\Gamma(k,\rho)<\Gamma(j,\tau)} (1 - 2N_{k\bar{\rho}}) \tag{8.19}$$

and it follows that $[V^C, \tilde{V}^C] = 0$. In an equivalent way, we can define the fermionic operator associated with the quantum gate $R_Y(\theta)$, acting on single-particle quantum state $i\sigma$, as

$$V^{R_Y}(\theta) = \cos\frac{\theta}{2} + \sin\frac{\theta}{2}(a^\dagger_{i\sigma} - a_{i\sigma}) \prod_{\Gamma(k,\rho)<\Gamma(j,\tau)} (1 - 2N_{k\rho}) \tag{8.20}$$

where, for the phase factor, the same consideration explained above are still valid. We see that

$$\tilde{V}^{R_Y}(\theta) = \cos\frac{\theta}{2} + \sin\frac{\theta}{2}(a^\dagger_{i\bar{\sigma}} - a_{i\bar{\sigma}}) \prod_{\Gamma(k,\rho)<\Gamma(j,\tau)} (1 - 2N_{k\bar{\rho}}) \tag{8.21}$$

that give $[V^{R_Y}(\theta), \tilde{V}^{R_Y}(\theta)] = 0$. By defining

$$U^C = V^C\tilde{V}^C \qquad U^{R_Y}(\theta) = V^{R_Y}(\theta)\tilde{V}^{R_Y}(\theta) \tag{8.22}$$

and considering the initializing state $|0\rangle^{\otimes_N}$, we can construct the ansatz

$$|\psi\rangle = U^C_M U^{R_Y}(\theta_M) \ldots U^C_1 U^{R_Y}(\theta_1) |0\rangle^{\otimes_N} \tag{8.23}$$

that preserve the spin-symmetry for each value of the parameters θ_i. Here the subscripts going from 1 to M in each operator remind us that they can act on different qubits.

8.3 Results

To show the validity of the method described above, we build an example of an ansatz that preserves the spin-inversion symmetry and we discuss the results obtained for the benchmarking H_2O molecule. We define the two-qubit quantum gate V in the following manner: apply a CNOT gate followed by two R_y gates, one on the target qubit and the other one on the control qubit, as shown in figure 8.2. If V acts on qubits $i\sigma$ and $j\tau$ for $i \neq j$, $\tilde{V}$ acts on qubits $i\bar{\sigma}$ and $j\bar{\tau}$, it follows that the quantum gate $U = V\tilde{V}$ is applied

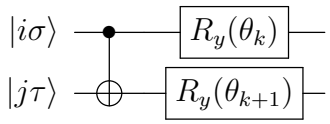

Figure 8.2: The quantum gate V, applied between the qubits $i\sigma$ and $j\tau$, that we defined to perform our simulations is shown.

on the four qubits that we specified with the representation $(i\sigma, j\tau, i\bar{\sigma}, j\bar{\tau})$. Here the first two indices are related to the gate V while the third and fourth are related to $\tilde{V}$. Consider the H_2O molecular system in sto-3g basis set. By applying the frozen core approximation we obtain a set of 6 orbitals, indexed from 0 to 5. With the Jordan-Wigner encoding method, we can map our system on a 12 qubits register, where the first half and the second half of qubits map the occupation number of respectively the spin-up and spin-down orbitals. We built the ansatz in the following manner: on each qubit $i\sigma$ we apply an $R_y(\theta_{i\sigma})$ quantum gate and constrain the parameters so that $R_y(\theta_{i\bar{\sigma}}) = R_y(\theta_{i\sigma})$, then an entanglement block composed only of U quantum gates is applied and repeated a number of times equal to the depth. To define an entanglement block we need to specify where the U gates are applied. We choose the following set of indices

$$
\begin{aligned}
U_1 &\to (1\uparrow, 5\uparrow, 1\downarrow, 5\downarrow) \\
U_2 &\to (2\uparrow, 4\downarrow, 2\downarrow, 4\downarrow) \\
U_3 &\to (5\uparrow, 1\downarrow, 5\downarrow, 1\uparrow) \\
U_4 &\to (4\uparrow, 2\downarrow, 4\downarrow, 2\uparrow) \\
U_5 &\to (0\uparrow, 4\uparrow, 0\downarrow, 4\downarrow) \\
U_6 &\to (4\uparrow, 1\downarrow, 4\downarrow, 1\uparrow)
\end{aligned}
$$

By setting the depth to 3 we obtain an ansatz composed of 36 CNOTs and 41 parameters. The ansatz parameters were optimized up to a convergence threshold of 10^{-6} Hartree. The VQE algorithm converges to 50.63% of the correlation energy, defined in chapter 3, and the corresponding root fidelity between this state and the groundstate is 0.99318. These results are comparable with the ones shown in chapter 5: the depth 4 ladder entangler, map composed of 44 CNOTs and 60 parameters, converged to 51.65% of the correlation energy with a root fidelity between this state and the groundstate equal to 0.99233. The spin-inversion symmetry of the converged state can

be pictorially shown by taking into account the quantum mutual information matrix (MI) defined in 7.2. Indeed, consider as an example the QMI

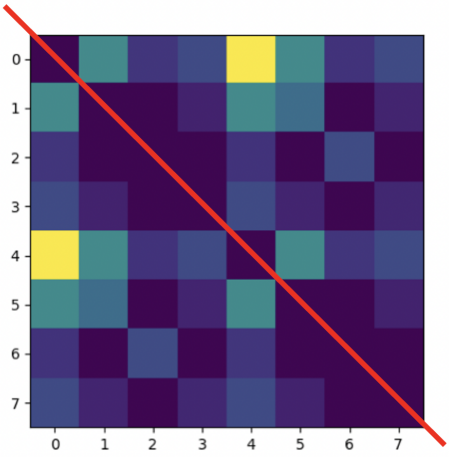

(a) MI matrix

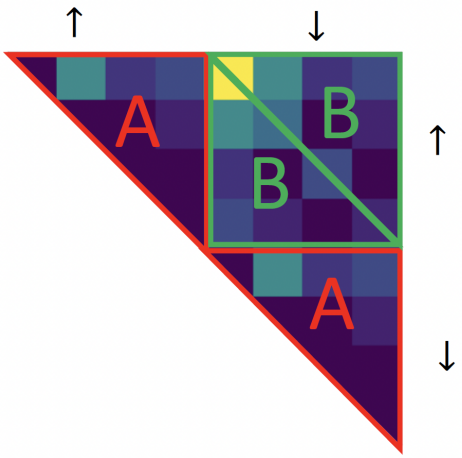

(b) Blocks

Figure 8.3: The MI is related to the H_2 system in HF basis. (a) The MI matrix is symmetric with respect to the diagonal by construction. (b) The spin-inversion symmetry divides the upper triangular part of the QMI into two couple of triangular blocks: the red blocks A and the green blocks B respectively corresponding to spin-orbital pairs with the same and the opposite spin projection.

matrix corresponding to the Jordan-Wigner mapped groundstate of the H_2

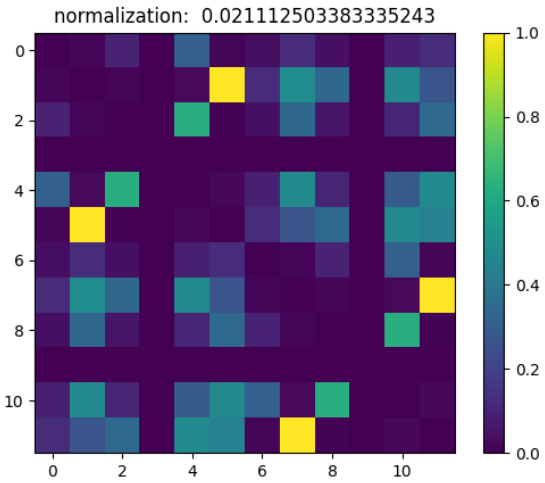

Figure 8.4: QMI matrix of the VQE state for the H_2O molecular system detailed in the main text.

molecule, expressed in Hatree-Fock spin-orbitals, shown in figure 8.3. Since this quantum system verifies the conditions set out in the previous section, we know that $R|\psi_{GS}\rangle = |\psi_{GS}\rangle$ and this equality is reflected on the QMI matrix. To explain this concept, we focus on the image 8.3[b] representing the upper triangular part of the QMI matrix. Here we identified two couple of triangular blocks that we called A and B. The upper A block defines the QMI between the spin-up orbitals and the lower one is related to the QMI between the spin-down orbitals. The B blocks take into account the QMI between spin-orbitals with opposite spin projections. In general, the four blocks defined above are different from each other. If the state under consideration possesses the spin-inversion symmetry, as done by $|\psi_{GS}\rangle$, the two A blocks are identical between them such as the B ones, as can be noted in figure 8.3[b]. Now we go back to the H_2O molecular system described above. In figure 8.4 we reported the QMI matrix corresponding to the converged VQE state. Since we constructed the ansatz in a spin-symmetric way, we note that the A and B blocks are equal as expected. For the VQE state obtained from the ladder ansatz with depth 4, the QMI matrix is shown in figure 5.2[a]. In this case, we note that nor the A blocks nor the B ones are identical because this ansatz does not preserve the spin-inversion symmetry.

Chapter 9

Conclusions and outlook

In this work, different approaches have been considered to improve the capabilities of the variational quantum algorithms. Exception made for the QIDA method, we tried to exploit the symmetries of the system under consideration to this scope. In chapters 3 and 4 we explained how to implement the orbital optimization procedure on a quantum computer by calculating the energy derivatives with respect to the Hamiltonian parameters that specify the single-particle basis set. Results showed that the algorithm improved the VQE energies and gave a certain flexibility in the ansatz connectivity, adapting the Hamiltonian to the wavefunction. In chapter 5 we showed that the WAHTOR algorithm converges to the natural orbital basis set for the benchmark molecular systems investigated. In chapter 6 the basis change is interpreted as a particular case of the Bogoliubov proper unitary transformation, thanks to the Hamiltonian can be written in terms of quasiparticles. This symmetry has been employed to study SU(N) Hubbard-type models. Despite the Hamiltonian optimization improving the VQE results for each system investigated the Bogoliubov transformation did not show any advantage with respect to the basis change. Further investigations are necessary to test the method before publishing the work: on the one hand, we want to simulate SU(4) models by optimizing the basis set, on the other hand, we will investigate the behaviour of the algorithm when the Bogoliubov transformation is taken into account for Hamiltonians containing superconductive terms, like for the Kitaev models. In chapter 7 we focused on the building of heuristic ansätze containing the potential to create the correlations characterising the chemical systems investigated. In particular, we developed a strategy that determines the quantum mutual information between the spin-orbitals of an approximated groundstate obtained from classical methods and, based on this information, built the entangler block. The results show that the VQE energies obtained with QIDA possess better statistical properties than

the ones obtained from the ladder ansatz. This is particularly evident for the NH_3 molecule, the bigger tested system. Given the promising results, the method could be further developed by considering quantum gates different from the CNOTs to entangle the qubits. Moreover, since the method concentrates the strongest correlations on a small number of CNOTs gates, it can be used as a starting point to build a more accurate ansatz. In chapter 8, we defined a strategy to build ansätze that preserves the spin-inversion symmetry. As proof of concept, we limited the test to a specific ansatz, thus further investigations are required to implement other quantum circuits.

The manuscripts related to the results shown in chapters 5 and 7 are in preparation while the ones related to the results exposed in chapters 4 and 3 are respectively under review [145] and published [103].

All these methods have been tested using state vector simulations. Despite we expect that the statistical noise in measurement-based simulations will not invalidate the methods developed in this work, we showed in figure 3.11 that noisy hardware is not yet able to reproduce physically significant results when the VQE algorithm is run. Thus further progress is necessary to reduce the noise of real quantum hardware and allow the use of the methods, based on the VQE algorithm, that we developed. The ideas developed in chapters 7 and 8 give rise to ansatz that naturally incorporates some property of the investigated system, like correlations or symmetry and, in this sense, they differ from the random hardware efficient ansatz that suffers the problem of the barren plateau [42]. Thus it will be interesting to investigate if this limitation is present in the proposed quantum circuits.

Finally, up to now, all the methods illustrated in this work have been developed independently from each other. In principle, they could be mixed to open the way to a new future prospective. For example, given an approximate state of the problem under investigation, we could build an ansatz using the QIDA method by considering a spin-inversion symmetric entangler in place of the CNOTs. Moreover, the Hamiltonian can be optimised using one of the transformations discussed in this work.

Chapter 10

Appendix

In this appendix, we give additional information about the results illustrated above. In particular, in the first section, we give proof of the equations used to calculate the derivatives of the one-body and two-body integrals with respect to the Hamiltonian parameters shown in chapter 4. in the second one, we show the quantum mutual information matrices obtained for the molecules investigated in chapter 5.

10.1 Derivatives

We start defining the vector $\boldsymbol{R} \in \mathbb{R}^{d^2}$ and the vector $\boldsymbol{T}$ of the generators of the Hermitian matrices of dimension d^2. The equation of the n-th derivative of the energy with respect to the variables with indices $l_1, l_2, ..., l_n$ is

$$\begin{aligned}\frac{d^n E(\boldsymbol{R},\boldsymbol{\theta})}{dR_{l_1},..,dR_{l_n}} = \sum_{i,j} \frac{d^n h(\boldsymbol{R})_{ij}}{dR_{l_1},..,dR_{l_n}} \langle\Psi(\boldsymbol{\theta})|\, a_i^\dagger a_j \,|\Psi(\boldsymbol{\theta})\rangle + \\ +\frac{1}{2}\sum_{c,d,e,f} \frac{d^n g(\boldsymbol{R})_{cdef}}{dR_{l_1},..,dR_{l_n}} \langle\Psi(\boldsymbol{\theta})|\, a_c^\dagger a_d^\dagger a_e a_f \,|\Psi(\boldsymbol{\theta})\rangle\end{aligned} \tag{10.1}$$

We note that to calculate the derivatives of each order of the energy with respect to the Hamiltonian parameters, we just need to calculate the derivatives of the one-body and two-body integrals

$$h(\boldsymbol{R}) = e^{-i\boldsymbol{R}\cdot\boldsymbol{T}} h_{HF} e^{i\boldsymbol{R}\cdot\boldsymbol{T}} \tag{10.2}$$

and

$$g(\boldsymbol{R}) = e^{-i\boldsymbol{R}\cdot\boldsymbol{T}} \otimes e^{-i\boldsymbol{R}\cdot\boldsymbol{T}} g_{HF} e^{i\boldsymbol{R}\cdot\boldsymbol{T}} \otimes e^{i\boldsymbol{R}\cdot\boldsymbol{T}} \tag{10.3}$$

where h_{HF} and g_{HF} are the one and the two body integrals expressed in Hartree-Fock basis, respectively. For this purpose, we can use the following

lemma of the Baker–Campbell–Hausdorff formula

$$e^{A}oe^{-A} = \sum_{k=0}^{\infty} \frac{[(A)^k, o]}{k!} \tag{10.4}$$

where $[(A)^k, o] = \underbrace{[A, .., [A[A,}_{\text{k times}} o]]...]$ is the iterated commutator for the two operators A and o, that can be written as

$$[(A)^k, o] = \sum_{B^k = Perm\{A^k\}} [B_1^k, [B_2^k, [B_3^k, ..., [B_k^k, o]...]]] \tag{10.5}$$

where B^k is a set composed of k objects that, in this case, are the same operator A repeated k times. Now suppose that A is linear in $\boldsymbol{R}$, so, defining $e^{A(\boldsymbol{R})}oe^{-A(\boldsymbol{R})} = o(\boldsymbol{R})$ it easy to show that

$$\frac{d^n o(\boldsymbol{R})}{dR_{l_1}, .., dR_{l_n}} = \sum_{k=0, n\leq k}^{\infty} \sum_{B^k} \frac{1}{k!} [B_1^k, [B_2^k, [B_3^k, ..., [B_k^k, o]...]]] \tag{10.6}$$

where

$$B^k = Perm\{A^{k-n}, \frac{dA}{dR_{l_1}}, .., \frac{dA}{dR_{l_n}}\} \tag{10.7}$$

The derivatives are easy to evaluate in $\boldsymbol{R} = \boldsymbol{0}$ because, in this case, just the term with $k = n$ survive in the summation

$$\frac{d^n o(\boldsymbol{R})}{dR_{l_1}, .., dR_{l_n}}|_{\boldsymbol{R}=\boldsymbol{0}} = \sum_{B^n} \frac{1}{n!} [B_1^n, [B_2^n, [B_3^n, ..., [B_n^n, o]...]]] \tag{10.8}$$

with

$$B^n = Perm\{\frac{dA}{dR_{l_1}}, .., \frac{dA}{dR_{l_n}}\} \tag{10.9}$$

This equation can be written recursively as

$$\frac{d^n o(\boldsymbol{R})}{dR_{l_1}, .., dR_{l_n}}|_{\boldsymbol{R}=\boldsymbol{0}} = \sum_{j=Perm\{l\}} \frac{1}{n} \left[\frac{dA}{dR_{j_1}}, \frac{d^{n-1} o(\boldsymbol{R})}{dR_{j_2}, .., dR_{j_n}}|_{\boldsymbol{R}=\boldsymbol{0}} \right] \tag{10.10}$$

For the one body term, we have that $A = -i\boldsymbol{R}\cdot\boldsymbol{T}$ and $o = h_{HF}$, so

$$\frac{d^n h(\boldsymbol{R})}{dR_{l_1}, .., dR_{l_n}}|_{\boldsymbol{R}=\boldsymbol{0}} = \sum_{j=Perm\{l\}} \frac{1}{n} \left[-iT_{j_1}, \frac{d^{n-1} h(\boldsymbol{R})}{dR_{j_2}, .., dR_{j_n}}|_{\boldsymbol{R}=\boldsymbol{0}} \right] \tag{10.11}$$

For the two body term, we observe that

$$e^{i\boldsymbol{R}\cdot\boldsymbol{T}} \otimes e^{i\boldsymbol{R}\cdot\boldsymbol{T}} = (e^{i\boldsymbol{R}\cdot\boldsymbol{T}} \otimes I)(I \otimes e^{i\boldsymbol{R}\cdot\boldsymbol{T}}) = e^{i\boldsymbol{R}\cdot\boldsymbol{T}\otimes I} e^{I\otimes i\boldsymbol{R}\cdot\boldsymbol{T}} = e^{(i\boldsymbol{R}\cdot\boldsymbol{T}\otimes I + I\otimes i\boldsymbol{R}\cdot\boldsymbol{T})} \tag{10.12}$$

where I is the identity operator and the last equality is true because of the Baker–Campbell–Hausdorff formula for commutating operators. So we can write the two body integrals in the following manner

$$g(\boldsymbol{R}) = e^{(-i\boldsymbol{R}\cdot\boldsymbol{T}\otimes I - I\otimes i\boldsymbol{R}\cdot\boldsymbol{T})} g_{HF} e^{(i\boldsymbol{R}\cdot\boldsymbol{T}\otimes I + I\otimes i\boldsymbol{R}\cdot\boldsymbol{T})} \tag{10.13}$$

Now, using the equation 10.10 and imposing $A = -i\boldsymbol{R}\cdot\boldsymbol{T} \otimes I - I \otimes i\boldsymbol{R}\cdot\boldsymbol{T}$ and $o = h_{HF}$, we obtain a formula similar to that shown for the one body term

$$\frac{d^n g(\boldsymbol{R})}{dR_{l_1}, .., dR_{l_n}}|_{\boldsymbol{R}=\boldsymbol{0}} = \sum_{j=Perm\{l\}} \frac{1}{n}\left[-i(T_{j_1}\otimes I + I\otimes T_{j_1}), \frac{d^{n-1} g(\boldsymbol{R})}{dR_{j_2}, .., dR_{j_n}}|_{\boldsymbol{R}=\boldsymbol{0}}\right] \tag{10.14}$$

Finally, we obtain the first derivatives

$$\begin{aligned} \frac{dh(\boldsymbol{R})}{dR_l}|_{\boldsymbol{R}=\boldsymbol{0}} &= -i[T_l, h_{HF}] \\ \frac{dg(\boldsymbol{R})}{dR_l}|_{\boldsymbol{R}=\boldsymbol{0}} &= -i[T_l\otimes I + I\otimes T_l, g_{HF}] \end{aligned} \tag{10.15}$$

and the second ones

$$\begin{aligned} &\frac{d^2 h(\boldsymbol{R})}{dR_{l_1} dR_{l_2}}|_{\boldsymbol{R}=\boldsymbol{0}} = -\frac{1}{2}([T_{l_1}, [T_{l_2}, h_{HF}]] + [T_{l_2}, [T_{l_1}, h_{HF}]]) \\ &\frac{d^2 g(\boldsymbol{R})}{dR_{l_1} dR_{l_2}}|_{\boldsymbol{R}=\boldsymbol{0}} = -\frac{1}{2}([T_{l_1}\otimes I + I\otimes T_{l_1}, [T_{l_2}\otimes I + I\otimes T_{l_2}, g_{HF}]] + \\ &+ [T_{l_2}\otimes I + I\otimes T_{l_2}, [T_{l_1}\otimes I + I\otimes T_{l_1}, g_{HF}]]) \end{aligned} \tag{10.16}$$

10.2 Quantum mutual information matrices

In the present section, we provide the quantum mutual information maps for the other molecules considered in chapter 5. For each figure, we have the VQE state (a), the WAHTOR state (b) and the ground state (c,d,e). The first one is expressed in the HF basis, the second one in the converged molecular basis and the third one in three different basis sets: Hartree-Fock, converged and natural orbitals set. For each molecule, we note that the quantum mutual information in the WAHTOR state is distributed on the qubit pairs as well as in the ground state expressed in the natural orbital basis. As more the converged state is similar to the ground state as more the quantum mutual information maps are similar.

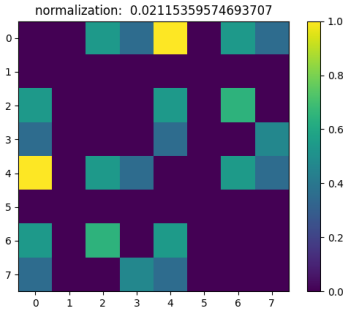

(a) VQE state in HF molecular orbitals

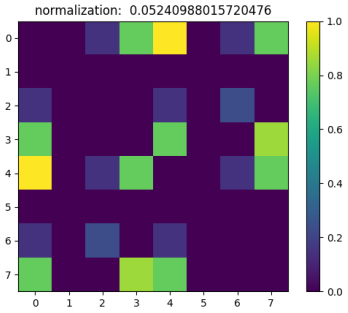

(b) WAHTOR state in converged molecular orbitals

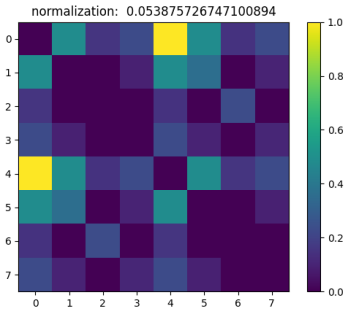

(c) Groundstate in HF molecular orbitals

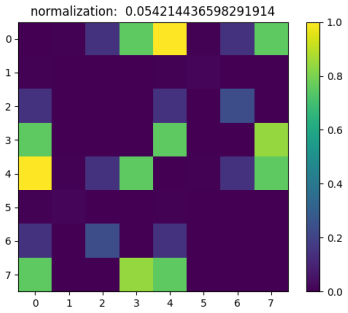

(d) Groundstate in converged molecular orbitals

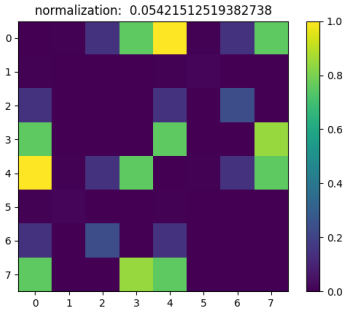

(e) Groundstate in natural molecular orbitals

Figure 10.1: Quantum mutual information for H_2 molecule.

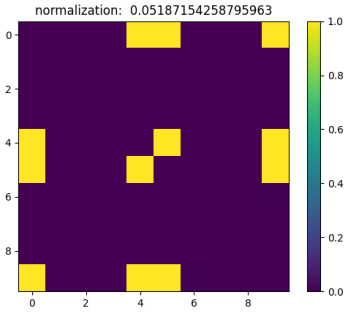

(a) VQE state in HF molecular orbitals

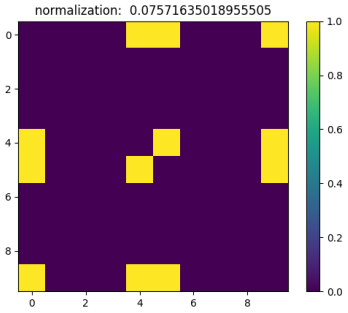

(b) WAHTOR state in converged molecular orbitals

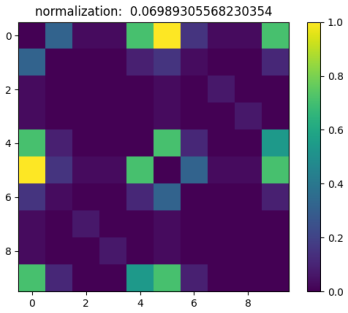

(c) Groundstate in HF molecular orbitals

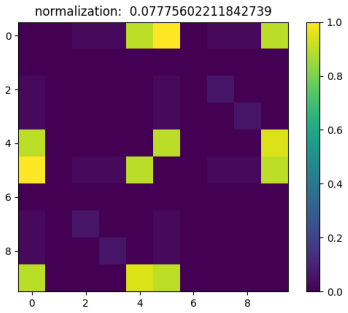

(d) Groundstate in converged molecular orbitals

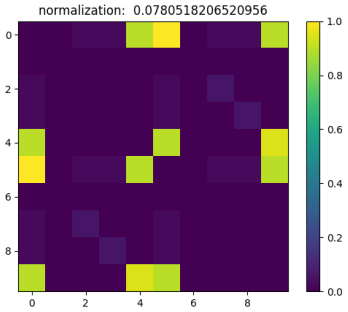

(e) Groundstate in natural molecular orbitals

Figure 10.2: Quantum mutual information for LiH molecule.

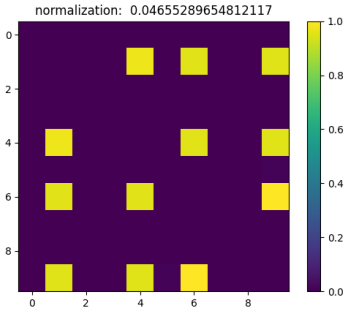

(a) VQE state in HF molecular orbitals

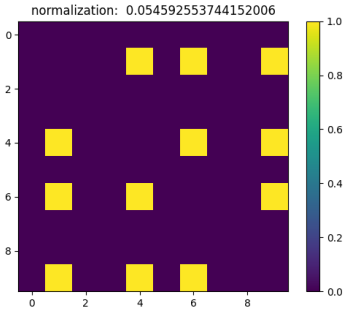

(b) WAHTOR state in converged molecular orbitals

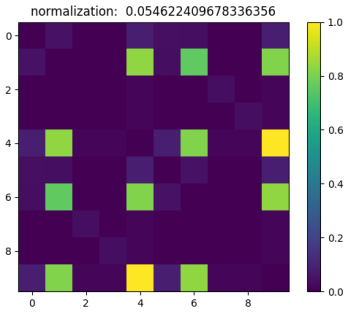

(c) Groundstate in HF molecular orbitals

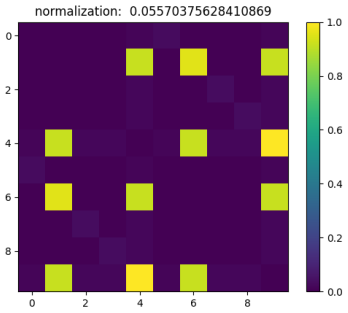

(d) Groundstate in converged molecular orbitals

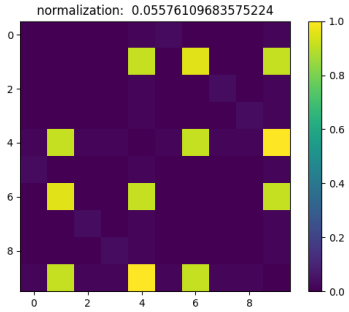

(e) Groundstate in natural molecular orbitals

Figure 10.3: Quantum mutual information for HF molecule.

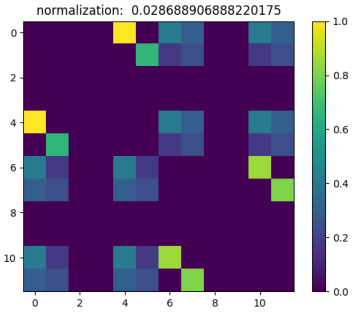

(a) VQE state in HF molecular orbitals

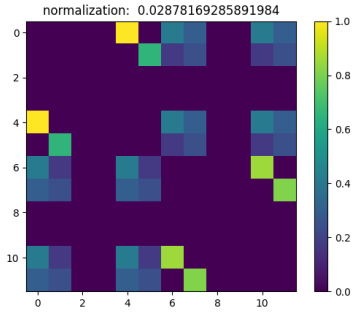

(b) WAHTOR state in converged molecular orbitals

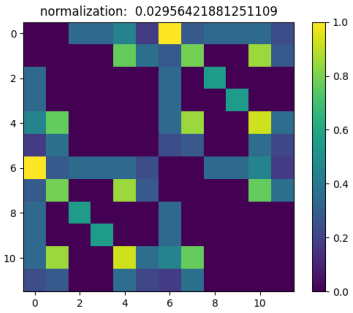

(c) Groundstate in HF molecular orbitals

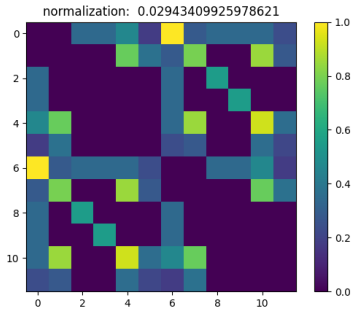

(d) Groundstate in converged molecular orbitals

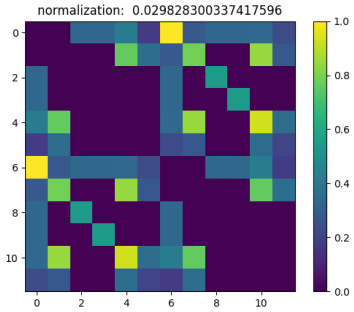

(e) Groundstate in natural molecular orbitals

Figure 10.4: Quantum mutual information for BeH_2 molecule.

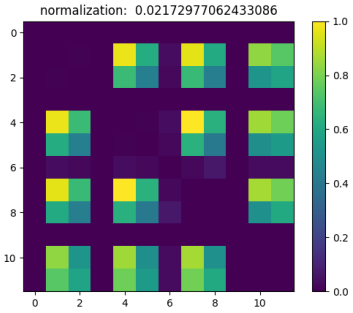

(a) VQE state in HF molecular orbitals

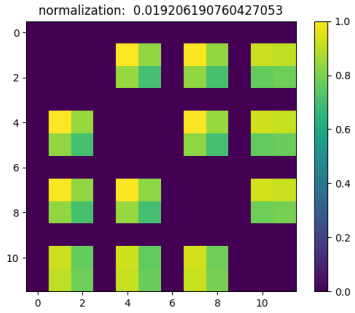

(b) WAHTOR state in converged molecular orbitals

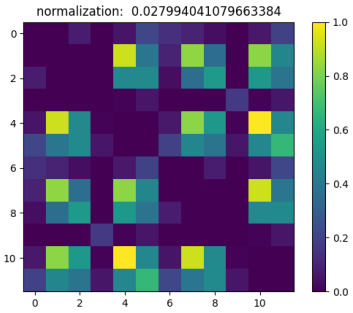

(c) Groundstate in HF molecular orbitals

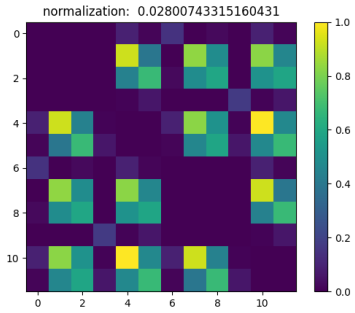

(d) Groundstate in converged molecular orbitals

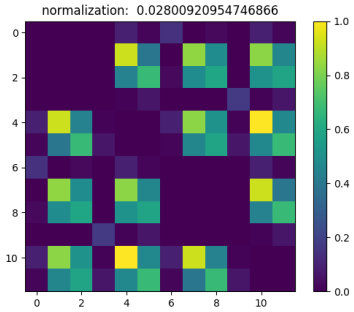

(e) Groundstate in natural molecular orbitals

Figure 10.5: Quantum mutual information for H_2S molecule.

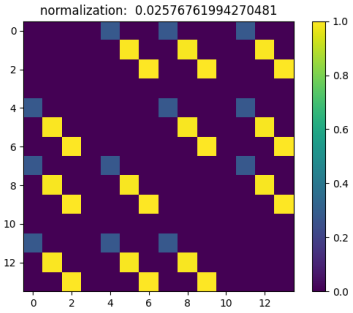

(a) VQE state in HF molecular orbitals

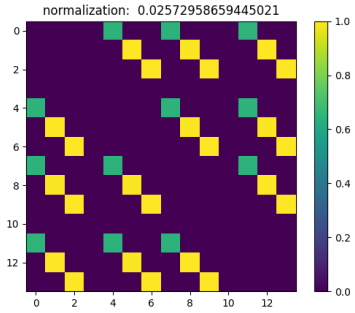

(b) WAHTOR state in converged molecular orbitals

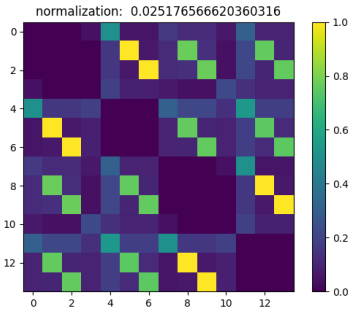

(c) Groundstate in HF molecular orbitals

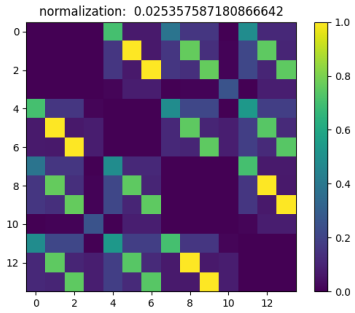

(d) Groundstate in converged molecular orbitals

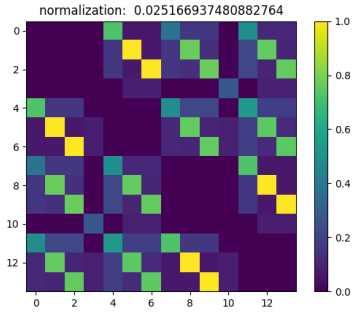

(e) Groundstate in natural molecular orbitals

Figure 10.6: Quantum mutual information for NH_3 molecule.

Bibliography

[1] M. A. Nielsen and I. L. Chuang, *Quantum Computation and Quantum Information*. Cambridge University Press, 2010.

[2] G. Benenti, G. Casati, and G. Strini, *Principles of Quantum Computation and Information*. WORLD SCIENTIFIC, 4 2004.

[3] S. Kais, *INTRODUCTION TO QUANTUM INFORMATION AND COMPUTATION FOR CHEMISTRY*. 2014.

[4] S. Attila and O. N. S., *Modern Quantum Chemistry: Introduction to Advanced Electronic Structure Theory*. Dover Publications, 2012.

[5] S. McArdle, S. Endo, A. Aspuru-Guzik, S. C. Benjamin, and X. Yuan, "Quantum computational chemistry," *Reviews of Modern Physics*, vol. 92, pp. 1–59, 2020.

[6] J. J. Sakurai and J. Napolitano, *Modern Quantum Mechanics*. Cambridge University Press, 9 2017.

[7] B. H. Bransden and C. J. Joachain, *Physics of atoms and molecules*. Pearson Education India, 2003.

[8] N. W. Ashcroft and N. D. Mermin, *Solid State Physics*. Holt-Saunders, 1976.

[9] A. L. Fetter and J. D. Walecka, *Quantum Theory of Many-Particle Systems*. Dover Publications, 6 2003.

[10] A. Altland and B. D. Simons, *Condensed Matter Field Theory*. Cambridge University Press, 3 2010.

[11] G. D. Mahan, *Many-Particle Physics*. Plenum, 2000.

[12] M. A. Nielsen, "The fermionic canonical commutation relations and the jordan-wigner transform," 2005.

[13] M. Tinkham, *Introduction to Superconductivity: Second Edition*. Dover Publications, 2004.

[14] P. G. D. Gennes, *Superconductivity of Metals and Alloys*. CRC Press, 3 2018.

[15] T. Helgaker, P. Jørgensen, and J. Olsen, *Molecular Electronic Structure Theory*. John Wiley Sons, LTD, 2000.

[16] G. Giuliani and G. Vignale, *Quantum Theory of the Electron Liquid*. Cambridge University Press, 3 2005.

[17] P.-O. Löwdin, "Quantum theory of many-particle systems. i. physical interpretations by means of density matrices, natural spin-orbitals, and convergence problems in the method of configurational interaction," *Physical Review*, vol. 97, pp. 1474–1489, 3 1955.

[18] C. F. Bender and E. R. Davidson, "A natural orbital based energy calculation for helium hydride and lithium hydride," *The Journal of Physical Chemistry*, vol. 70, pp. 2675–2685, 8 1966.

[19] F. Coester, "Bound states of a many-particle system," *Nuclear Physics*, vol. 7, pp. 421–424, 6 1958.

[20] F. Coester and H. Kümmel, "Short-range correlations in nuclear wave functions," *Nuclear Physics*, vol. 17, pp. 477–485, 6 1960.

[21] J. Cizek and J. Paldus, "Coupled cluster approach," *Physica Scripta*, vol. 21, pp. 251–254, 1 1980.

[22] J. Preskill, "Quantum computing in the nisq era and beyond," *Quantum*, vol. 2, pp. 1–20, 2018.

[23] P. Jordan and E. Wigner, "Über das paulische Äquivalenzverbot," vol. 1927, 1928.

[24] J. T. Seeley, M. J. Richard, and P. J. Love, "The bravyi-kitaev transformation for quantum computation of electronic structure," *Journal of Chemical Physics*, vol. 137, 2012.

[25] A. Aspuru-Guzik, A. D. Dutoi, P. J. Love, and M. Head-Gordon, "Simulated quantum computation of molecular energies," *Science*, vol. 309, pp. 1704–1707, 9 2005.

[26] S. B. Bravyi and A. Y. Kitaev, "Fermionic quantum computation," *Annals of Physics*, vol. 298, pp. 210–226, 2002.

[27] O. D. Matteo, A. McCoy, P. Gysbers, T. Miyagi, R. M. Woloshyn, and P. Navrátil, "Improving hamiltonian encodings with the gray code," *Physical Review A*, vol. 103, p. 042405, 4 2021.

[28] S. Bravyi, J. M. Gambetta, A. Mezzacapo, and K. Temme, "Tapering off qubits to simulate fermionic hamiltonians," 1 2017.

[29] K. Setia, R. Chen, J. E. Rice, A. Mezzacapo, M. Pistoia, and J. D. Whitfield, "Reducing qubit requirements for quantum simulations using molecular point group symmetries," *Journal of Chemical Theory and Computation*, vol. 16, pp. 6091–6097, 10 2020.

[30] F. Verstraete and J. I. Cirac, "Mapping local hamiltonians of fermions to local hamiltonians of spins," *Journal of Statistical Mechanics: Theory and Experiment*, vol. 2005, pp. P09012–P09012, 9 2005.

[31] R. C. Ball, "Fermions without fermion fields," *Physical Review Letters*, vol. 95, p. 176407, 10 2005.

[32] T. C. Farrelly and A. J. Short, "Causal fermions in discrete spacetime," *Physical Review A*, vol. 89, p. 012302, 1 2014.

[33] M. Steudtner and S. Wehner, "Quantum codes for quantum simulation of fermions on a square lattice of qubits," *Physical Review A*, vol. 99, p. 022308, 2 2019.

[34] J. D. Whitfield, V. Havlíček, and M. Troyer, "Local spin operators for fermion simulations," *Physical Review A*, vol. 94, p. 030301, 9 2016.

[35] A. Peruzzo, J. McClean, P. Shadbolt, M. H. Yung, X. Q. Zhou, P. J. Love, A. Aspuru-Guzik, and J. L. O'Brien, "A variational eigenvalue solver on a photonic quantum processor," *Nature Communications*, vol. 5, 7 2014.

[36] J. R. McClean, J. Romero, R. Babbush, and A. Aspuru-Guzik, "The theory of variational hybrid quantum-classical algorithms," *New Journal of Physics*, vol. 18, p. 023023, 2 2016.

[37] D. S. Abrams and S. Lloyd, "Quantum algorithm providing exponential speed increase for finding eigenvalues and eigenvectors," *Physical Review Letters*, vol. 83, pp. 5162–5165, 12 1999.

[38] J. Romero, R. Babbush, J. R. McClean, C. Hempel, P. J. Love, and A. Aspuru-Guzik, "Strategies for quantum computing molecular energies using the unitary coupled cluster ansatz," *Quantum Science and Technology*, vol. 4, pp. 1–18, 2019.

[39] D. Wecker, M. B. Hastings, and M. Troyer, "Progress towards practical quantum variational algorithms," *Physical Review A*, vol. 92, p. 042303, 10 2015.

[40] M. R. Hoffmann and J. Simons, "A unitary multiconfigurational coupled-cluster method: Theory and applications," *The Journal of Chemical Physics*, vol. 88, pp. 993–1002, 1 1988.

[41] R. J. Bartlett, S. A. Kucharski, and J. Noga, "Alternative coupled-cluster ansätze ii. the unitary coupled-cluster method," *Chemical Physics Letters*, vol. 155, pp. 133–140, 2 1989.

[42] J. R. McClean, S. Boixo, V. N. Smelyanskiy, R. Babbush, and H. Neven, "Barren plateaus in quantum neural network training landscapes," *Nature Communications*, vol. 9, p. 4812, 11 2018.

[43] E. Grant, L. Wossnig, M. Ostaszewski, and M. Benedetti, "An initialization strategy for addressing barren plateaus in parametrized quantum circuits," *Quantum*, vol. 3, p. 214, 12 2019.

[44] A. Kandala, A. Mezzacapo, K. Temme, M. Takita, M. Brink, J. M. Chow, and J. M. Gambetta, "Hardware-efficient variational quantum eigensolver for small molecules and quantum magnets," *Nature*, vol. 549, pp. 242–246, 2017.

[45] T. Giurgica-Tiron, Y. Hindy, R. Larose, A. Mari, and W. J. Zeng, "Digital zero noise extrapolation for quantum error mitigation," pp. 306–316, Institute of Electrical and Electronics Engineers Inc., 10 2020.

[46] K. Temme, S. Bravyi, and J. M. Gambetta, "Error mitigation for short-depth quantum circuits," *Physical Review Letters*, vol. 119, pp. 1–15, 2017.

[47] R. P. Feynman, "Simulating physics with computers," *International Journal of Theoretical Physics*, vol. 21, pp. 467–488, 1982.

[48] V. E. Elfving, B. W. Broer, M. Webber, J. Gavartin, M. D. Halls, K. P. Lorton, and A. Bochevarov, "How will quantum computers provide an industrially relevant computational advantage in quantum chemistry?," pp. 1–20, 2020.

[49] S. McArdle, T. Jones, S. Endo, Y. Li, S. C. Benjamin, and X. Yuan, "Variational ansatz-based quantum simulation of imaginary time evolution," *npj Quantum Information*, vol. 5, pp. 1–14, 2019.

[50] B. Bauer, S. Bravyi, M. Motta, and G. K.-L. Chan, "Quantum algorithms for quantum chemistry and quantum materials science," *Chemical Reviews*, vol. 120, pp. 12685–12717, 11 2020.

[51] A. Y. Kitaev, "Quantum measurements and the abelian stabilizer problem," pp. 1–22, 1995.

[52] R. Cleve, A. Ekert, C. Macchiavello, and M. Mosca, "Quantum algorithms revisited," *Proceedings of the Royal Society A: Mathematical, Physical and Engineering Sciences*, vol. 454, pp. 339–354, 1998.

[53] N. P. Bauman, H. Liu, E. J. Bylaska, S. Krishnamoorthy, G. H. Low, C. E. Granade, N. Wiebe, N. A. Baker, B. Peng, M. Roetteler, M. Troyer, and K. Kowalski, "Toward quantum computing for high-energy excited states in molecular systems: Quantum phase estimations of core-level states," *Journal of Chemical Theory and Computation*, vol. 17, pp. 201–210, 2021.

[54] T. Bian, D. Murphy, R. Xia, A. Daskin, and S. Kais, "Quantum computing methods for electronic states of the water molecule," *Molecular Physics*, vol. 117, pp. 2069–2082, 2019.

[55] H. Wang, S. Kais, A. Aspuru-Guzik, and M. R. Hoffmann, "Quantum algorithm for obtaining the energy spectrum of molecular systems," *Phys. Chem. Chem. Phys.*, vol. 10, pp. 5388–5393, 2008.

[56] Y. Cao, J. Romero, J. P. Olson, M. Degroote, P. D. Johnson, M. Kieferová, I. D. Kivlichan, T. Menke, B. Peropadre, N. P. Sawaya, S. Sim, L. Veis, and A. Aspuru-Guzik, "Quantum chemistry in the age of quantum computing," *Chemical Reviews*, vol. 119, pp. 10856–10915, 2019.

[57] L. Ding, S. Mardazad, S. Das, S. Szalay, U. Schollwöck, Z. Zimborás, and C. Schilling, "Concept of orbital entanglement and correlation in quantum chemistry," *Journal of Chemical Theory and Computation*, vol. 17, pp. 79–95, 2021.

[58] Y. Nam, J. S. Chen, N. C. Pisenti, K. Wright, C. Delaney, D. Maslov, K. R. Brown, S. Allen, J. M. Amini, J. Apisdorf, K. M. Beck, A. Blinov, V. Chaplin, M. Chmielewski, C. Collins, S. Debnath, K. M. Hudek,

A. M. Ducore, M. Keesan, S. M. Kreikemeier, J. Mizrahi, P. Solomon, M. Williams, J. D. Wong-Campos, D. Moehring, C. Monroe, and J. Kim, "Ground-state energy estimation of the water molecule on a trapped-ion quantum computer," *npj Quantum Information*, vol. 6, p. 33, 12 2020.

[59] J. R. McClean, J. Romero, R. Babbush, and A. Aspuru-Guzik, "The theory of variational hybrid quantum-classical algorithms," *New Journal of Physics*, vol. 18, 2016.

[60] P. J. O'Malley, R. Babbush, I. D. Kivlichan, J. Romero, J. R. McClean, R. Barends, J. Kelly, P. Roushan, A. Tranter, N. Ding, B. Campbell, Y. Chen, Z. Chen, B. Chiaro, A. Dunsworth, A. G. Fowler, E. Jeffrey, E. Lucero, A. Megrant, J. Y. Mutus, M. Neeley, C. Neill, C. Quintana, D. Sank, A. Vainsencher, J. Wenner, T. C. White, P. V. Coveney, P. J. Love, H. Neven, A. Aspuru-Guzik, and J. M. Martinis, "Scalable quantum simulation of molecular energies," *Physical Review X*, vol. 6, pp. 1–13, 2016.

[61] J. Lee, W. J. Huggins, M. Head-Gordon, and K. B. Whaley, "Generalized unitary coupled cluster wave functions for quantum computation," *Journal of Chemical Theory and Computation*, vol. 15, pp. 311–324, 2019.

[62] R. Xia and S. Kais, "Qubit coupled cluster singles and doubles variational quantum eigensolver ansatz for electronic structure calculations," *Quantum Science and Technology*, vol. 6, pp. 1–13, 2020.

[63] P. J. Ollitrault, A. Baiardi, M. Reiher, and I. Tavernelli, "Hardware efficient quantum algorithms for vibrational structure calculations," *Chemical Science*, vol. 11, pp. 6842–6855, 2020.

[64] F. Benfenati, L. Guidoni, G. Mazzola, P. Barkoutsos, P. Ollitrault, and I. Tavernelli, "Extended wavefunctions for the variational quantum eigensolver," p. F5A.36, Optical Society of America, 2019.

[65] F. Benfenati, G. Mazzola, C. Capecci, P. K. Barkoutsos, P. J. Ollitrault, I. Tavernelli, and L. Guidoni, "Improved accuracy on noisy devices by nonunitary variational quantum eigensolver for chemistry applications," *Journal of Chemical Theory and Computation*, vol. 17, p. 3946–3954, 2021.

[66] M. Cerezo, A. Sone, T. Volkoff, L. Cincio, and P. J. Coles, "Cost function dependent barren plateaus in shallow parametrized quantum circuits," *Nature Communications*, vol. 12, 12 2021.

[67] M. Ganzhorn, D. J. Egger, P. Barkoutsos, P. Ollitrault, G. Salis, N. Moll, M. Roth, A. Fuhrer, P. Mueller, S. Woerner, I. Tavernelli, and S. Filipp, "Gate-efficient simulation of molecular eigenstates on a quantum computer," *Physical Review Applied*, vol. 11, 2019.

[68] W. Mizukami, K. Mitarai, Y. O. Nakagawa, T. Yamamoto, T. Yan, and Y. ya Ohnishi, "Orbital optimized unitary coupled cluster theory for quantum computer," *Phys. Rev. Research*, vol. 2, p. 33421, 9 2020.

[69] P. K. Barkoutsos, J. F. Gonthier, I. Sokolov, N. Moll, G. Salis, A. Fuhrer, M. Ganzhorn, D. J. Egger, M. Troyer, A. Mezzacapo, S. Filipp, and I. Tavernelli, "Quantum algorithms for electronic structure calculations: Particle-hole hamiltonian and optimized wave-function expansions," *Physical Review A*, vol. 98, pp. 1–14, 2018.

[70] G. G. Guerreschi and M. Smelyanskiy, "Practical optimization for hybrid quantum-classical algorithms," 1 2017.

[71] N. Moll, P. Barkoutsos, L. S. Bishop, J. M. Chow, A. Cross, D. J. Egger, S. Filipp, A. Fuhrer, J. M. Gambetta, M. Ganzhorn, A. Kandala, A. Mezzacapo, P. Müller, W. Riess, G. Salis, J. Smolin, I. Tavernelli, and K. Temme, "Quantum optimization using variational algorithms on near-term quantum devices," *Quantum Science and Technology*, vol. 3, p. 030503, 7 2018.

[72] Q. Sun, T. C. Berkelbach, N. S. Blunt, G. H. Booth, S. Guo, Z. Li, J. Liu, J. D. McClain, E. R. Sayfutyarova, S. Sharma, S. Wouters, and G. K.-L. Chan, "Pyscf: the python-based simulations of chemistry framework," *WIREs Computational Molecular Science*, vol. 8, p. e1340, 2018.

[73] G. Aleksandrowicz, T. Alexander, P. Barkoutsos, L. Bello, Y. Ben-Haim, D. Bucher, F. J. Cabrera-Hernández, J. Carballo-Franquis, A. Chen, C.-F. Chen, J. M. Chow, A. D. Córcoles-Gonzales, A. J. Cross, A. Cross, J. Cruz-Benito, C. Culver, S. D. L. P. González, E. D. L. Torre, D. Ding, E. Dumitrescu, I. Duran, P. Eendebak, M. Everitt, I. F. Sertage, A. Frisch, A. Fuhrer, J. Gambetta, B. G. Gago, J. Gomez-Mosquera, D. Greenberg, I. Hamamura, V. Havlicek, J. Hellmers, Łukasz Herok, H. Horii, S. Hu, T. Imamichi, T. Itoko,

A. Javadi-Abhari, N. Kanazawa, A. Karazeev, K. Krsulich, P. Liu, Y. Luh, Y. Maeng, M. Marques, F. J. Martín-Fernández, D. T. McClure, D. McKay, S. Meesala, A. Mezzacapo, N. Moll, D. M. Rodríguez, G. Nannicini, P. Nation, P. Ollitrault, L. J. O'Riordan, H. Paik, J. Pérez, A. Phan, M. Pistoia, V. Prutyanov, M. Reuter, J. Rice, A. R. Davila, R. H. P. Rudy, M. Ryu, N. Sathaye, C. Schnabel, E. Schoute, K. Setia, Y. Shi, A. Silva, Y. Siraichi, S. Sivarajah, J. A. Smolin, M. Soeken, H. Takahashi, I. Tavernelli, C. Taylor, P. Taylour, K. Trabing, M. Treinish, W. Turner, D. Vogt-Lee, C. Vuillot, J. A. Wildstrom, J. Wilson, E. Winston, C. Wood, S. Wood, S. Wörner, I. Y. Akhalwaya, and C. Zoufal, "Qiskit: An open-source framework for quantum computing," 1 2019.

[74] J. R. Johansson, P. D. Nation, and F. Nori, "Qutip: An open-source python framework for the dynamics of open quantum systems," *Computer Physics Communications*, vol. 183, pp. 1760–1772, 2012.

[75] J. R. Johansson, P. D. Nation, and F. Nori, "Qutip 2: A python framework for the dynamics of open quantum systems," *Computer Physics Communications*, vol. 184, pp. 1234–1240, 2013.

[76] R. H. Byrd, P. Lu, J. Nocedal, and C. Zhu, "A limited memory algorithm for bound constrained optimization," *SIAM Journal on Scientific Computing*, vol. 16, pp. 1190–1208, 1995.

[77] M. J. D. Powell, "Advances in optimization and numerical analysis," 1994.

[78] J. M. F. A. S. F. Boys, "Canonical configuration interaction procedure," *Reviews of Modern Physics*, vol. 32, pp. 300–302, 1960.

[79] T. Y. Nikolaienko and L. A. Bulavin, "Localized orbitals for optimal decomposition of molecular properties," *International Journal of Quantum Chemistry*, vol. 119, pp. 38–55, 2019.

[80] S. Saebø and P. Pulay, "Local treatment of electron correlation," *Annual Review of Physical Chemistry*, vol. 44, pp. 213–236, 1993.

[81] A. D. Corcoles, A. Kandala, A. Javadi-Abhari, D. T. McClure, A. W. Cross, K. Temme, P. D. Nation, M. Steffen, and J. M. Gambetta, "Challenges and opportunities of near-term quantum computing systems," *Proceedings of the IEEE*, vol. 108, pp. 1338–1352, 2020.

[82] N. V. Tkachenko, J. Sud, Y. Zhang, S. Tretiak, P. M. Anisimov, A. T. Arrasmith, P. J. Coles, L. Cincio, and P. A. Dub, "Correlation-informed permutation of qubits for reducing ansatz depth in the variational quantum eigensolver," *PRX Quantum*, vol. 2, p. 1, 2021.

[83] Q. Gao, H. Nakamura, T. P. Gujarati, G. O. Jones, J. E. Rice, S. P. Wood, M. Pistoia, J. M. Garcia, and N. Yamamoto, "Computational investigations of the lithium superoxide dimer rearrangement on noisy quantum devices," *The Journal of Physical Chemistry A*, vol. 125, pp. 1827–1836, 2 2021.

[84] M. Urbanek, D. Camps, R. V. Beeumen, and W. A. de Jong, "Chemistry on quantum computers with virtual quantum subspace expansion," *Journal of Chemical Theory and Computation*, vol. 16, pp. 5425–5431, 8 2020.

[85] P. W. Shor, "Polynomial-time algorithms for prime factorization and discrete logarithms on a quantum computer," *SIAM Journal on Computing*, vol. 26, 1997.

[86] H. Bernien, S. Schwartz, A. Keesling, H. Levine, A. Omran, H. Pichler, S. Choi, A. S. Zibrov, M. Endres, M. Greiner, V. Vuletić, and M. D. Lukin, "Probing many-body dynamics on a 51-atom quantum simulator," *Nature*, vol. 551, pp. 579–584, 11 2017.

[87] M. C. Bañuls, R. Blatt, J. Catani, A. Celi, J. I. Cirac, M. Dalmonte, L. Fallani, K. Jansen, M. Lewenstein, S. Montangero, C. A. Muschik, B. Reznik, E. Rico, L. Tagliacozzo, K. V. Acoleyen, F. Verstraete, U.-J. Wiese, M. Wingate, J. Zakrzewski, and P. Zoller, "Simulating lattice gauge theories within quantum technologies," *The European Physical Journal D*, vol. 74, p. 165, 8 2020.

[88] H. Hussain, M. B. Javaid, F. S. Khan, A. Dalal, and A. Khalique, "Optimal control of traffic signals using quantum annealing," *Quantum Information Processing*, vol. 19, p. 312, 9 2020.

[89] D. J. Egger, C. Gambella, J. Marecek, S. McFaddin, M. Mevissen, R. Raymond, A. Simonetto, S. Woerner, and E. Yndurain, "Quantum computing for finance: State-of-the-art and future prospects," *IEEE Transactions on Quantum Engineering*, vol. 1, pp. 1–24, 1 2021.

[90] F. Arute, K. Arya, R. Babbush, D. Bacon, J. C. Bardin, R. Barends, R. Biswas, S. Boixo, F. G. Brandao, D. A. Buell, B. Burkett,

Y. Chen, Z. Chen, B. Chiaro, R. Collins, W. Courtney, A. Dunsworth, E. Farhi, B. Foxen, A. Fowler, C. Gidney, M. Giustina, R. Graff, K. Guerin, S. Habegger, M. P. Harrigan, M. J. Hartmann, A. Ho, M. Hoffmann, T. Huang, T. S. Humble, S. V. Isakov, E. Jeffrey, Z. Jiang, D. Kafri, K. Kechedzhi, J. Kelly, P. V. Klimov, S. Knysh, A. Korotkov, F. Kostritsa, D. Landhuis, M. Lindmark, E. Lucero, D. Lyakh, S. Mandrà, J. R. McClean, M. McEwen, A. Megrant, X. Mi, K. Michielsen, M. Mohseni, J. Mutus, O. Naaman, M. Neeley, C. Neill, M. Y. Niu, E. Ostby, A. Petukhov, J. C. Platt, C. Quintana, E. G. Rieffel, P. Roushan, N. C. Rubin, D. Sank, K. J. Satzinger, V. Smelyanskiy, K. J. Sung, M. D. Trevithick, A. Vainsencher, B. Villalonga, T. White, Z. J. Yao, P. Yeh, A. Zalcman, H. Neven, and J. M. Martinis, "Quantum supremacy using a programmable superconducting processor," *Nature*, vol. 574, pp. 505–510, 2019.

[91] N. H. Stair and F. A. Evangelista, "Simulating many-body systems with a projective quantum eigensolver," *PRX Quantum*, vol. 2, p. 030301, 7 2021.

[92] S. Barison, F. Vicentini, and G. Carleo, "An efficient quantum algorithm for the time evolution of parameterized circuits," *Quantum*, vol. 5, p. 512, 7 2021.

[93] R. Xia and S. Kais, "Quantum machine learning for electronic structure calculations," *Nature Communications*, vol. 9, p. 4195, 10 2018.

[94] D. A. Fedorov, B. Peng, N. Govind, and Y. Alexeev, "Vqe method: a short survey and recent developments," *Materials Theory*, vol. 6, p. 2, 1 2022.

[95] J. Tilly, H. Chen, S. Cao, D. Picozzi, K. Setia, Y. Li, E. Grant, L. Wossnig, I. Rungger, G. H. Booth, and J. Tennyson, "The variational quantum eigensolver: A review of methods and best practices," *Physics Reports*, vol. 986, pp. 1–128, 11 2022.

[96] H. R. Grimsley, S. E. Economou, E. Barnes, and N. J. Mayhall, "An adaptive variational algorithm for exact molecular simulations on a quantum computer," *Nature Communications*, vol. 10, 2019.

[97] Y. S. Yordanov, V. Armaos, C. H. W. Barnes, and D. R. M. Arvidsson-Shukur, "Qubit-excitation-based adaptive variational quantum eigensolver," *Communications Physics*, vol. 4, p. 228, 10 2021.

[98] D. Castaldo, S. Jahangiri, A. Delgado, and S. Corni, "Quantum simulation of molecules in solution," *Journal of Chemical Theory and Computation*, vol. 18, pp. 7457–7469, 12 2022.

[99] W. Kutzelnigg, "Error analysis and improvements of coupled-cluster theory," *Theoretica Chimica Acta*, vol. 80, pp. 349–386, 7 1991.

[100] D. J. Egger, C. Capecci, B. Pokharel, P. K. Barkoutsos, L. E. Fischer, L. Guidoni, and I. Tavernelli, "A study of the pulse-based variational quantum eigensolver on cross-resonance based hardware," pp. 1–13, 2023.

[101] O. R. Meitei, B. T. Gard, G. S. Barron, D. P. Pappas, S. E. Economou, E. Barnes, and N. J. Mayhall, "Gate-free state preparation for fast variational quantum eigensolver simulations," *npj Quantum Information*, vol. 7, pp. 1–11, 2021.

[102] Z. Liang, J. Cheng, H. Ren, H. Wang, F. Hua, Y. Ding, F. Chong, S. Han, Y. Shi, and X. Qian, "Pan: Pulse ansatz on nisq machines," pp. 1–13, 2022.

[103] L. Ratini, C. Capecci, F. Benfenati, and L. Guidoni, "Wave function adapted hamiltonians for quantum computing," *Journal of Chemical Theory and Computation*, vol. 18, pp. 899–909, 2022.

[104] J. Nocedal and S. J. Wright, *Numerical Optimization*. Springer, 1999.

[105] R. Fletcher, *Practical Methods of Optimization*. John Wiley Sons, second ed., 1987.

[106] I. O. Sokolov, P. K. Barkoutsos, P. J. Ollitrault, D. Greenberg, J. Rice, M. Pistoia, and I. Tavernelli, "Quantum orbital-optimized unitary coupled cluster methods in the strongly correlated regime: Can quantum algorithms outperform their classical equivalents?," *Journal of Chemical Physics*, vol. 152, pp. 1–18, 2020.

[107] C. Cade, L. Mineh, A. Montanaro, and S. Stanisic, "Strategies for solving the fermi-hubbard model on near-term quantum computers," *Physical Review B*, vol. 102, p. 235122, 12 2020.

[108] P. Suchsland, P. K. Barkoutsos, I. Tavernelli, M. H. Fischer, and T. Neupert, "Simulating a ring-like hubbard system with a quantum computer," *Physical Review Research*, vol. 4, p. 013165, 3 2022.

[109] M. Consiglio, W. J. Chetcuti, C. Bravo-Prieto, S. Ramos-Calderer, A. Minguzzi, J. I. Latorre, L. Amico, and T. J. G. Apollaro, "Variational quantum eigensolver for su(n) fermions," *Journal of Physics A: Mathematical and Theoretical*, vol. 55, p. 265301, 7 2022.

[110] P. Jordan and E. P. Wigner, "Über das paulische Äquivalenzverbot," 1993.

[111] T. J. Ypma, "Historical development of the newton–raphson method," *SIAM Review*, vol. 37, pp. 531–551, 1995.

[112] C. G. BROYDEN, "The convergence of a class of double-rank minimization algorithms 1. general considerations," *IMA Journal of Applied Mathematics*, vol. 6, pp. 76–90, 1970.

[113] R. Fletcher, "A new approach to variable metric algorithms," *The Computer Journal*, vol. 13, pp. 317–322, 1970.

[114] D. Goldfarb, "A family of variable-metric methods derived by variational means," *Math. Comp.*, vol. 24, pp. 23–26, 1970.

[115] D. F. Shanno, "Conditioning of quasi-newton methods for function minimization," *Math. Comp.*, vol. 24, pp. 647–656, 1970.

[116] W. Gander, "On halley's iteration method," *The American Mathematical Monthly*, vol. 92, p. 131, 2 1985.

[117] C. Gnang and F. Dubeau, "On the rediscovery of halley's iterative method for computing the zero of an analytic function," *Journal of Computational and Applied Mathematics*, vol. 335, pp. 129–141, 6 2018.

[118] D. S. Abrams and S. Lloyd, "Simulation of many-body fermi systems on a universal quantum computer," *Physical Review Letters*, vol. 79, pp. 2586–2589, 9 1997.

[119] E. R. Davidson, "Properties and uses of natural orbitals," *Reviews of Modern Physics*, vol. 44, pp. 451–464, 7 1972.

[120] Ákos Rapp, G. Zaránd, C. Honerkamp, and W. Hofstetter, "Color superfluidity and "baryon" formation in ultracold fermions," *Physical Review Letters*, vol. 98, p. 160405, 4 2007.

[121] D. P. Arovas, A. Karlhede, and D. Lilliehöök, "Su(n) quantum hall skyrmions," *Physical Review B*, vol. 59, pp. 13147–13150, 5 1999.

[122] F. Scazza, C. Hofrichter, M. Höfer, P. C. D. Groot, I. Bloch, and S. Fölling, "Observation of two-orbital spin-exchange interactions with ultracold su(n)-symmetric fermions," *Nature Physics*, vol. 10, pp. 779–784, 10 2014.

[123] N. N. Bogoljubov, "On a new method in the theory of superconductivity," *Il Nuovo Cimento*, vol. 7, pp. 794–805, 3 1958.

[124] J. G. Valatin, "Comments on the theory of superconductivity," *Il Nuovo Cimento*, vol. 7, pp. 843–857, 3 1958.

[125] E. Lieb, T. Schultz, and D. Mattis, "Two soluble models of an antiferromagnetic chain," *Annals of Physics*, vol. 16, pp. 407–466, 12 1961.

[126] G. B. Mbeng, A. Russomanno, and G. E. Santoro, "The quantum ising chain for beginners," 9 2020.

[127] Z. C. Seskir, R. Korkmaz, and A. U. Aydinoglu, "The landscape of the quantum start-up ecosystem," *EPJ Quantum Technology 2022 9:1*, vol. 9, pp. 1–15, 10 2022.

[128] A. Robert, P. K. Barkoutsos, S. Woerner, and I. Tavernelli, "Resource-efficient quantum algorithm for protein folding," *npj Quantum Information*, vol. 7, 12 2021.

[129] K. Bharti, A. Cervera-Lierta, T. H. Kyaw, T. Haug, S. Alperin-Lea, A. Anand, M. Degroote, H. Heimonen, J. S. Kottmann, T. Menke, W. K. Mok, S. Sim, L. C. Kwek, and A. Aspuru-Guzik, "Noisy intermediate-scale quantum algorithms," *Reviews of Modern Physics*, vol. 94, p. 015004, 3 2022.

[130] M. R. Hoffmann and J. Simons, "A unitary multiconfigurational coupled-cluster method: Theory and applications," *The Journal of Chemical Physics*, vol. 88, p. 993, 8 1998.

[131] B. Cooper and P. J. Knowles, "Benchmark studies of variational, unitary and extended coupled cluster methods," *The Journal of Chemical Physics*, vol. 133, p. 234102, 12 2010.

[132] F. A. Evangelista, "Alternative single-reference coupled cluster approaches for multireference problems: The simpler, the better," *The Journal of Chemical Physics*, vol. 134, p. 224102, 6 2011.

[133] J. D. Whitfield, J. Biamonte, and A. Aspuru-Guzik, "Simulation of electronic structure hamiltonians using quantum computers," *http://dx.doi.org/10.1080/00268976.2011.552441*, vol. 109, pp. 735–750, 3 2011.

[134] C. Møller and M. S. Plesset, "Note on an approximation treatment for many-electron systems," *Physical Review*, vol. 46, 1934.

[135] Legeza and J. Sólyom, "Optimizing the density-matrix renormalization group method using quantum information entropy," *Physical Review B - Condensed Matter and Materials Physics*, vol. 68, p. 195116, 11 2003.

[136] L. Amico, R. Fazio, A. Osterloh, and V. Vedral, "Entanglement in many-body systems," *Reviews of Modern Physics*, vol. 80, pp. 517–576, 5 2008.

[137] Z. Huang and S. Kais, "Entanglement as measure of electron–electron correlation in quantum chemistry calculations," *Chemical Physics Letters*, vol. 413, pp. 1–5, 9 2005.

[138] J. von Neumann, "Mathematische grundlagen der quantenmechanik," *Mathematische Grundlagen der Quantenmechanik*, 1996.

[139] J. Rissler, R. M. Noack, and S. R. White, "Measuring orbital interaction using quantum information theory," *Chemical Physics*, vol. 323, pp. 519–531, 4 2006.

[140] D. R. Hartree, "The wave mechanics of an atom with a non-coulomb central field. part ii. some results and discussion," *Mathematical Proceedings of the Cambridge Philosophical Society*, vol. 24, pp. 111–132, 1928.

[141] P. J. Knowles and N. C. Handy, "A new determinant-based full configuration interaction method," *Chemical Physics Letters*, vol. 111, pp. 315–321, 11 1984.

[142] B. Zeng, X. Chen, D.-L. Zhou, and X.-G. Wen, *Quantum Information Meets Quantum Matter*. Springer New York, 2019.

[143] F. Aquilante, J. Autschbach, A. Baiardi, S. Battaglia, V. A. Borin, L. F. Chibotaru, I. Conti, L. D. Vico, M. Delcey, I. F. Galván, N. Ferré, L. Freitag, M. Garavelli, X. Gong, S. Knecht, E. D. Larsson, R. Lindh, M. Lundberg, P. Åke Malmqvist, A. Nenov, J. Norell, M. Odelius, M. Olivucci, T. B. Pedersen, L. Pedraza-González, Q. M. Phung,

K. Pierloot, M. Reiher, I. Schapiro, J. Segarra-Martí, F. Segatta, L. Seijo, S. Sen, D. C. Sergentu, C. J. Stein, L. Ungur, M. Vacher, A. Valentini, and V. Veryazov, "Modern quantum chemistry with [open]molcas," *The Journal of Chemical Physics*, vol. 152, p. 214117, 6 2020.

[144] I. Bengtsson and K. Życzkowski, *Geometry of Quantum States*. Cambridge University Press, 8 2017.

[145] L. Ratini, C. Capecci, and L. Guidoni, "Optimization strategies in wahtor algorithm for quantum computing empirical ansatz: a comparative study," 2023.

La borsa di dottorato è stata cofinanziata con risorse del Programma Operativo Nazionale 2014-2020 (CCI 2014IT16M2OP005), Fondo Sociale Europeo, Azione I.1 “Dottorati Innovativi con caratterizzazione industriale”